

ALMA MATER STUDIORUM • UNIVERSITÀ DI BOLOGNA

---

Scuola di Scienze  
Corso di Laurea Magistrale in Fisica del Sistema Terra

**PCA study of the interannual  
variability of the GPS height  
and environmental parameters**

**Relatore:**  
**Prof. Susanna Zerbini**

**Presentata da:**  
**Letizia Elia**

**Sessione III**  
**Anno Accademico 2018/2019**



*A Paolino  
e Mirella*



# Abstract

ENGLISH VERSION

Time series of GPS coordinates longer than two decades are now available at many stations around the world. The objective of this study is to investigate large networks of GPS stations to identify and analyze spatially coherent signals present in the coordinate time series and, at the same locations, to identify and analyze common patterns in the series of environmental parameters and climate indices.

The study is confined to Europe and the Mediterranean area, where 107 GPS stations were selected from the archive of the Nevada Geodetic Laboratory (NGL) on the basis of the completeness and length of the data series. The parameters of interest for this study are the stations GPS Up coordinate, the atmospheric surface pressure (SP), the terrestrial water storage (TWS) and various climate indices, namely NAO (North Atlantic Oscillation), EA (East Atlantic), AO (Arctic Oscillation), SCAND (Scandinavia Index), TNA (Tropical North Atlantic) and MEI v2 (Multivariate ENSO Index version 2).

The Principal Component Analysis (PCA) is the methodology adopted to extract the main patterns of the space/time variability of these parameters. The work also focused on the coupled modes of space/time interannual variability between pairs of variables using the Singular Value Decomposition (SVD) methodology. The coupled variability between all the aforementioned parameters is investigated. It shall be pointed out that PCA and SVD are mathematical tools providing common modes on the one hand, and statistical correlations between pairs of parameters on the other. Therefore, these methodologies do not allow to directly infer the physical mechanisms responsible for the observed behaviors which should be explained through appropriate modelling.

This study has identified, over Europe and the Mediterranean, main modes of variability in the time series of GPS Up coordinates, SP and TWS. For example, regarding the stations GPS Up coordinate, the first mode explains about 30% of the variance and the spatial pattern is coherent over the entire study area. The SVD analysis of coupled parameters, namely GPS Up-SP and GPS Up-TWS, showed that most of the common variability is explained by the first 3 modes. In particular, 70% for the GPS Up-SP and 49% for the GPS Up-TWS pair. Moreover, the correlation between the stations GPS Up coordinate and the climate indices was estimated to

investigate the possible influence of climate variability on the GPS Up coordinate behavior. To do so, the stations GPS Up coordinate were represented using the first four modes of variability to reduce the potential effect of local anomalies. More than 30 stations, over the total of 107, show significant correlations up to about 0.3 with the AO, TNA and SCAND indices. The correlation coefficients with MEI v2 and EA turn out to be significant and up to 0.5 for about half of the stations.

Attualmente sono disponibili serie temporali di coordinate GPS più lunghe di vent'anni per molte stazioni GPS intorno al mondo. L'obiettivo di questo studio è quello di identificare segnali spazialmente coerenti nelle serie temporali delle coordinate GPS di un network di stazioni e, negli stessi siti, di identificare e analizzare pattern comuni nelle serie di parametri ambientali e indici climatici.

Lo studio è confinato in Europa e nel Mediterraneo, dove 107 stazioni GPS sono state selezionate dagli archivi del Nevada Geodetic Laboratory (NGL) sulla base di completezza e lunghezza temporale delle serie di dati. I parametri di interesse per questo studio sono la coordinata Up del GPS, la pressione atmosferica alla superficie (SP), l'acqua accumulata sulla superficie terrestre (TWS) e vari indici climatici, ossia NAO (North Atlantic Oscillation), EA (East Atlantic), AO (Arctic Oscillation), SCAND (Scandinavia Index), TNA (Tropical North Atlantic) e MEI v2 (Multivariate ENSO Index version 2).

L'analisi delle componenti principali (PCA) è la metodologia che è stata adottata per estrarre i principali pattern di variabilità spaziale/temporale di questi parametri. Il lavoro è stato incentrato anche sull'analisi dei modi di variabilità comuni tra coppie delle variabili menzionate sopra, ottenuti tramite la decomposizione ai valori singolari (SVD). Bisogna puntualizzare che PCA e SVD sono strumenti matematici che forniscono rispettivamente modi comuni di variabilità all'interno dei dati e correlazioni statistiche tra coppie di variabili. Pertanto, questi metodi statistici non consentono di dedurre direttamente i meccanismi fisici responsabili dei comportamenti osservati, i quali dovrebbero essere spiegati attraverso modelli appropriati.

Questo studio ha identificato, in Europa e nel Mediterraneo, i principali modi di variabilità delle serie temporali di coordinata Up GPS, SP e TWS. Per esempio, riguardo alla coordinata Up delle stazioni GPS, il primo modo di variabilità spiega il 30% della varianza del sistema e il pattern spaziale è coerente su tutta l'area di studio. L'analisi SVD di coppie di parametri, ossia GPS Up-SP e GPS Up-TWS, ha mostrato che la maggior parte della variabilità comune è spiegata dai primi 3 modi. In particolare, il 70% per la coppia GPS Up-SP e 49% per la coppia GPS Up-TWS. Inoltre, è stata stimata la correlazione tra la coordinata Up delle stazioni GPS e gli indici climatici, in modo tale da investigare la possibile influenza del clima sul movimento verticale delle stazioni GPS. Per ridurre l'effetto delle anomalie locali, le serie temporali della coordinata Up delle stazioni sono state ricostruite tramite i primi quattro modi di variabilità. Più di 30 stazioni, su un totale di 107, hanno

mostrato correlazioni significative fino a 0.3 con gli indici AO, TNA, SCAND. La correlazione con il MEI v2 e l'EA sono risultate significative e fino a 0.5 per quasi la metà delle stazioni.

# Contents

<b>Abstract</b>	<b>v</b>
<b>List of Figures</b>	<b>xi</b>
<b>List of Tables</b>	<b>xvii</b>
<b>1 Background and motivation</b>	<b>1</b>
1.1 Global Positioning System (GPS) . . . . .	3
1.1.1 East, North and Up (ENU) coordinate system . . . . .	5
1.2 Principal Component Analysis (PCA) . . . . .	5
1.2.1 Mathematical definition . . . . .	7
1.2.2 Interpretation . . . . .	8
1.2.3 Singular Value Decomposition (SVD) . . . . .	10
<b>2 Data pre-processing</b>	<b>13</b>
2.1 GPS data . . . . .	14
2.1.1 Stations selection . . . . .	14
2.1.2 Outliers . . . . .	16
2.1.3 Offsets . . . . .	19
2.1.4 Interpolation using PCA . . . . .	22
2.1.5 Seasonal variability of the GPS Up time series . . . . .	26
2.2 Surface pressure and terrestrial water storage data . . . . .	29
2.2.1 Surface pressure (SP) . . . . .	29
2.2.2 Terrestrial water storage (TWS) . . . . .	30
<b>3 PCA analysis</b>	<b>33</b>
3.1 PCA results . . . . .	33
3.1.1 GPS Up . . . . .	34
3.1.2 Surface pressure (SP) . . . . .	47
3.1.3 Terrestrial water storage (TWS) . . . . .	54
3.2 SVD . . . . .	62

---

3.2.1	GPS Up coordinates and SP . . . . .	62
3.2.2	GPS Up coordinate and TWS . . . . .	67
<b>4</b>	<b>GPS Up and climate indices</b>	<b>71</b>
4.1	Northern Hemisphere Indices . . . . .	72
4.1.1	North Atlantic Oscillation (NAO) . . . . .	73
4.1.2	East Atlantic (EA) . . . . .	77
4.1.3	Scandinavia (SCAND) . . . . .	81
4.2	Arctic Oscillation (AO) . . . . .	85
4.3	Tropical North Atlantic (TNA) . . . . .	89
4.4	Multivariate ENSO Index Version 2 (MEI v2) . . . . .	92
	<b>Conclusions</b>	<b>99</b>
	<b>Bibliography</b>	<b>103</b>
	<b>Acknowledgements</b>	<b>115</b>
	<b>Appendices</b>	<b>117</b>
A	GPS Stations list . . . . .	119

# List of Figures

1.1	The Global Positioning System (GPS), 24 satellite configuration (Seeber, 2003).	3
1.2	Basic principles of positioning with GPS (Seeber, 2003).	3
1.3	The East, North and Up (ENU) and the $(x, y, z)$ ECEF coordinate systems.	6
2.1	Distribution of missing data in the weekly time series of the GPS stations up coordinate between 2008 and 2019 in log-scale. The number of occurrences is in log-scale.	16
2.2	Location of the GPS stations.	17
2.3	Up coordinate time series of the TRIE GPS station. The red dots are the identified outliers, while the green dots are up coordinates after the outliers removal.	18
2.4	SOPAC <sup>1</sup> offsets characterization since 1995 over 340 sites (560 offsets): type of offset (a); frequency of occurrence of offsets with a certain magnitude (b).	20
2.5	Up coordinate time series of the GPS station EUSK before ((a), red dots) and after ((b), blue dots) the offset correction. The green triangles identify the epochs of the discontinuities, corresponding to information given by the NGL.	21
2.6	Up coordinate time series of the GPS station GAIA before ((a), red dots) and after ((b), blue dots) the offset correction. The green triangles identify the epochs of the discontinuities, corresponding to information given by the NGL.	21
2.7	Example of interpolation of the Up position component of the GPS station CORL; red dots are interpolated data, blue dots are the original ones.	26

2.8	Steps of the deseasonalizing procedure applied to the time series of the GPS Up coordinate of station DEVA: (a) original series after having removed the outliers (black line), linear trend (red line); (b) the residual time series, where outliers and linear trend were removed; (c) the time series after removal of a 5th order polynomial (black line), mean annual cycle (red line); (d) weekly interpolated time series after removal of the linear trend and of the mean annual cycle. . . . .	28
2.9	NCEP SP data grid. . . . .	29
2.10	MERRA-2 TWS data grid. . . . .	31
3.1	First spatial pattern of the weekly GPS Up coordinate residuals. .	37
3.2	First time component of the weekly GPS Up coordinate residuals.	37
3.3	Second spatial pattern of the weekly GPS Up coordinate residuals.	38
3.4	Second time component of the weekly GPS Up coordinate residuals.	38
3.5	Third spatial pattern of the weekly GPS Up coordinate residuals.	39
3.6	Third time component of the weekly GPS Up coordinate residuals.	39
3.7	Fourth spatial pattern of the weekly GPS Up coordinate residuals.	40
3.8	Fourth time component of the weekly GPS Up coordinate residuals.	40
3.9	Regionalization map of the first four spatial patterns of the GPS Up coordinate residuals. . . . .	41
3.10	Regionalization map of the first three spatial patterns of the GPS Up coordinate residuals. . . . .	41
3.11	Location of the GPS stations related to the two decades time series.	42
3.12	First spatial pattern of the two decades weekly GPS Up coordinate residuals. . . . .	43
3.13	First time component of the two decades weekly GPS Up coordinate residuals. . . . .	43
3.14	Second spatial pattern of the two decades weekly GPS Up coordinate residuals. . . . .	44
3.15	Second time component of the two decades weekly GPS Up coordinate residuals.. . . .	44
3.16	Third spatial pattern of the two decades weekly GPS Up coordinate residuals. . . . .	45

---

3.17	Third time component of the two decades weekly GPS Up coordinate residuals. . . . .	45
3.18	Fourth spatial pattern of the two decades weekly GPS Up coordinate residuals. . . . .	46
3.19	Fourth time component of the two decades weekly GPS Up coordinate residuals. . . . .	46
3.20	First spatial pattern of the weekly SP residuals. . . . .	49
3.21	First time component of the weekly SP residuals. . . . .	49
3.22	Second spatial pattern of the weekly SP residuals. . . . .	50
3.23	Second time component of the weekly SP residuals. . . . .	50
3.24	Third spatial pattern of the weekly SP residuals. . . . .	51
3.25	Third time component of the weekly SP residuals. . . . .	51
3.26	Fourth spatial pattern of the weekly SP residuals. . . . .	52
3.27	Fourth time component of the weekly SP residuals. . . . .	52
3.28	Regionalization map of the first four spatial patterns of the SP residuals. . . . .	53
3.29	Regionalization map of the first three spatial patterns of the SP residuals. . . . .	53
3.30	First spatial pattern of the weekly TWS residuals. . . . .	56
3.31	First time component of the weekly TWS residuals. . . . .	56
3.32	November 2010 Precipitation Anomalies in millimeters (NOAA National Centers for Environmental Information, 2018f). . . . .	57
3.33	Second spatial pattern of the weekly TWS residuals. . . . .	58
3.34	Second time component of the weekly TWS residuals. . . . .	58
3.35	Third spatial pattern of the weekly TWS residuals. . . . .	59
3.36	Third time component of the weekly TWS residuals. . . . .	59
3.37	Fourth spatial pattern of the weekly TWS residuals. . . . .	60
3.38	Fourth time component of the weekly TWS residuals. . . . .	60
3.39	Regionalization map of the first four spatial patterns of the TWS residuals. . . . .	61
3.40	Regionalization map of the first three spatial patterns of the TWS residuals. . . . .	61
3.41	First SVD of GPS Up component and SP. . . . .	64

3.42	Second SVD of GPS Up component and SP. . . . .	65
3.43	Third SVD of GPS Up component and SP. . . . .	66
3.44	First SVD of GPS Up component and TWS. . . . .	68
3.45	Second SVD of GPS Up component and TWS. . . . .	69
3.46	Third SVD of GPS Up component and TWS. . . . .	70
4.1	Spatial pattern of the NAO from January 1950 to January 2000 (NOAA CPC, 2000). . . . .	73
4.2	The NAO standardized 3-month running mean index (NOAA CPC, 2020e). . . . .	74
4.3	Comparison between the GPS Up second time component and the NAO index. . . . .	74
4.4	Comparison between the GPS Up third time component and the NAO index. . . . .	75
4.5	Correlation map between GPS Up time series and the NAO index. Lilac points identify the GPS sites whose time series has a significant correlation larger than 10%. . . . .	76
4.6	The EA positive phase spatial pattern during January, April, July and October (NOAA CPC, 2020b). . . . .	77
4.7	The EA standardized 3-month running mean index (NOAA CPC, 2020c). . . . .	78
4.8	Comparison between the GPS Up first time component and the EA index. . . . .	78
4.9	Comparison between the GPS Up fourth time component and the EA index. . . . .	79
4.10	Correlation map of the GPS Up time series and the EA index. The GPS sites the Up time series of which show a correlation with the EA index larger than 10% and a significance level larger than 95% are identified by lilac points; those sites with correlation above the same threshold and a significance level larger than 99% are identified by white points. . . . .	80
4.11	The SCAND positive phase spatial pattern during January, April, July and October (NOAA CPC, 2020f). . . . .	82
4.12	The SCAND standardized 3-month running mean index (NOAA CPC, 2020g). . . . .	82

---

4.13	Comparison between the GPS Up second time component and the SCAND index. . . . .	83
4.14	Correlation map of the GPS Up time series and the SCAND index. The GPS sites the Up time series of which show a correlation with the SCAND index larger than 10% and a significance level larger than 95% are identified by lilac points; those sites with correlation above the same threshold and a significance level larger than 99% are identified by white points. . . . .	84
4.15	The AO spatial pattern (NOAA CPC, 2020a). . . . .	85
4.16	AO positive and negative phases (NOAA NCDC, 2010). . . . .	86
4.17	Graphic representation of the AO positive and negative phases (NOAA NCDC, 2010). . . . .	86
4.18	Comparison between the GPS Up third time component and the AO index. . . . .	87
4.19	Correlation map of the GPS Up time series and the AO index. The GPS sites the Up time series of which show a correlation with the AO index larger than 10% with a significance level larger than 95% are identified by lilac points; those sites with correlation above the same threshold and a significance level larger than 99% are identified by white points. . . . .	88
4.20	Area relevant to the TNA SST index. . . . .	89
4.21	Comparison between the GPS Up first time component and the TNA index. . . . .	90
4.22	Comparison between the GPS Up fourth time component and the TNA index. . . . .	90
4.23	Correlation map of the GPS Up time series and the TNA index. The GPS sites the Up time series of which show a correlation with the TNA index larger than 10% with a significance level larger than 95% are identified by lilac points; those sites with correlation above the same threshold and a significance level larger than 99% are identified by white points. . . . .	91
4.24	Schematic representation of El Niño (a) and La Niña (b) (Doyle, 2018). Red and blue mean higher and lower SST, respectively. . .	93
4.25	The MEI v2 time series; red represents the warm phase (El Niño) and blue the cold phase (La Niña). . . . .	94

---

4.26	Comparison between the GPS Up second time component and the MEI index. . . . .	95
4.27	Comparison between the GPS Up third time component and the MEI index. . . . .	95
4.28	Comparison between the GPS Up fourth time component and the MEI index. . . . .	96
4.29	Correlation map of the GPS Up time series and the MEI index. The GPS sites the Up time series of which show a correlation with the MEI index larger than 10% with a significance level larger than 95% are identified by lilac points; those sites with correlation above the same threshold and a significance level larger than 99% are identified by white points. . . . .	97
4.30	Annual European precipitation anomalies from 1979 to 2017, relative to the annual average for the period 1981-2010 (Copernicus Climate Change Service, 2017). . . . .	101

# List of Tables

3.1	Percentage of variance explained by each mode of variability of the GPS Up coordinate data set. . . . .	35
3.2	Percentage of variance explained by each mode of variability of the SP data set. . . . .	48
3.3	Percentage of variance explained by each mode of variability of the TWS data set. . . . .	55
4.1	Number of GPS sites for each of the following conditions: correlation coefficient ( $r$ ) in absolute value higher or equal to 10%; significance level lower or equal to 95%; correlation coefficient ( $r$ ) in absolute value higher or equal to 10% and significance level larger than 95%; correlation coefficient ( $r$ ) in absolute value higher or equal to 10% and significance level larger than 99%. . . . .	75
4.2	Number of GPS sites for each of the following conditions: correlation coefficient ( $r$ ) in absolute value higher or equal to 10%; significance level lower or equal to 95%; correlation coefficient ( $r$ ) in absolute value higher or equal to 10% and significance level larger than 95%; correlation coefficient ( $r$ ) in absolute value higher or equal to 10% and significance level larger than 99%. . . . .	79
4.3	Number of GPS sites for each of the following conditions: correlation coefficient ( $r$ ) in absolute value higher or equal to 10%; significance level lower or equal to 95%; correlation coefficient ( $r$ ) in absolute value higher or equal to 10% and significance level larger than 95%; correlation coefficient ( $r$ ) in absolute value higher or equal to 10% and significance level larger than 99%. . . . .	83
4.4	Number of GPS sites for each of the following conditions: correlation coefficient ( $r$ ) in absolute value higher or equal to 10%; significance level lower or equal to 95%; correlation coefficient ( $r$ ) in absolute value higher or equal to 10% and significance level larger than 95%; correlation coefficient ( $r$ ) in absolute value higher or equal to 10% and significance level larger than 99%. . . . .	87

4.5	Number of GPS sites for each of the following conditions: correlation coefficient ( $r$ ) in absolute value higher or equal to 10%; significance level lower or equal to 95%; correlation coefficient ( $r$ ) in absolute value higher or equal to 10% and significance level larger than 95%; correlation coefficient ( $r$ ) in absolute value higher or equal to 10% and significance level larger than 99%. . . . .	91
4.6	Number of GPS sites for each of the following conditions: correlation coefficient ( $r$ ) in absolute value higher or equal to 10%; significance level lower or equal to 95%; correlation coefficient ( $r$ ) in absolute value higher or equal to 10% and significance level larger than 95%; correlation coefficient ( $r$ ) in absolute value higher or equal to 10% and significance level larger than 99%. . . . .	96
A.1	GPS station name, latitude and longitude. . . . .	122

# Background and motivation

---

1.1	Global Positioning System (GPS) . . . . .	3
1.1.1	East, North and Up (ENU) coordinate system . . . . .	5
1.2	Principal Component Analysis (PCA) . . . . .	5
1.2.1	Mathematical definition . . . . .	7
1.2.2	Interpretation . . . . .	8
1.2.3	Singular Value Decomposition (SVD) . . . . .	10

---

The Earth's crust has always been subjected to surface deformations. The deformations might have several causes and could take place at variable time scales and with different magnitude. For example, there exist diurnal and semi-diurnal deformations, which are driven by the gravitational attraction exerted by the Sun, the Moon and the planets of the Solar system. These motions of the Earth surface are called solid Earth tides and the main component has meter-level amplitude. Other deformations are of tectonic nature, such as the displacements induced by earthquakes. Another well-known deformation is the Glacial Isostatic Adjustment (GIA) which is the process the Earth is undergoing to reach an equilibrium state in reaction to ice-age burden and the subsequent melting. The Earth deforms if stressed by loadings, such as the pressure exerted by the atmosphere, the liquid water and the snow.

Geoffrey Blewitt et al. (2001, 2002), showed that the most significant annual motions of the Earth's crust are driven by environmental mass redistribution, which generates changes in gravitational and surface forces that produce a stress response in the solid Earth, accompanied by characteristic patterns of surface deformation (Farrell, 1972; T.M. van Dam and Wahr, 1998). It has long been acknowledged that atmospheric pressure loading causes deformations of the surface of the Earth (Darwin, 1882) and it was observed that this loading can induce vertical displacements of up to 18 mm in mid-to high-latitudes (Gegout et al., 2009; Petrov and Boy, 2004; Tregoning and T. van Dam, 2005). Furthermore, the terrestrial water storage loading, which can be defined as the loading induced by the summation of all water on the land surface and subsurface including the

water stored in the vegetation (Giroto and Rodell, 2019), can cause vertical displacements up to 15 mm at the same latitudes (T. van Dam, Wahr, et al., 2001). Also the oceans play a key role when dealing with crustal deformations. On the one hand, the oceans exert the so called ocean loading. This effect is due to the elastic response of the Earth's crust to ocean tides, which produces a deformation of the sea floor and a surface displacement up to several cm of the adjacent lands (Subirana, Zornoza, and Hernández-Pajares, 2011). On the other, the oceans exert the so called non-tidal ocean loading, which concerns both the "normal" ocean circulation (e.g., Zerbini, Matonti, et al., 2004, T. van Dam, Collilieux, et al., 2012) and special occasions like storm surges (e.g., Fratepietro et al., 2006), which can cause a vertical displacement of a few centimeters within hours (Geng et al., 2012).

The changes in the climate system can be observed by monitoring environmental parameters, such as the atmospheric pressure and the terrestrial water content. Variations in such parameters modify crustal loadings. As a consequence, the crustal deformation patterns are expected to be related to the climate change and to climate indices, which are a tool by which monitoring climate variability. The Earth's climate has changed throughout history, but the current changes are of particular significance because most of them are likely to be the result of human activity since the mid-20th century and are proceeding at a rate that is unprecedented over decades to millennia (NASA JPL Earth Science Communications Team, 2019; Working Group I to the Fifth Assessment Report of the IPCC, 2013). Earth-orbiting satellites and other technological advances have enabled scientists to see the big picture, collecting many different types of information about our planet and its climate on a global scale. These data, collected over many years, reveals the signals of a changing climate, which can be linked to crustal deformations thanks to satellite positioning techniques.

The purpose of this work is to study, by means of an appropriate statistical analysis, the principal modes of variability of non-linear and non-tidal vertical displacements of the crust and some of the environmental parameters mentioned previously, namely the atmospheric surface pressure and the terrestrial water storage, which could be responsible for the observed surface deformations. Also the coupled modes of variability between the vertical displacements and the environmental parameters will be investigated. Finally, the study also investigates the correlation between vertical displacements and a few climate indices.

In the following Sections, the technique through which vertical displacements are measured and the statistical theory that is behind the analysis carried out in this work are discussed.

## 1.1 Global Positioning System (GPS)

The detection of crustal displacements with mm accuracy are nowadays possible thanks to the availability of space geodetic techniques and, in particular, of the Global Navigation Satellite System (GNSS). GNSS is the ensemble of different positioning systems, among which the GPS (Global Positioning System) constellation. GNSS allows accurate and frequent positioning of dense networks of stations globally distributed. For this reason, the present work uses data provided by this space geodetic technique for monitoring vertical displacements.

The first realization of the GNSS was the GPS, which is defined, according to Wooden (1985), as:

“The NAVSTAR Global Positioning System is an all-weather, space-based navigation system developed by the U. S. Department of Defense (DoD) to satisfy the requirements for the military forces to accurately determine their position, velocity, and time in a common reference system, anywhere on, or near, the Earth on a continuous basis.”

The GPS is a satellite-based radio navigation system providing precise three dimensional position, navigation and time information to suitably equipped users (Seeber, 2003). The final configuration of the GPS consists of nominally 24 satellites placed in orbits at about 20200 km above the surface of the Earth (Figure 1.1). The navigation principle is based on the measurement of the so-called pseudoranges between the user and, at least, four satellites (Figure 1.2).

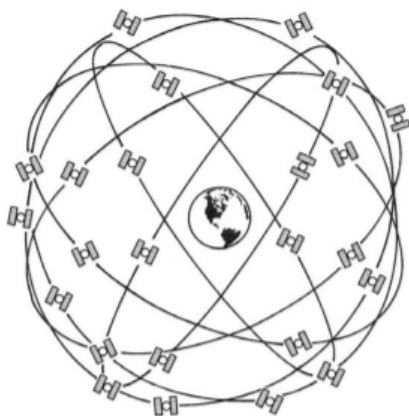


Figure 1.1: The Global Positioning System (GPS), 24 satellite configuration (Seeber, 2003).

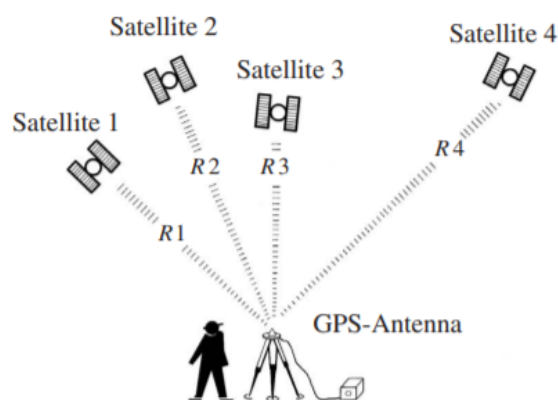


Figure 1.2: Basic principles of positioning with GPS (Seeber, 2003).

The coordinates of the user antenna can be obtained by knowing the satellite coordinates (i.e. the ephemeris) in a suitable reference frame. From the geometrical point of view three ranges, i.e. three observable satellites, would be sufficient,

but since the GPS uses the one-way ranging technique<sup>1</sup> a fourth observation is necessary in order to correct the synchronization error. This synchronization error is the reason for the term "pseudorange".

Data collected by the GPS receiver are available in the form of RINEX files which contain the code and phase pseudoranges. A code pseudorange is a measure of the travel time, converted into distance, of a GPS signal, from a satellite to a station, using the C/A code or the P code<sup>2</sup>. A phase pseudorange is a measure, converted into distance, of the phase difference of the GPS signal between the emission at the satellite and the reception at the station. Code and phase pseudoranges are affected by several error sources, including the errors of the satellite and stations clocks. Moreover, phase pseudoranges are ambiguous by an integer number of cycles (i.e., the phase cycle ambiguity). Despite this, the phase pseudoranges are much precise than code pseudoranges (a few millimeters compared to roughly 1 meter precision).

The GPS signal, which is an electromagnetic wave in the microwave spectrum, travels through multiple atmospheric layers after leaving the satellite and until reaching the receiver antenna. The signal interacts both with the dry and wet troposphere<sup>3</sup> and the ionosphere<sup>4</sup>. This interaction implies that the signal propagation is delayed, therefore corrections should be applied when evaluating the phase pseudoranges. The correction for the dry troposphere can be achieved by means of a rather simple model, while the wet component is more difficult to be accounted for because it is highly variable in space and time. However, a description of these error modeling is beyond the scope of this work. GPS signals interact with the ionosphere; in fact, the induced ionospheric effects on the code (delay) and phase (advance) pseudoranges have been used to study the ionosphere and related phenomena (Thomas, 2018). However, the advance of the GPS signal phases due to ionospheric refraction is frequency-dependent, therefore if phase pseudoranges are measured by a dual frequency receiver, it is possible to cancel (at least to the first order) the ionosphere-induced error.

These corrections and the preprocessing of the GPS signals are made by using

---

<sup>1</sup>In the one-way mode it is assumed that either the clocks in the satellite and in the receiver are synchronized with each other or that a remaining synchronization error can be determined through the observation technique (Seeber, 2003).

<sup>2</sup>The C/A (coarse acquisition) code and the P code (precise code) are the modulation codes, which are a series of  $-1/ + 1$ . These codes modulates the signal generated by the satellite at a fixed frequency given by the atomic clock given by the satellite itself.

<sup>3</sup>The troposphere is the lowest layer of the atmosphere of Earth. The total average height of the troposphere is 13 km. The wet troposphere is the water vapour component of the total air mass of the troposphere. The dry troposphere is constituted by the remaining components of the troposphere which are not water vapour (oxygen, nitrogen, argon, carbon dioxide and others)

<sup>4</sup>The ionosphere is the ionized part of the upper atmosphere of Earth, from about 60 km to 1,000 km altitude.

sophisticated software packages, allowing the high-accuracy evaluation of the receiver coordinates. Among the most well-known software for the GPS and, in general, GNSS data processing are the Bernese (developed at the Astronomical Institute of the University of Berne) and GIPSY-OASIS II (developed by the NASA Jet Propulsion Laboratory in Pasadena, California).

### 1.1.1 East, North and Up (ENU) coordinate system

The coordinates provided by the software are the  $(x, y, z)$  Earth-Centered Earth-Fixed (ECEF) and the East, North and Up (ENU). Both are defined with respect to the ellipsoid which best approximates the Earth surface. Since the Earth undergoes deformations, this ellipsoid is updated periodically together with the geodetic datum<sup>5</sup>. Nowadays the global geodetic datum are the IGS14 and the ITRF14<sup>6</sup>.

ECEF is a Cartesian coordinate system in which the point of coordinates (0,0,0) is center of mass of the Earth. The  $z$  axis direction is towards the true North, the  $x$  axis is perpendicular to the  $z$  axis and intersects the prime meridian in Greenwich and the  $y$  axis completes the triad of coordinates (Figure 1.3). The ECEF rotates with the Earth, such that coordinates of a fixed point on the surface of the Earth do not change.

ENU are local coordinates and are formed considering a plane tangent to Earth surface, fixed at a specific location, in which the North direction follows the local meridian, the East direction follows the circle of latitude and the Up is outward with respect to the Earth surface and perpendicular to east and north axis (Figure 1.3).

In this work, the coordinate used for studying the vertical displacements of the locations of interest is the Up coordinate, obtained by means of GPS measurements at the selected network of stations.

## 1.2 Principal Component Analysis (PCA)

The Principal Component Analysis (PCA) is a statistical method used for the analysis of the spatial and temporal variability of a dataset. The origin of the PCA method can be traced back to E. Beltrami (1835-1899), C. Jordan (1838-1921), J.

---

<sup>5</sup>A geodetic datum is a coordinate system and a set of reference points used for locating places on the Earth.

<sup>6</sup>The IGS14 is a GNSS reference frame, while the ITRF14 is built with a combination of GNSS and other geodetic techniques.

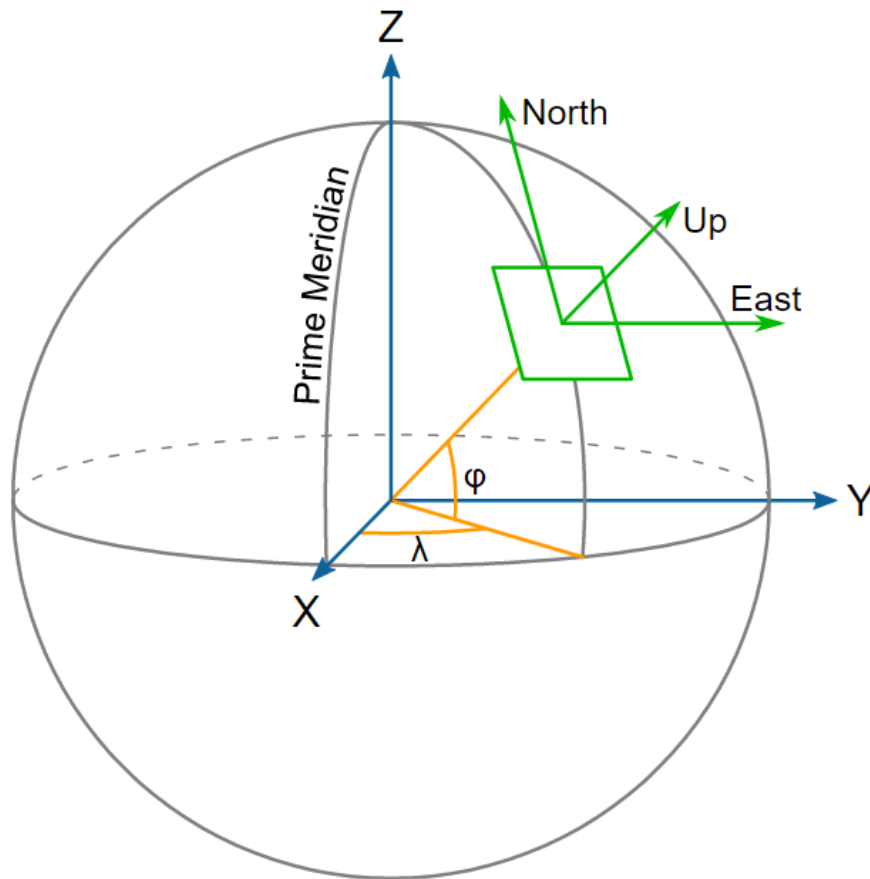


Figure 1.3: The East, North and Up (ENU) and the  $(x, y, z)$  ECEF coordinate systems.

J. Sylvester (1814-1897), E. Schmidt (1876-1959) and H. Weyl (1885-1955), who, independently from each others, laid the foundation of this statistical method (Stewart, 1993). The official introduction of the PCA in literature is commonly attributed to K. Pearson in 1901 (Pearson, 1901), but its modern formalization is due to H. Hotelling, who proposed the term "principal component" in 1933 (Abdi and Williams, 2010).

Subsequently, the PCA became a widespread method in many fields requiring data analysis, in particular, in geophysical sciences. For example, nowadays the PCA are used for climatological research purposes in order to try to link environmental parameters to historical time series related to specific locations (e.g., Eccel et al., 2012) or to study the effects of climate changes (e.g., Sagredo and Lowell, 2012). The PCA is also applied to space geodetic observations in order to monitor co-seismic and post-seismic deformations (e.g., Savage and Svarc, 2010) or tectonic deformations (e.g., Pan et al., 2018). The PCA can also be used to identify the principal spatial pattern of variability of a dataset and their time variations and to reduce the dimensionality of the data, representing the dataset through the principal modes of variability (Zerbini, Raicich, et al., 2013).

### 1.2.1 Mathematical definition

In order to define the PCA, the dataset has to be organized in a matrix. It is assumed that the dataset consists of measurements of the same variable taken at:

- the locations  $x_1, \dots, x_p$ ;
- the epochs  $t_1, \dots, t_n$ .

At each epoch  $t_i$ , the measurements taken at different positions represents a map or a field. The measures are organized in a matrix  $F_{ij}$ , where  $i$  is the time-index and  $j$  is the space-index. Therefore the column  $j$  is the time series of the location  $x_j$ , while the row  $i$  represents a map at the epoch  $t_i$ :

$$F_{ij} = \begin{bmatrix} f_{11} & f_{1,2} & \dots & f_{1p} \\ f_{21} & f_{22} & \dots & f_{2p} \\ f_{31} & \ddots & & \vdots \\ \vdots & & \ddots & \vdots \\ f_{n1} & f_{n2} & \dots & f_{np} \end{bmatrix} = \begin{bmatrix} f(t_1, x_1) & f(t_1, x_2) & \dots & f(t_1, x_p) \\ f(t_2, x_1) & f(t_2, x_2) & \dots & f(t_2, x_p) \\ f(t_3, x_1) & \ddots & & \vdots \\ \vdots & & \ddots & \vdots \\ f(t_n, x_1) & f(t_n, x_2) & \dots & f(t_n, x_p) \end{bmatrix} \quad . \quad (1.1)$$

Each of the  $p$  columns is then standardized in order to have columns with unit variance and avoid that time series with greater variability dominate over the others at the end of the analysis.

Since each column is a standardized time series, the matrix  $R = \frac{1}{n-1} F^T F$  is the correlation matrix and the relative eigenvalue problem is:

$$RC = C\Lambda \quad , \quad (1.2)$$

where

$$\Lambda = \begin{bmatrix} \lambda_1 & & \\ & \ddots & \\ & & \lambda_p \end{bmatrix}$$

is the diagonal matrix whose values are the eigenvalues of the correlation matrix  $R$  and the columns  $\vec{c}_i$  of the matrix

$$C = \begin{bmatrix} \vec{c}_1 & \dots & \vec{c}_p \end{bmatrix}$$

are the eigenvectors of  $R$  related to the eigenvalues  $\lambda_i$ .  $C$  e  $\Lambda$  are  $p \times p$  matrices.

Since  $R$  is a symmetric matrix, according to the Spectral theorem, there exist an orthogonal matrix  $C$  and a diagonal one  $\Lambda$  such that

$$\Lambda = C^T R C \quad .$$

These are the same matrix of the equation (1.2) and as a consequence the matrix  $C$  ( $C^{-1} = C^T$ ) and the vectors  $\vec{c}_i$  are orthogonal. The vectors  $c_i$  are called spatial patterns and their orthogonality implies that they are uncorrelated in space.

The vectors  $c_i$  (i.e., the spatial patterns) are ordered for decreasing eigenvalue  $\lambda_i^7$ , i.e. based on how much variance they explain, because the eigenvalues  $\lambda_i$  are the squared variance explained by the mode of variability. Plotting the spatial patterns, stationary oscillations are obtained and their time evolution is given by:

$$\vec{a}_i = F\vec{c}_i \quad , \quad (1.3)$$

where the vectors  $\vec{a}_i$  are the time components. The time components might be interpreted as the projections of the maps in  $F$  (i.e., the rows of the matrix  $F$ ) over the spatial patterns (Bjornsson and Venegàs, 1997).

Furthermore, from (1.3) derives

$$A = FC \iff AC^T = F \iff F = \sum_{i=1}^p \vec{a}_i \vec{c}_i^T \quad . \quad (1.4)$$

At this point, spatial patterns are commonly used to obtain a cleaner version of the data set, truncating the summation to an  $i = p' \ll p$ , i.e. it is assumed that the first  $p'$  eigenvalues capture the dynamic behaviour of the system and the remaining eigenvalues are random noise. This procedure is called dimensionality-reduction.

## 1.2.2 Interpretation

Recovering the matrix representation (1.1)

$$F_{ij} = \begin{bmatrix} f_{11} & f_{1,2} & \dots & f_{1p} \\ f_{21} & f_{22} & \dots & f_{2p} \\ f_{31} & \ddots & & \vdots \\ \vdots & & \ddots & \vdots \\ f_{n1} & f_{n2} & \dots & f_{np} \end{bmatrix} = \begin{bmatrix} \vec{f}_1^T \\ \vdots \\ \vec{f}_n^T \end{bmatrix} \quad ,$$

in which every row of  $F$  can be seen as a map over a fixed epoch or as a vector in a  $p$ -dimensional space. Therefore, the points of this space are the observations and, if these observations were completely random they would be distributed as an homogeneous cloud of points. On the contrary, if the observations were not random (i.e. if there are regularities in the data), a cluster would appear along a particular direction.

---

<sup>7</sup>The first spatial pattern will be the one with higher eigenvalue, etc.

The method consists in searching for the orthonormal base vectors  $e_m$  ( $m = 1, \dots, p$ ) in this  $p$ -dimensional space, which maximize the projection of the vectors  $\vec{f}_i$  along these base vectors ( $e_m$  are  $p$  vectors of dimension  $p$ , while  $f_i$  are  $n$  of dimension  $p$ ) and coincide with the eigenvectors of the correlation matrix  $R$ . Mathematically the problem is to maximize

$$\sum_{i=1}^n (e_m^T f_i)^2 = e_m^T F^T F e_m = e_m^T R e_m$$

with  $m = 1, \dots, p$  under the constraint

$$e_i^T e_j = \delta_{ij} \quad .$$

The standard approach is to use the Lagrange multiplier method, that consist in solving the equation

$$\nabla(\vec{x}^T R \vec{x}) - \lambda \nabla(\vec{x}^T \vec{x}) = 0 \quad (1.5)$$

for each vector  $\vec{x} = \vec{e}_m$ , where  $\nabla$  is the gradient operator and  $\lambda$  is the Lagrange multiplier. Manipulating the Equation (1.5)

$$\nabla(\vec{x}^T R \vec{x}) = \partial_i (x_j R_{jm} x_m) = R_{im} x_m + R_{ji} x_j = x_m (R_{im} + R_{im}^T) = 2R_{im} x_m = 2R \vec{x} \quad ,$$

$$\lambda \nabla(\vec{x}^T \vec{x}) = \lambda \partial_i (x_j x_j) = 2\lambda \vec{x} \quad ,$$

gives the equation

$$2R_{im} x_m = 2R \vec{x} = 2\lambda \vec{x} \quad , \quad (1.6)$$

which is the eigenvalues equation analogous of (1.2). Therefore, the spatial patterns emerge when searching a new  $\vec{x}$  coordinate system along the data regularities.

Since the matrix  $R$  is symmetric, according to the Spectral representation theorem, it can be decomposed into:

$$R = \lambda_1 c_1 c_1^T + \lambda_2 c_2 c_2^T + \dots + \lambda_p c_p c_p^T \quad .$$

This means that the greater is  $\lambda_i$ , the better the related spatial pattern  $c_i$  represents  $R$ , i.e. the system variability. Thus the series can be truncated at a  $p' < p$  retaining only those eigenvalue that represent, for example, 90% of variability:

$$\frac{\sum_{i=1}^{p'} \lambda_i}{\text{Tr } \Lambda} \leq 90\% \quad .$$

From this decomposition it can be inferred the amount of variance explained by the  $i$ -th mode, which is equal to  $\frac{\lambda_i}{\text{Tr } \Lambda}$ . Usually the first few eigenvalues (in order

of magnitude) dominates over the others, and this means that the largest part of data behaviour can be explained in terms of few base vectors, so that it is possible to reduce data to few variability modes. Thus data can be viewed as a subspace of the  $p$ -dimensional space. For example, if just the first  $p'$  eigenvalues are large, the space which generated the data is  $p'$ -dimensional. In this case  $p'$  eigenvalues explain almost the whole variance of the system, and the original series in Equation (1.4) can be recalculated truncating the summation:

$$F \simeq \sum_{i=1}^{p'} \vec{a}_i \vec{c}_i^t \quad . \quad (1.7)$$

### 1.2.3 Singular Value Decomposition (SVD)

The Singular Value Decomposition (SVD) method can be thought of as a generalization to rectangular matrices of the diagonalization of square symmetric matrices, like a PCA analysis (Bjornsson and Venegàs, 1997), and is usually applied in geophysics to study two data fields (for example, surface pressure and a GPS coordinate). It allows extracting orthogonal components that are common to both variables and therefore representing modes of coupled variability.

The SVD is widely used in many different geophysical fields, such as: climatology, where the SVD analysis is used, for example, to study the climate variability (e.g., Venegàs, Mysak, and Straub, 1996); meteorology, in which the SVD method has been used to characterize local phenomena (Bigot and Planchon, 2003), or to perform the downscaling<sup>8</sup> (e.g., Bertacchi Uvo et al., 2001); seismology, in which the SVD approach has been used, for example, to attenuate the random noise in seismic data (Gan et al., 2015); topography, where the SVD analysis is used in order to compare geographical maps (e.g., Dvorský, Snášel, and Voženílek, 2009); geodesy, in which the SVD analysis has been used in order to find common modes of variability between geodetic and environmental parameters (Zerbini, Raicich, et al., 2013).

In order to apply the SVD analysis to two fields, two data matrices are considered, namely  $S$  and  $P$ . Each of them is organized as in (1.1) and is related to a different variable (e.g., surface pressure and a GPS coordinate).

These matrices are allowed to have different dimensions, since each of the two variables might be measured in different locations: for example, given  $n$  the number of epochs,  $S$  might be  $n \times p$  and  $P$  might be  $n \times q$ , where  $p$  and  $q$  are number of locations. In this work each variable is measured at the same locations: this

---

<sup>8</sup>Downscaling is any procedure to infer high-resolution information from low-resolution variables.

implies that  $p$  and  $q$  are equal. As specified in Section 1.2.1, each column of  $S$  and  $P$  is a standardized time series for a fixed location and each row contains a map for a fixed time.

Once defined the cross-correlation matrix as  $R_{cross} = S^T P$ , the SVD of  $R_{cross}$  consists in finding the orthogonal matrices  $U$  and  $V$  and a diagonal matrix  $L$  so that

$$R_{cross} = U L V^T \quad . \quad (1.8)$$

The singular vectors for the matrix  $S$  are the columns  $\vec{u}_i$  of  $U$ , and the singular vectors for  $P$  are the columns  $\vec{v}_i$  of  $V$ . Each pair of singular vectors is a mode of co-variability between the fields  $S$  and  $P$  and represents a spatial pattern. The time series describing the oscillation in time of each mode, i.e. the time components of the mode of co-variability, are contained in the matrices

$$A = S U \quad , \quad B = P V \quad , \quad (1.9)$$

where the columns are the time components of each mode. The orthogonality of  $U$  and  $V$  leads to  $S = A U^T$  and  $P = B V^T$ . A measure of the importance of the  $i$ -th mode of variability is given by the fraction of squared cross-correlation (SCF) explained by this mode:

$$SCF_i = \frac{l_i}{\text{Tr}(L)} \quad , \quad (1.10)$$

in which  $l_i = L(i, i)$  are called singular values and  $\text{Tr}(L)$  is the trace of the matrix  $L$ . Generally only the modes of co-variability that jointly explain at least a SCF equal to 50% are taken into account.

Algorithms based on SVD have shown to be numerically more stable with respect to those based on PCA (Nakatsukasa and Higham, 2013; Wu, Massart, and Jong, 1997). This is the reason for which, in this work, the algorithms based on SVD are used also to perform PCA analysis, considering that:

- $R_{cross} = R$ ;
- $\lambda_i = \frac{l_i^2}{n-1}$ ;
- the eigenvectors of  $R$  are the column vectors of  $V$ .

In order to check the validity of this procedure, the last condition in the Equation (1.4) was verified.



# Data pre-processing

---

2.1	GPS data . . . . .	14
2.1.1	Stations selection . . . . .	14
2.1.2	Outliers . . . . .	16
2.1.3	Offsets . . . . .	19
2.1.4	Interpolation using PCA . . . . .	22
2.1.4.1	Mean and covariance estimators with missing data	23
2.1.4.2	Solution to the interpolation problem . . . . .	24
2.1.4.3	Implementation and results . . . . .	25
2.1.5	Seasonal variability of the GPS Up time series . . . . .	26
2.2	Surface pressure and terrestrial water storage data . . . . .	29
2.2.1	Surface pressure (SP) . . . . .	29
2.2.2	Terrestrial water storage (TWS) . . . . .	30

---

In this study, three types of parameters were studied: the Up component of GPS stations coordinates located in the European and Mediterranean area, the surface pressure (SP) and terrestrial water storage (TWS) at the same sites. For each of these variables, weekly time-series were used and the locations were chosen according to criteria described in Section 2.1.1.

Europe and the Mediterranean is the area of interest for this study. In total, the number of selected locations is 107, on the basis of the availability of the GPS data in the Nevada Geodetic Laboratory archive.

In this chapter the data sets preparation will be described by illustrating the procedure and the various steps carried out. On the one hand, the GPS data were subjected to a detailed process, starting from the standard data pre-processing (outliers removal and offsets correction) to the interpolation of the signals based on the Principal Component Analysis. On the other, SP and TWS data were only spatially interpolated, detrended and deseasonalized, in order to build time series at the locations of interest.

## 2.1 GPS data

For the study, it was used a subset of the GPS data sets made available online (Blewitt, Hammond, and Kreemer, 2018; <http://geodesy.unr.edu/>) by Nevada Geodetic Laboratory (NGL). NGL is a center of research which among other activities routinely provides time series of coordinates of more than 17,000 GNSS (Global Navigation Satellite System, including GPS) stations located all over the world.

The GPS data provided by NGL are analyzed through the GISPY-OASIS II (GOA II) software package (Section 1.1) and analysis products are provided to the NGL itself by the Jet Propulsion Laboratory, Pasadena, California. The NGL uses GOA II for the calculation of the ENU coordinates (Section 1.1.1) and the data analysis strategy adopted include the correction of ionosphere, wet and dry troposphere, solid tides, ocean tide loading and phase cycle ambiguities (Section 1.1). The NGL provides the ENU coordinates in meters, splitting the integer and the decimal part. The integer part does not change in time, while the decimal part varies in time. In this work the time series of the decimal part of the Up coordinate are those taken into account.

In the following, the steps of GPS data preparation carried out are described. They are respectively:

- choice of the GPS stations (Section 2.1.1);
- outlier removal and residuals estimation (Section 2.1.2);
- offsets detection (Section 2.1.3);
- data interpolation (Section 2.1.4);
- seasonal annual signal detection (Section 2.1.5).

### 2.1.1 Stations selection

In the NGL database, thousands of temporary or continuous GPS stations are available in the European/Mediterranean area. From this ensemble, a subset of about 100 stations was extracted. Filtering operation was performed according to the following criteria:

- the station location shall provide a homogeneous coverage of the area;
- the time span of the data set shall cover the period 2011-2018, in order to give the continuity to the work presented in Zerbini, Raicich, et al., 2013;

- the data quality.

First of all, stations in the European/Mediterranean area were selected. A rectangle was identified with the following latitude  $\phi$  and longitude  $\lambda$  ranges:

- $35^\circ \leq \phi \leq 71.3^\circ$ ;
- $-9.6^\circ \leq \lambda \leq 45^\circ$ .

Stations characterized by continuous data acquisition between 2011 and 2018 were selected. In a subsequent step, the stations the time series of which turned out to be below the following threshold were eliminated:

$$C_{th} = \left( \frac{N}{\tau} \right)_{th} ,$$

where  $N$  is the number of daily data and  $\tau$  is the time range of activity in days. The ratio  $C = \frac{N}{\tau}$  can be labelled "completeness" and can be interpreted as an index of the quality of the data set. The *completeness* threshold value was at first set to be  $C_{th} = 92\%$ . Each of the selected station started to acquire data at a different epoch, therefore the subsequent step was to cut the time series over the period of maximum time overlap.

However, the *completeness*, as defined above, is a value related to the whole time series, and not to the period that will be considered for the data analysis. This should not be a problem, since the probability that high completeness stations have a large amount of missing data exactly in the period under consideration is low.

In order to have a spatially uniform distribution of stations, it was decided to include about 20 additional stations, even if they did not comply with the completeness requisite. These additional stations are characterized by a *completeness* between 86% and 92%, excluded the station SRJV, whose *completeness* is about 55%.

In the Up coordinate time series, in addition to the *completeness* (i.e. missing data occurrences), it is even more relevant the problem generated by the number of contiguous missing weeks of data. A simple statistics concerning this property is presented in Figure 2.1. The histogram shows the frequencies at which the number of missing weeks occurs. As expected, it can be seen that the distribution peaks towards the lower values and goes to zero for a time period longer than 40 weeks.

Considering the adopted criteria, the total number of stations to be analyzed is 107 (Appendix A), the time series of which cover the period from June, 9, 2010 to September, 5, 2018 (i.e. the time span of maximum overlap). There are two regions

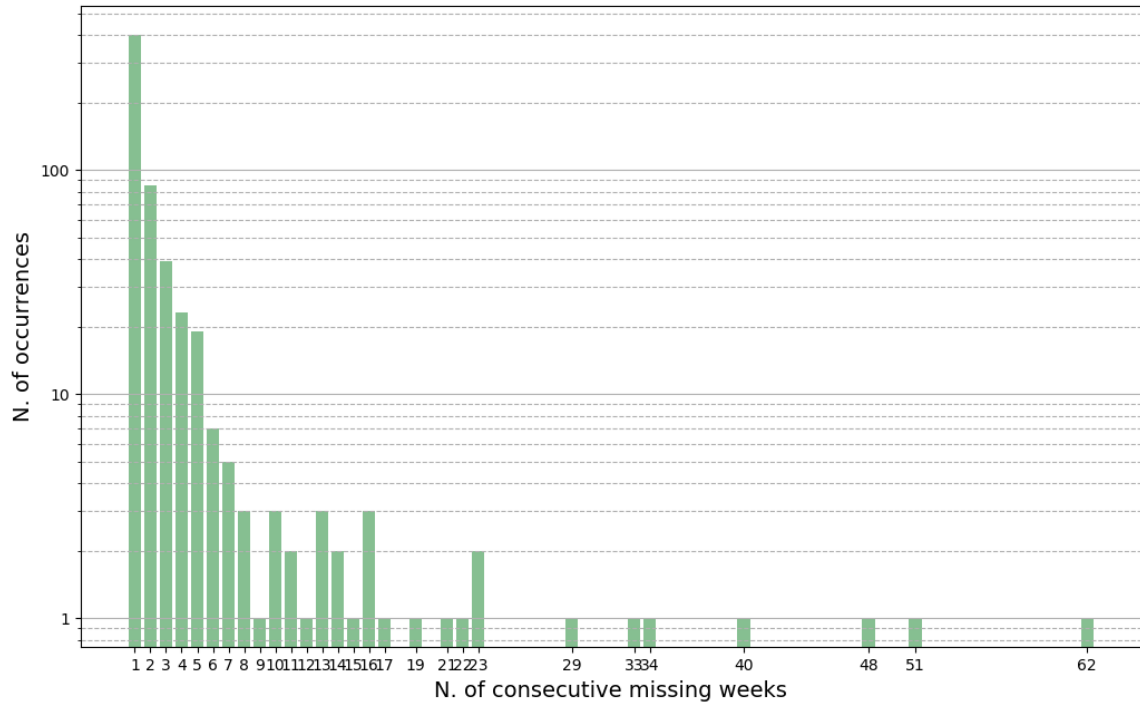


Figure 2.1: Distribution of missing data in the weekly time series of the GPS stations up coordinate between 2008 and 2019 in log-scale. The number of occurrences is in log-scale.

(Figure 2.2), namely the Balkans and Eastern Europe, that are characterized by a smaller density of stations. The reason is due to critical problems shown by the stations, such as long time data gaps.

### 2.1.2 Outliers

Every time measurements are performed and a data distribution is obtained, it may happen, for some reason, that a few or several values can differ significantly from the series of observations. These observations are usually labelled as outliers:

An outlier is an observation that deviates so much from other observations as to arouse suspicions that it was generated by a different mechanism (Hawkins, 1980).

This is not a precise definition, because it does not say how mathematically or physically a sample of measurements shall fit together, but such a definition does not exist.

In geodesy the term outlier is defined on the basis of a statistical hypothesis test necessary for identifying gross measurements errors in the observations (Baarda, 1968; Pope, 1976). Observations that are rejected by such a test are called outliers.

Outliers in the time series of GPS coordinates are generally related to variations

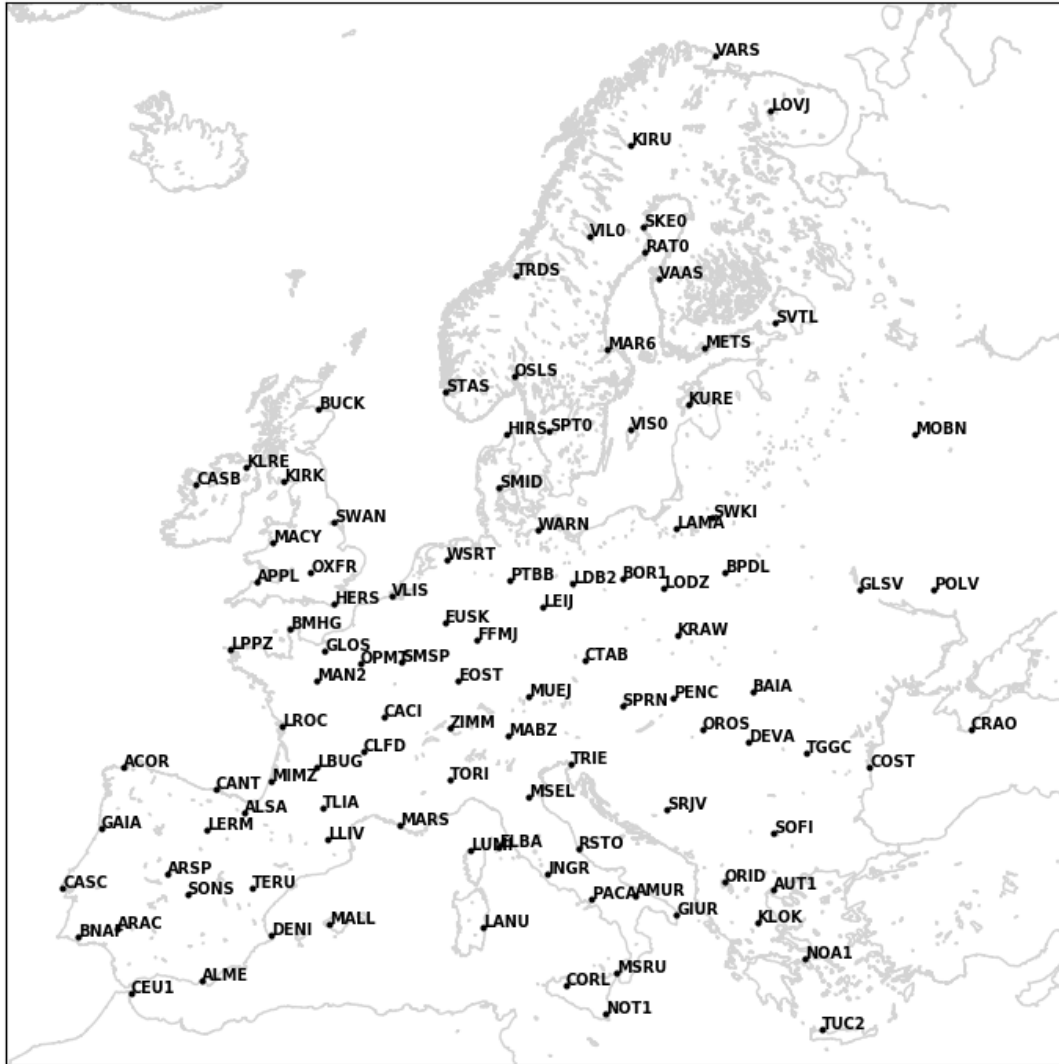


Figure 2.2: Location of the GPS stations.

in positioning accuracy, which might depend upon a number of factors, among them according to Ordóñez et al. (2011):

- failure of the receiver;
- errors in the satellite clock and ephemeris;
- errors in the receiver clock;
- badly estimated atmospheric delays;
- satellite geometry (distribution of satellites in azimuth and elevation).

The procedure adopted in this work to remove the outliers is based on a  $3\text{-}\sigma$  rejection criterion, which identifies as outliers those observations that deviate from

the mean by an amount equal or greater than three times the standard deviation. It is a simple method widely adopted in many fields (Lehmann, 2013)<sup>1</sup>.

In this work it was decided to cut each time series of the stations Up coordinate into a 3-months window, and apply first a  $2\text{-}\sigma$  and then a  $3\text{-}\sigma$  rejection criteria. The reason for this choice is that, to apply the  $\sigma$  rule, it is necessary to deal with a quasi-linear behaviour. In fact, when screening the GPS Up coordinate time series, in general one recognizes the occurrence of seasonal (yearly) oscillations; therefore, a 3-months window appears to be an appropriate choice for meeting the linear behaviour requirement. Moreover, the fact that an initial  $2\text{-}\sigma$  rejection is applied to the series is due to the relatively high level of noise that characterize the GPS data.

The outliers removal procedure is time consuming because each station has its own peculiarities. For this reason, each Up coordinate time series was checked after cleaning, in order to monitor the amount of data removed. An example of time series before and after applying the outliers removal is reported in Figure 2.3, in which the red dots are the identified outliers and the green dots are the cleaned data series.

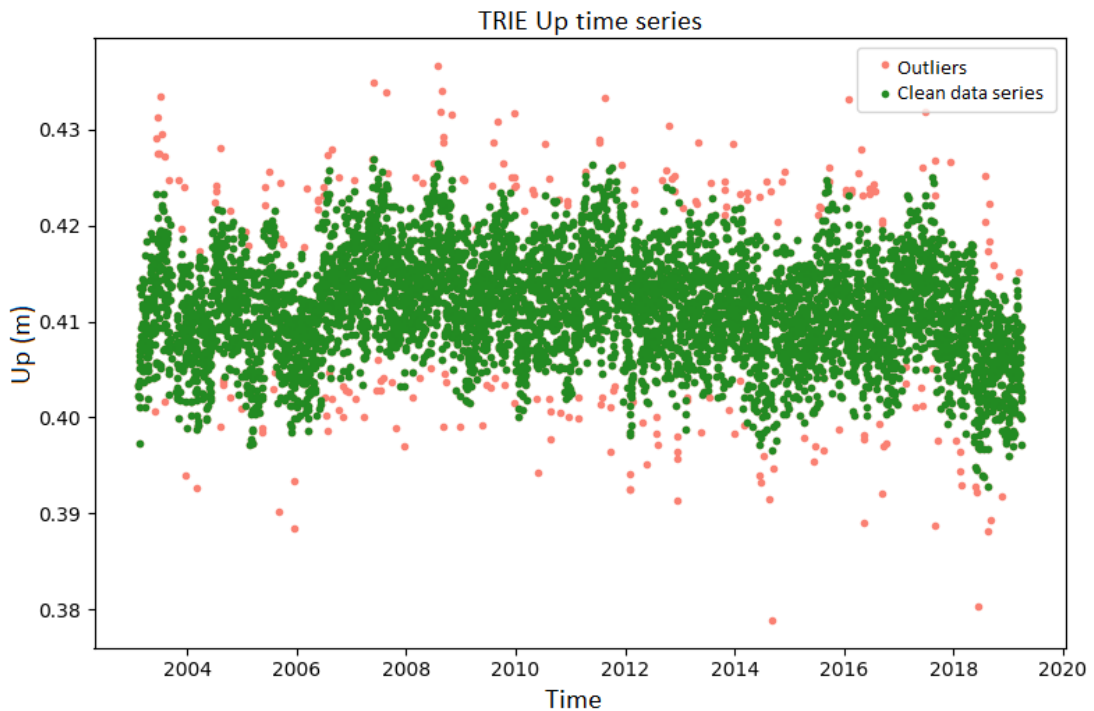


Figure 2.3: Up coordinate time series of the TRIE GPS station. The red dots are the identified outliers, while the green dots are up coordinates after the outliers removal.

Lastly, the residuals were estimated.

<sup>1</sup>Some authors even refer to this rule for the definition of the outliers (e.g., Hekimoglu and Koch, 2000)

### 2.1.3 Offsets

When dealing with GPS coordinates time series and, in particular, with the Up coordinate, it can be seen that the series are characterized by linear, non-linear variations and sudden jumps. The last ones are offsets or discontinuities, which can be defined as a sharp change of the mean resulting in a long-lasting effect on the estimate of the station horizontal and vertical motions (Gazeaux et al., 2013).

If the discontinuities are not properly accounted for and removed, they will have a detrimental effect on position and velocity estimation and, therefore, will impact the proper understanding of the station motion.

Offset detection, also known as data segmentation or homogenization, is a problem investigated in a large number of scientific fields, from climate/meteorology (J. Gazeaux et al., 2011) to marketing (Fonf and DeSarbo, 2007), to geodesy, where the discontinuities detection and their magnitude evaluation play an important role.

In particular, the discontinuities affecting the GPS time series shall be treated carefully, since a not negligible percentage of offsets of unpredictable magnitude occurs at unknown epochs. However, a high percentage of offsets has a well known cause (Figure 2.4), and this allows to identify the epoch at which the *jump* took place. The most common causes for such discontinuities are: earthquakes, changes in the station equipment, antenna mounting problems, multipath<sup>2</sup>, vandalism and data analysis procedure (e.g., change of the reference frame). As shown in Figure 2.4, the main difference between offsets with known and unknown cause is within their full width at half maximum, which is higher for offsets generated by equipment change and seismic event than for offsets with unknown cause. For this reason, the latter are, in general, smaller than the other discontinuities making them especially difficult to detect.

The Nevada Geodetic Laboratory (NGL), from which the GPS data were obtained, provide for each site a list of epochs at which discontinuities occurred, but only if their causes are:

- equipment changes (antenna code, elevation cutoff, receiver type and model and random code change);
- earthquakes (for which a potential step record appears when the distance station-epicenter is less than  $10^{(\frac{M}{2}-0.8)}$  km, where  $M$  is earthquake magnitude);

---

<sup>2</sup>The interference by multipath is generated when a signal arrives, by different ways, at the antenna. Its principal cause is the antenna closeness to the reflecting structures, and it is important when the signal comes from the satellite with low elevation.

<sup>3</sup>The Scripps Orbit and Permanent Array Center, <http://sopac.ucsd.edu/>.

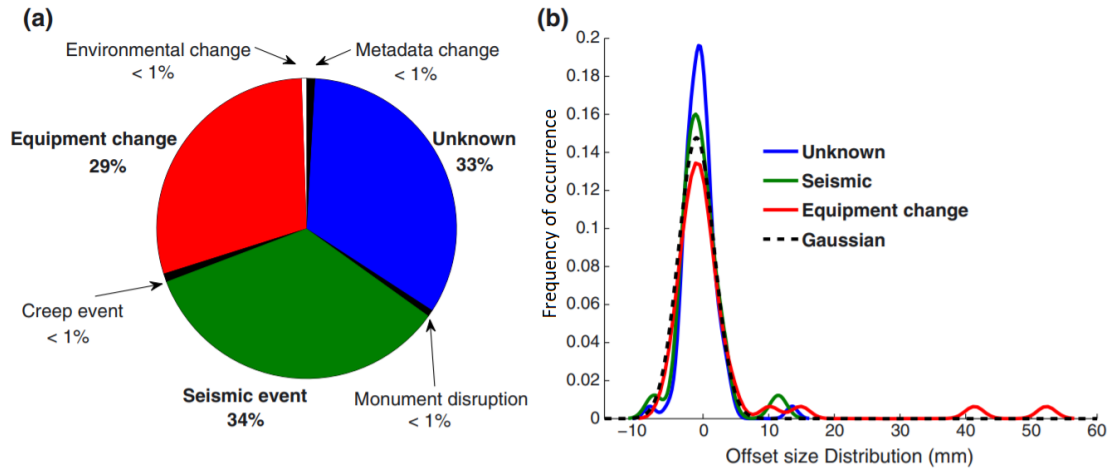


Figure 2.4: SOPAC<sup>3</sup> offsets characterization since 1995 over 340 sites (560 offsets): type of offset (a); frequency of occurrence of offsets with a certain magnitude (b).

- change of reference frame (from IGB08 to IGS14, for the data used in this work).

Offsets with a different origin shall be detected with appropriate methodologies.

Once the epochs are known, it is possible to proceed by correcting the discontinuities. This was done for each *jump* identified at a generic epoch  $t$ , in 3 steps:

1. two 30-days windows were selected before and after occurrence of the discontinuity;
2. on each window separately, the parameters of a linear fit were evaluated;
3. called  $a$  ( the "after" window) and  $b$  (the "before" window) the values of the linear interpolation at the epoch  $t$ , the difference  $a - b$  is added to all the data taken before the time  $t$ .

Figure 2.5a shows an example of the presence of discontinuities. Panel b shows the time series after having removed the discontinuities. Figure 2.6 shows a case in which *jumps* are not clearly recognizable, but their impact is clear after the correction is applied.

Once the *jumps* were removed, residuals were calculated again and weekly means were estimated from the new time series. The mean was computed if and only if there were at least 3 data in a week, leading to the data distribution shown in Figure 2.1 (Section 2.1.1).

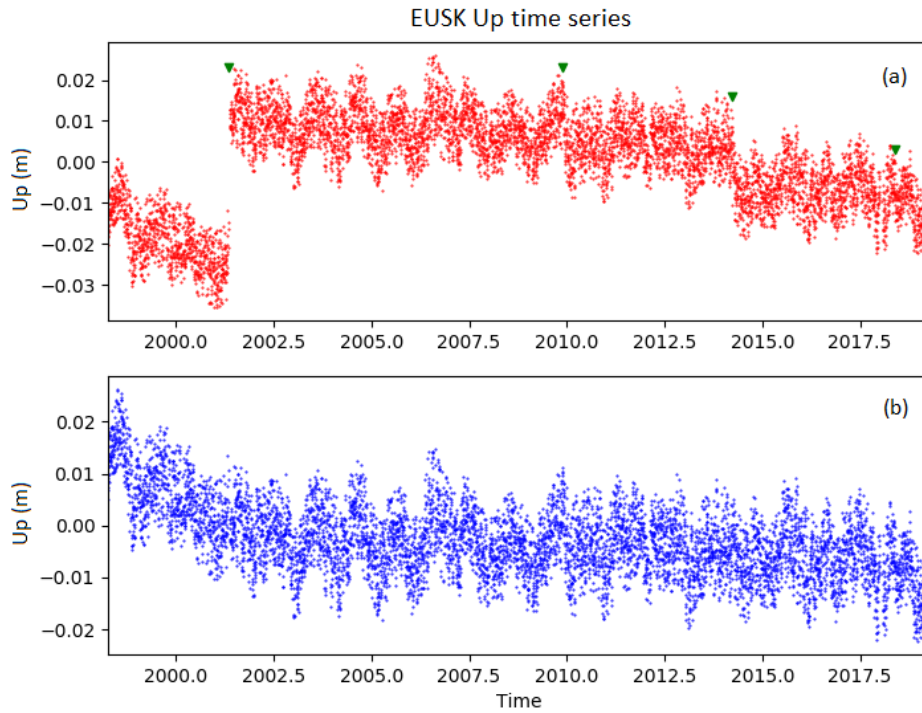


Figure 2.5: Up coordinate time series of the GPS station EUSK before ((a), red dots) and after ((b), blue dots) the offset correction. The green triangles identify the epochs of the discontinuities, corresponding to information given by the NGL.

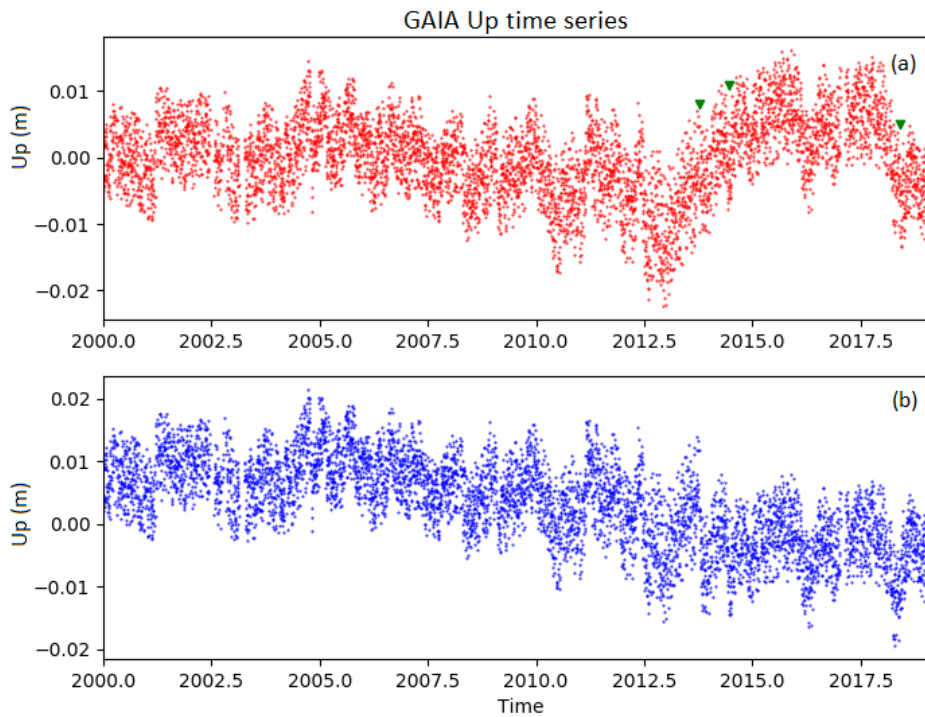


Figure 2.6: Up coordinate time series of the GPS station GAIA before ((a), red dots) and after ((b), blue dots) the offset correction. The green triangles identify the epochs of the discontinuities, corresponding to information given by the NGL.

### 2.1.4 Interpolation using PCA

The methodologies adopted to extract the main patterns of the space/time variability/co-variability of the various parameters are the Principal Component Analysis (PCA) and the Singular Value Decomposition (SVD) (Section 1.2). These, as well as the other standard multivariate techniques, are based on the eigendecomposition of a cross-product positive semi-definite matrix (e.g., correlation matrix) and thus require complete data sets. If there are missing data, performing PCA (or SVD analysis) may or may not lead to a positive semi-definite correlation matrix, i.e. the eigenvalues can be negative. Therefore, when facing the problem of deciding which spatial patterns and time patterns are relevant, the selection criteria can no longer rely on the magnitude of the eigenvalues (Section 1.2.1), but should also take into account the effect of the negative eigenvalues (Beckers and Rixen, 2003).

Time series of GPS coordinates are often characterized by missing observations, therefore a particular attention is needed during the statistical analysis and the use of PCA. Different strategies are envisaged to apply PCA on incomplete data sets. The most common approach is to discard those time series with missing observations and perform standard PCA (Dray and Josse, 2014). According to this approach, GPS Up coordinate time series which have just one missing value should not be taken into account. Considering that almost all the series are characterized by missing data, this would lead to a massive loss of information and would reduce the ability to detect common patterns. Another approach is to find, by applying appropriate algorithms, a proper estimate of the covariance matrix starting from incomplete data sets (Boscardin and Zhang, 2004), but they are heavy from the computational point of view (Ilin and Raiko, 2010). A third and final strategy consists in the imputation (i.e. the process of replacing missing data with substituted values) of missing values and then the application of PCA on the completed data set.

In this work, this last method (i.e. imputation of missing values) was adopted. The simplest approach to generate missing data is to provide values derived by the time averaging of the series. Other methods are based on iterative algorithms, for example the Papoulis-Gerchberg algorithm (Gerchberg, 1974; Papoulis, 1975) and the Expectation Maximization algorithm (Roweis, 1998), which are the most commonly used. However, the iterative characteristics of these methods, with the relevant computational burden, and the low convergence rates, preclude their use in a number of applications (Oliveira and Gomes, 2009). As a consequence, Oliveira and Gomes (2009) developed a more sophisticated procedure: a non-iterative methodology for the interpolation of signals with missing data supported by the PCA method. This approach is based on the following assumption:

**Assumption** *The missing information on the multidimensional sampled signals are negligible and the available samples, in a number greater than the selected principal components, are representative of the original signal.*

This assumption is verified for the GPS Up coordinate time series used in this work, since the percentage of missing data does not exceed 4% of the total (except for the station SRJV, where 14% of data is missing).

To perform the interpolation, it is necessary first to define unbiased estimators for the mean and the covariance of the discrete time signals with missing data. Then the PCA-based interpolation, defined through these unbiased estimators, is performed carried out on a series-by-series basis.

#### 2.1.4.1 Mean and covariance estimators with missing data

The estimators for the mean and covariance generally used do not take into account possible missing values. Hence, new estimators must be introduced.

Consider a set of  $M$  signals (signals intended a time series of a generic nature)  $\mathbf{x}_i \in \ell_2$ , i.e. with finite energy, with  $i = 1, \dots, M$ , from a discrete time real-valued stochastic process corrupted by zero mean noise (e.g. a GPS Upcoordinate time series, Zanetti, 2007), represented as column vectors of length  $N$ . Consider also an indicator index  $\mathbf{l}(j)$ , with  $j = 1 \dots N$ , which is set to 1 if the  $j$ -th component of signal  $\mathbf{x}$  is available and zero otherwise. In the latter, the component  $\mathbf{x}(j)$  is set to zero without loss of generality.

**Lemma I** *Given a set of  $M$  signals  $\mathbf{x}_i$ , with associated indexes  $\mathbf{l}_i$ , and the auxiliary vectors of counter  $\mathbf{c} = \sum_{i=1}^M \mathbf{l}_i$  and  $\mathbf{C} = \sum_{i=1}^M \mathbf{l}_i \mathbf{l}_i^T$ ,*

- i) *the estimator for the  $j$ -th component of the ensemble mean  $\mathbf{m}_x(j)$ ,  $j = 1 \dots N$ ,*

$$\mathbf{m}_x(j) = \frac{1}{\mathbf{c}(j)} \sum_{i=1}^M \mathbf{l}_i(j) \mathbf{x}_i(j) \quad , \quad (2.1)$$

- ii) *the estimator for the covariance element  $\mathbf{R}_{xx}(j, k)$ ,  $j, k = 1 \dots N$ , given  $\mathbf{y}_i = \mathbf{x}_i - \mathbf{m}_x$ ,*

$$\mathbf{R}_{xx}(j, k) = \frac{1}{\mathbf{C}(i, j) - 1} \sum_{i=1}^M \mathbf{l}_i(j) \mathbf{l}_i(k) \mathbf{y}_i(j) \mathbf{y}_i(k)^T \quad , \quad (2.2)$$

*are unbiased and efficient*<sup>4</sup>.

---

<sup>4</sup>For the proof, see (Kay, 1993).

To be noted is the fact that the correlation matrix is proportional to  $\mathbf{y}_i(j)\mathbf{y}_i(k)^T$  and not to  $\mathbf{y}_i(j)^T\mathbf{y}_i(k)$ . In this case, the method is called PCA in *T-mode* (Compagnucci, Araneo, and Canziani, 2001) and is usually applied in order to analyse spatial fields in different times, while, the traditional method, also known as PCA in *S-mode*, involves the analysis of time series corresponding to different space-points and attempts to isolate subgroups of points that covary similarly (Richman, 1983, Richman, 1986).

#### 2.1.4.2 Solution to the interpolation problem

To solve the interpolation problem, consider that each signal  $\mathbf{x}_i$  is obtained from the original signal  $\mathbf{r}_i$  due to missing data, verifying the relation  $\mathbf{x}_i = \mathbf{L}_i\mathbf{r}_i$ . The matrix  $\mathbf{L}_i \in \mathbb{R}^{N \times n}$  is diagonal and filled with the indicator index  $\mathbf{l}_i$ . Consider also the following quantities:

- $\mathbf{U} = [\mathbf{u}_1\mathbf{u}_2 \dots \mathbf{u}_N]$ , the matrix composed by the  $N$  orthogonal column vectors of the basis which verifies the eigenvalue problem

$$\mathbf{R}_{xx}\mathbf{u}_j = \lambda_j\mathbf{u}_j \quad , \quad j = 1 \dots N \quad , \quad (2.3)$$

where  $\mathbf{R}_{xx}$ , the covariance matrix defined above;

- assuming that the eigenvalues  $\lambda_i$  are ordered (i.e.  $\lambda_1 \geq \lambda_2 \geq \dots \geq \lambda_N$ ) and that  $n \ll N$  is the number of chosen principal components,  $\tilde{\mathbf{U}} = [\mathbf{u}_1\mathbf{u}_2 \dots \mathbf{u}_n]$  is the matrix with dimension  $\mathbb{R}^{N \times n}$ , composed by the  $n$  eigenvectors  $\mathbf{u}$  associated with the first  $n$  eigenvalues  $\lambda$  (analogous to the PCA procedure illustrated in Section 1.2.1);
- $\mathbf{v} = \mathbf{U}^T(\mathbf{r} - \mathbf{m}_x)$ , the vector projection of  $\mathbf{r}$  in the basis defined by  $\mathbf{v}$  itself.

The interpolation procedure can be now formulated as finding  $\tilde{\mathbf{r}}_i$  that minimizes the weighted  $\ell_2$  norm of the error and the latter is computed as the estimation error on the components of the signal which are known:

**Lemma II** *Considering the original signal  $\mathbf{r}_i$ , from which there is only available a signal with samples indexed by  $\mathbf{L}_i$ , the optimal interpolated signal  $\tilde{\mathbf{r}}_i$  (in the minimum error energy sense) can be obtained solving the weighted least mean square problem*

$$\min_{\tilde{\mathbf{r}}_i \in \mathbb{R}^N} \|\mathbf{L}_i(\tilde{\mathbf{r}}_i - \mathbf{r}_i)\|_{2,\mathbf{W}}^2 \quad , \quad (2.4)$$

given the symmetric positive semi-definite weight  $\mathbf{W} \in \mathbb{R}^{N \times N}$ , where the solution based on PCA is given by

$$\tilde{\mathbf{v}}_i = (\tilde{\mathbf{U}}^T \mathbf{L}_i \mathbf{W} \mathbf{L}_i \tilde{\mathbf{U}})^{-1} \tilde{\mathbf{U}}^T \mathbf{L}_i \mathbf{W}^T (\mathbf{x}_i - \mathbf{L}_i \mathbf{m}_x) \quad , \quad (2.5)$$

which leads to the interpolated signal

$$\tilde{\mathbf{r}}_i = \tilde{\mathbf{U}} \tilde{\mathbf{v}}_i + \mathbf{m}_x \quad . \quad (2.6)$$

It can be also demonstrated that the optimal choice of the weight is  $\mathbf{W} = \mathbf{R}_{xx}^{-1}$  (Oliveira and Gomes, 2009, Kailath, Sayed, and Hassibi, 2000).

According to the Assumption, the minimization is well posed in the case where the expected number of samples available are greater than the selected number of principal components. Given  $\eta$ , i.e. the percentage of missing samples in the signal, the assumption translates into  $N(1 - \eta) > n$  and therefore into an interval of validity for the interpolation equal to:

$$0 \leq \eta \leq \frac{N - n}{N} \quad . \quad (2.7)$$

Remarkable is the fact that no limitation on the amount of missing data was found for the application of the method, even if the lower is the number of missing data, the greater is the number of main components that can be considered and the better is the quality of the interpolation.

### 2.1.4.3 Implementation and results

In Lemma I the number  $M$  of signals involved in the interpolation appears: they are signals generated by the same stochastic process and share the same time patterns. This implies that in order to perform the interpolation, each GPS Up coordinate time series has to be divided into a subset of  $M$  signals of length  $N$ , which are called *mosaics*. Let  $S$  be the length of the original signal (missing data included), then the number of *mosaics* is  $M = S - N + 1$ . If  $s_i$  is the value of the signal at the epoch  $t_i$ , the *mosaics* are organized as follows:

$$\begin{pmatrix} \mathbf{x}_1 \\ s_1 \\ s_2 \\ \vdots \\ s_N \end{pmatrix} \quad \begin{pmatrix} \mathbf{x}_2 \\ s_2 \\ s_3 \\ \vdots \\ s_{N+1} \end{pmatrix} \quad \cdots \quad \begin{pmatrix} \mathbf{x}_M \\ s_{S-N} \\ s_{S-N+1} \\ \vdots \\ s_S \end{pmatrix} \quad , \quad (2.8)$$

where each of the mosaics corresponds to the aforementioned signals  $\mathbf{x}_i$ .

Once the *mosaic* structure is obtained, the signal can be interpolated. The interpolation result is an ensemble of vectors  $\tilde{\mathbf{v}}_i$ , which are filtered in order to remove possible outliers, merged into a single signal of length  $S$  (through a weighted average on the number of missing data) and finally used to obtain the final signal (equation (2.6)).

The interpolation is repeated until there are no more missing data.

Figure 2.7 shows an example of the interpolation results: interpolated data (red dots) follow the same time pattern of the original ones (blue dots).

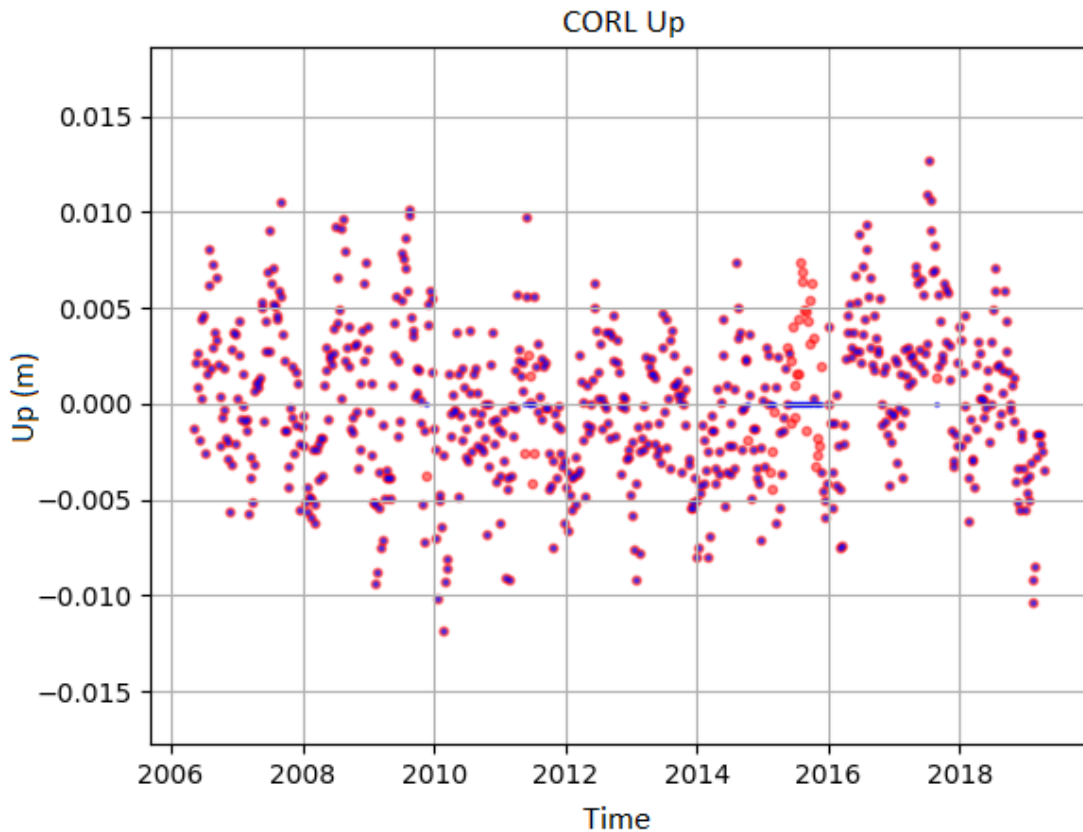


Figure 2.7: Example of interpolation of the Up position component of the GPS station CORL; red dots are interpolated data, blue dots are the original ones.

### 2.1.5 Seasonal variability of the GPS Up time series

The detection of the seasonal (annual) signal was the last step in the pre-processing of the GPS Up coordinate time series. The seasonal signal is a pattern that is generally present in each time series. For this reason, a mean annual cycle (as well as a linear trend) has to be removed, in order to identify the interannual variations of GPS Up time series.

To derive the annual signal, the GPS Up coordinate time series were analyzed according to the following procedure:

1. first, the outliers were removed;
2. a linear trend was estimated and removed. In this way a residual series was created;
3. the residual series was further analyzed to identify the presence of possible interannual signals. If present, they were removed by fitting a polynomial of appropriate order;
4. the residual series obtained in this way was used in a stacking procedure to generate the mean annual cycle.

The annual cycle thus computed was removed from interpolated GPS Up coordinate time series (2.1.4). These are the data used in the analysis described in the following chapters.

Figure 2.8 is an example which illustrates the steps of the procedure outlined above. It refers to the GPS Up coordinates of the DEVA station, located in Eastern Europe (Figure 2.2).

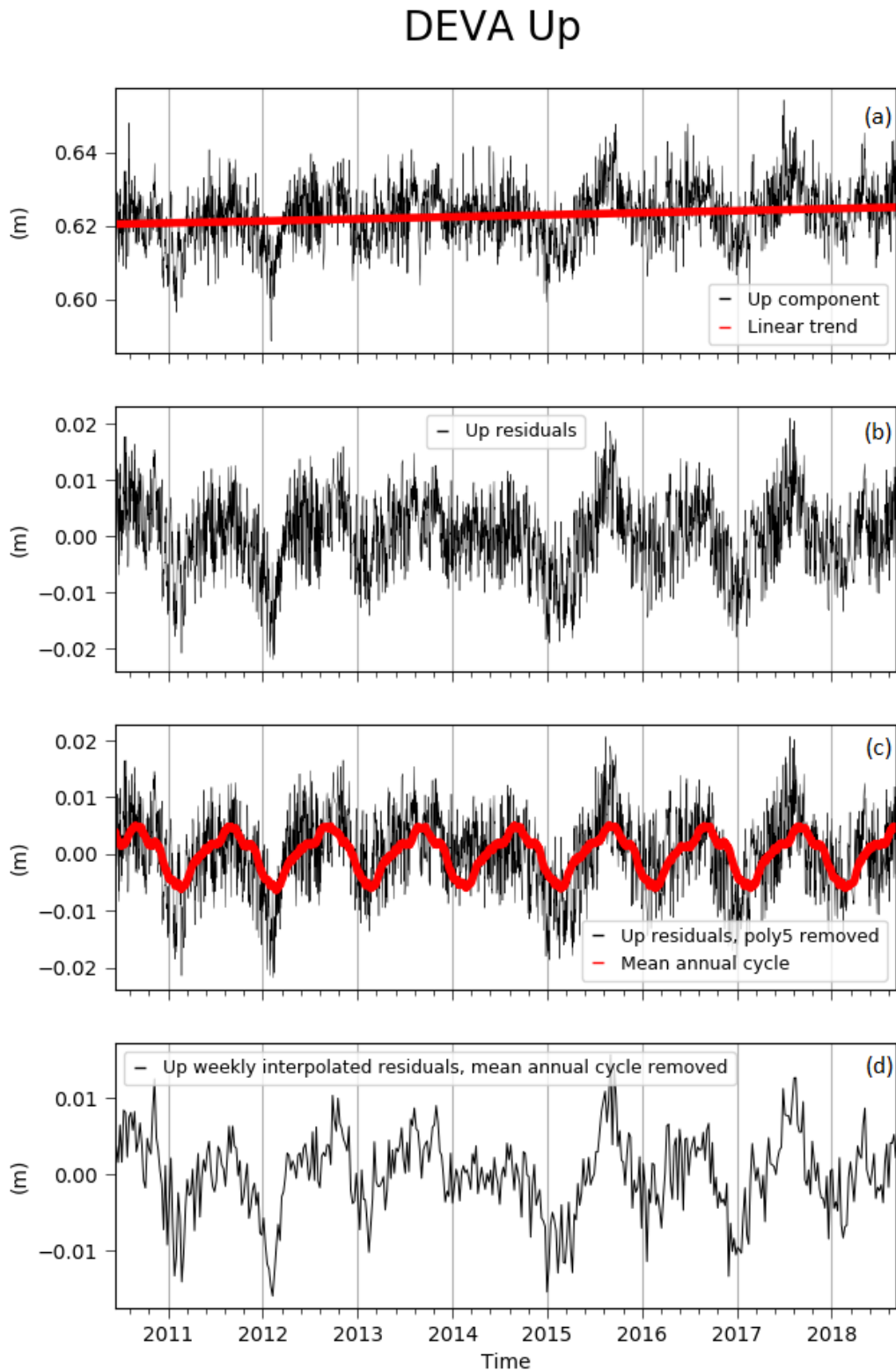


Figure 2.8: Steps of the deseasonalizing procedure applied to the time series of the GPS Up coordinate of station DEVA: (a) original series after having removed the outliers (black line), linear trend (red line); (b) the residual time series, where outliers and linear trend were removed; (c) the time series after removal of a 5th order polynomial (black line), mean annual cycle (red line); (d) weekly interpolated time series after removal of the linear trend and of the mean annual cycle.

## 2.2 Surface pressure and terrestrial water storage data

Surface pressure (SP) and terrestrial water storage (TWS) are the environmental parameters used in this study. The respective time series were derived from different sources described in the following.

### 2.2.1 Surface pressure (SP)

SP is the atmospheric pressure at a location on Earth's surface (terrain and oceans). SP time series used are the NCEP Daily Global Analyses over the period 2010-2019 on a  $2.5^\circ \times 2.5^\circ$  grid that covers the latitudinal range  $10^\circ$  W- $37.5^\circ$  E and the longitudinal range  $30^\circ$  N- $70^\circ$  N (Figure 2.10). NCEP daily SP is given in mb and values are of the order of  $10^3$  mb. Data are provided by the NOAA-ESRL Physical Sciences Division (PSD) from their Web site at <https://www.esrl.noaa.gov/psd/data/gridded/data.ncep.html> (NOAA/OAR/ESRL PSD, 1979 to present).

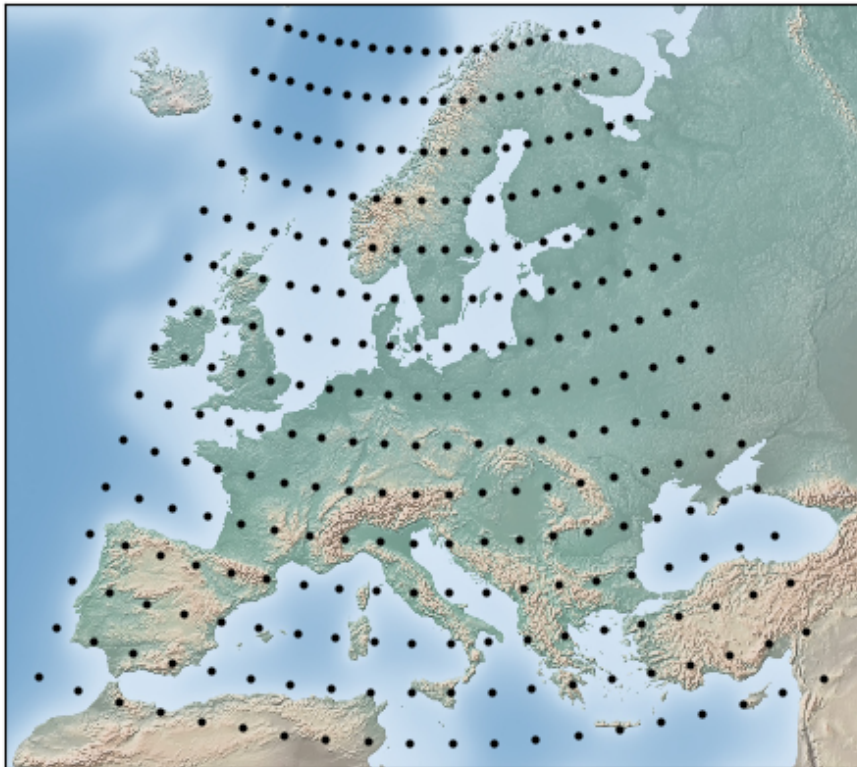


Figure 2.9: NCEP SP data grid.

Technically speaking, this is an analyzed data set, which is obtained from observational and model data. In fact, sampled observations are currently interpolated into a grid and analyzed through forecasting models in order to fill possible missing values due to the non homogeneous data coverage.

In this work, these SP data were interpolated in order to derive pressure values at the location of the 107 GPS sites (Figure 2.2). Then, the resulting time series were detrended and deseasonalized. Finally, weekly means were derived.

## 2.2.2 Terrestrial water storage (TWS)

The TWS can be defined as the summation of all water on the land surface and in the subsurface. It includes surface soil moisture, root zone soil moisture, groundwater, snow, ice, water stored in the vegetation, river and lake water (Giroto and Rodell, 2019).

The TWS data set used in this work is the "M2T1NXLND" (MERRA-2 `tavg1.2d.lnd_Nx`, V5.12.4, Global Modeling and Assimilation Office (GMAO), 2015), which is one of the products of Modern-Era Retrospective analysis for Research and Applications version 2 (MERRA-2), i.e. the project that places the NASA Earth Observation System (EOS) suite of observations in a climate context. These data are available on the NASA Goddard Earth Sciences (GES) Data and Information Services Center (DISC) Web site at <https://disc.gsfc.nasa.gov/>.

These data span over the period 2010-2019 and cover the same latitudinal and longitudinal ranges of the SP data. The daily TWS data are provided on a grid of spatial resolution  $0.5^\circ \times 0.625^\circ$  and were interpolated in order to obtain the values of TWS at the location of interest (Figure 2.2).

Lastly, the daily time series were detrended and deseasonalized and weekly time series were estimated.

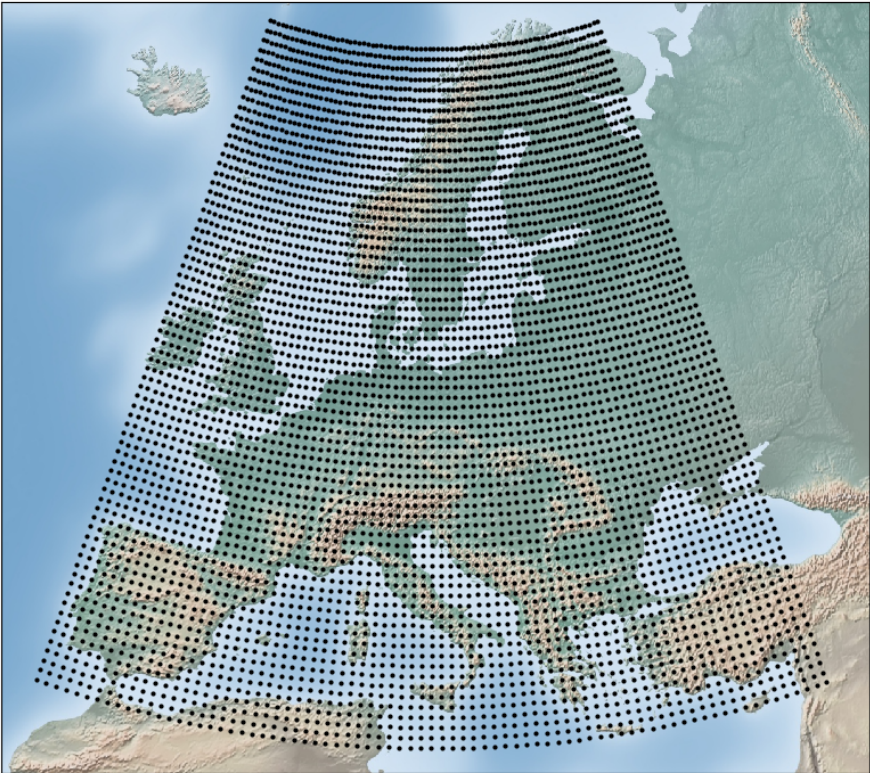


Figure 2.10: MERRA-2 TWS data grid.



# PCA analysis

---

3.1	PCA results . . . . .	33
3.1.1	GPS Up . . . . .	34
3.1.1.1	Two decades series . . . . .	35
3.1.2	Surface pressure (SP) . . . . .	47
3.1.3	Terrestrial water storage (TWS) . . . . .	54
3.2	SVD . . . . .	62
3.2.1	GPS Up coordinates and SP . . . . .	62
3.2.2	GPS Up coordinate and TWS . . . . .	67

---

In this chapter, the principal modes of variability of the GPS Up coordinate, surface pressure (SP) and terrestrial water storage (TWS) and their behavior will be described.

The Principal Component Analysis (PCA, Section 1.2) has been chosen to study the time series variability. This is not the only available approach, but it appears the most appropriate since the aim of this work is to compare the results with climate indices, that are also obtained from a PCA analysis (Chapter 4).

Coupling of different fields is explored via Singular Value Decomposition (SVD), which has the same mathematical basis as that of the PCA, but it is applied to two fields of variables.

## 3.1 PCA results

In this section are shown the results of the PCA analysis, performed on GPS Up coordinate, SP and TWS residuals.

As mentioned in Section 1.2.1, the three data sets are organized in three matrices where each column is a detrended, deseasonalized and standardized weekly time series. The correlation matrix was computed and from this the spatial pattern coefficients and the time components were derived.

The maps of the spatial pattern coefficients were obtained by assigning the proper value to the station point on the map, and then filling the map through a nearest neighbors interpolation, which returns the value at the data point closest to the point of interpolation. Furthermore, the spatial pattern coefficients were multiplied by 100, since they are always lower than 1. The plot color bar was created in such a way that the zero value is always in the middle of the bar. The spatial pattern coefficients and the time components are complementary and must be studied together.

### 3.1.1 GPS Up

The GPS Up time series were analyzed first. The most relevant are the first four modes of variability, which explain about the 50% of the total variability.

The first spatial pattern shows a rather homogeneous behaviour in the central European area and the Mediterranean, while Northern Great Britain, Ireland, and the Scandinavian zone are not characterized by the same behaviour (Figure 3.1). In particular, the station LOVJ shows a spatial pattern coefficient close to zero. The first time component (Figure 3.2) is characterized by high frequency oscillations and three pronounced slopes appear during 2011, mid 2015 and mid 2017. This time component explains the 28.65% of the total variance (Table 3.1): this is a significant amount, considering the large number of degrees of freedom (107).

The second spatial pattern shows a Northeast to Southwest gradient (Figure 3.3). Again, the station LOVJ seems anomalous. The second time component (Figure 3.4) shows a quasi decadal oscillation, where two anomalous peaks can be recognized: one around mid 2015 and the other in mid 2018. This component explains 11.60% of the total variance (Table 3.1), which is about one third of the first one.

The third spatial pattern (Figure 3.5) presents a gradient orthogonal to that of the second mode. It shows a positive maximum on the Great Britain side and a negative one over Southeastern Europe. The third time component does not show any particular behaviour and explains the 9.07% of the data total variability (Table 3.1).

The fourth spatial pattern (Figure 3.7) explains only a small percentage of the variance (4.17%, Table 3.1) and it shows a different pattern in Northern and Southeastern Europe. The fourth time component (Figure 3.8) shows a multi-annual oscillation, whose period varies from one to two years, superimposed over an oscillation of long period (3-to-4 years).

Figures 3.9 and 3.10 present two regionalization maps: different colours identify the different spatial patterns and each zone is coloured according to which one

Modes	Percentage of variance explained
1	28.65%
2	11.60%
3	9.07%
4	4.17%

Table 3.1: Percentage of variance explained by each mode of variability of the GPS Up coordinate data set.

best represents the relative GPS site. In Figure 3.9 the regionalization was created using all the four main spatial patterns. Central Europe is best described by the first mode, Scandinavia by the second, Great Britain and the Southeastern Europe by the third. The fourth mode instead does not identify a clear behaviour over the whole Europe. In Figure 3.10 the regionalization was created using only the first three spatial patterns and shows a behaviour similar to that of Figure 3.9. The main differences are in the Eastern part of the Adriatic, represented by the first mode, and in the Central Southern Italy and Eastern Spain, described by the second spatial pattern.

#### 3.1.1.1 Two decades series

The results previous shown might be sensitive to the time period taken into account and to the number of chosen time series. In order to verify if the spatial patterns and time components are affected from this bias, the PCA were applied on two decades GPS Up time series. In order to obtain at least a distribution of 40 GPS sites, the chosen time period goes from September, 19, 2001 to September, 5, 2018. In Figure 3.11 is shown the new distribution of stations. From figure 3.12 to figure 3.19 are shown the results of the PCA performed on these two decades time series.

The spatial patterns of the first three modes of variability (Figures 3.12, 3.14 and 3.16) exhibit the same behaviour of those obtained with the 107 time series (Figures 3.1, 3.3 and 3.5). The fourth spatial pattern (3.18) differs from the pattern shown in Figure 3.7 because is characterized by positive coefficients in Eastern Europe, France and the Iberian Peninsula, and by negative coefficients elsewhere.

In the time period between June, 6, 2010 and September, 5, 2018 the first three time components (Figures 3.13, 3.15 and 3.17) show the same behaviour as the previous ones, which were presented in Figures 3.2, 3.4 and 3.6. The fourth time component of the two decades GPS Up time series (Figure 3.19) show a completely different behaviour on the period between June, 6, 2010 and September, 5, 2018 with respect to the fourth time component in Figure 3.8, since is characterized by a

decreasing linear trend on which is superimposed a short period (annual/bi-annual) oscillation.

From this results, it is possible to infer that the first three modes of variability do not show neither a dependence on the length of the time period, nor a dependence on the number of stations selected. Conversely, the fourth mode of variability seems to be sensitive to the time period or the number of stations chosen.

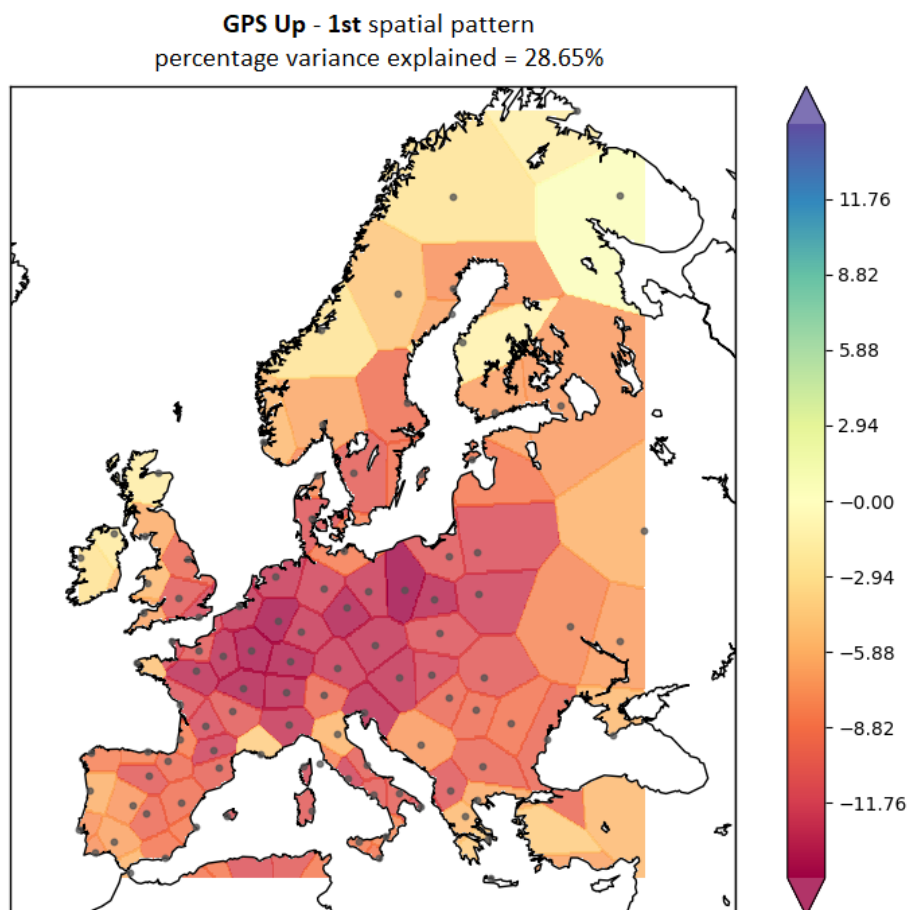


Figure 3.1: First spatial pattern of the weekly GPS Up coordinate residuals.

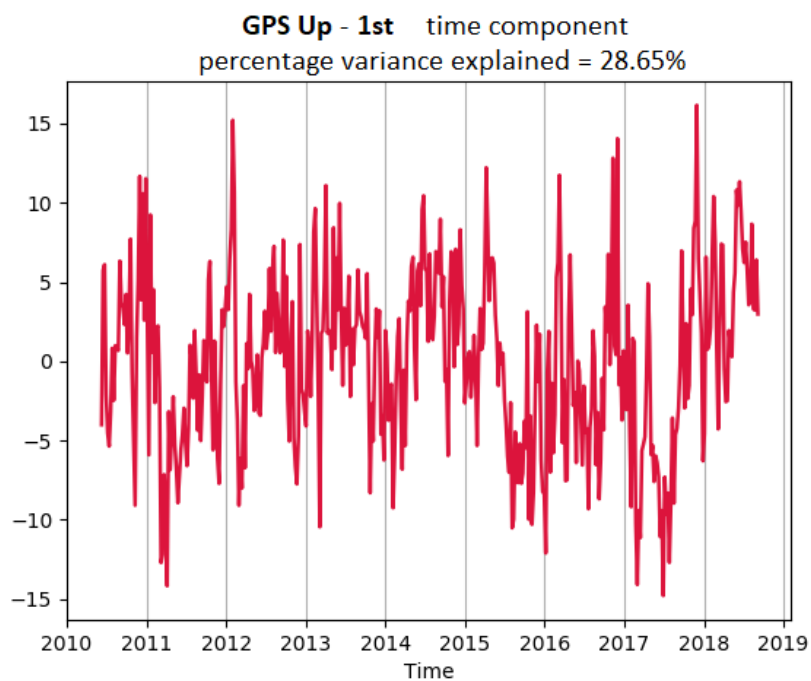


Figure 3.2: First time component of the weekly GPS Up coordinate residuals.

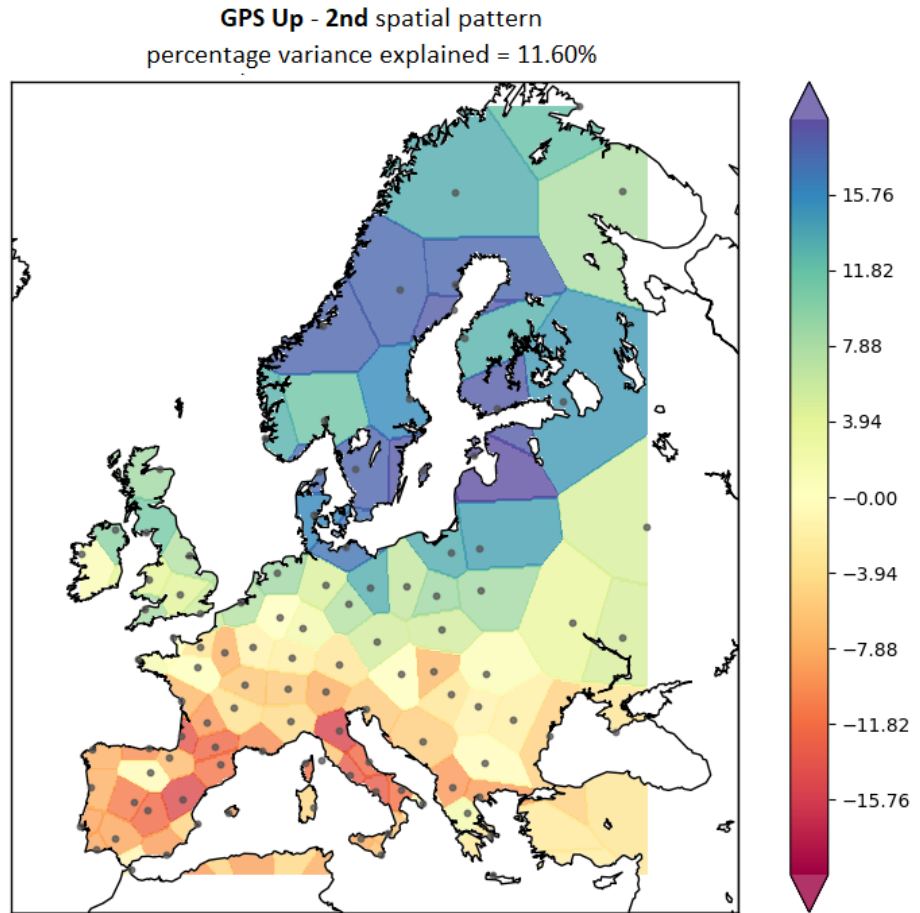


Figure 3.3: Second spatial pattern of the weekly GPS Up coordinate residuals.

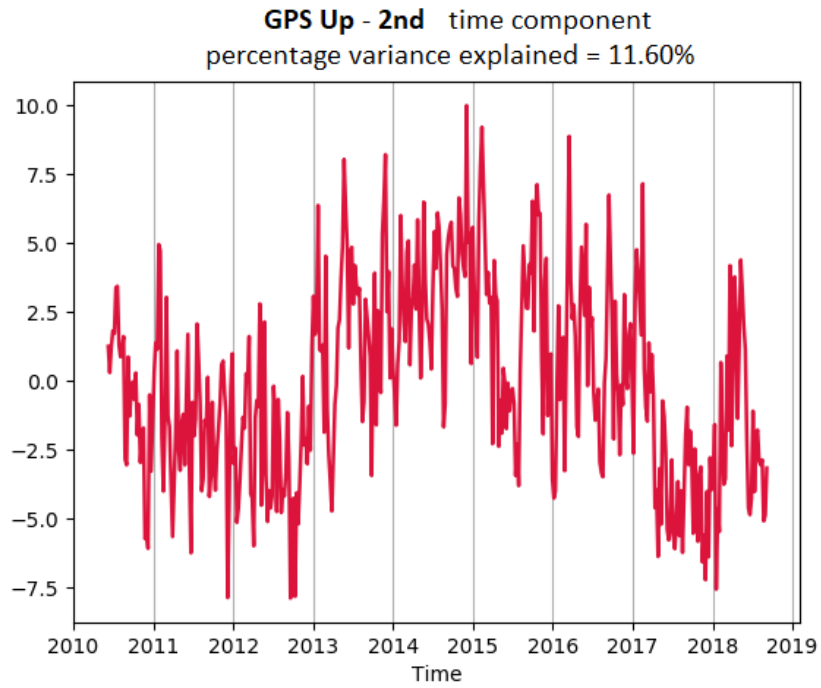


Figure 3.4: Second time component of the weekly GPS Up coordinate residuals.

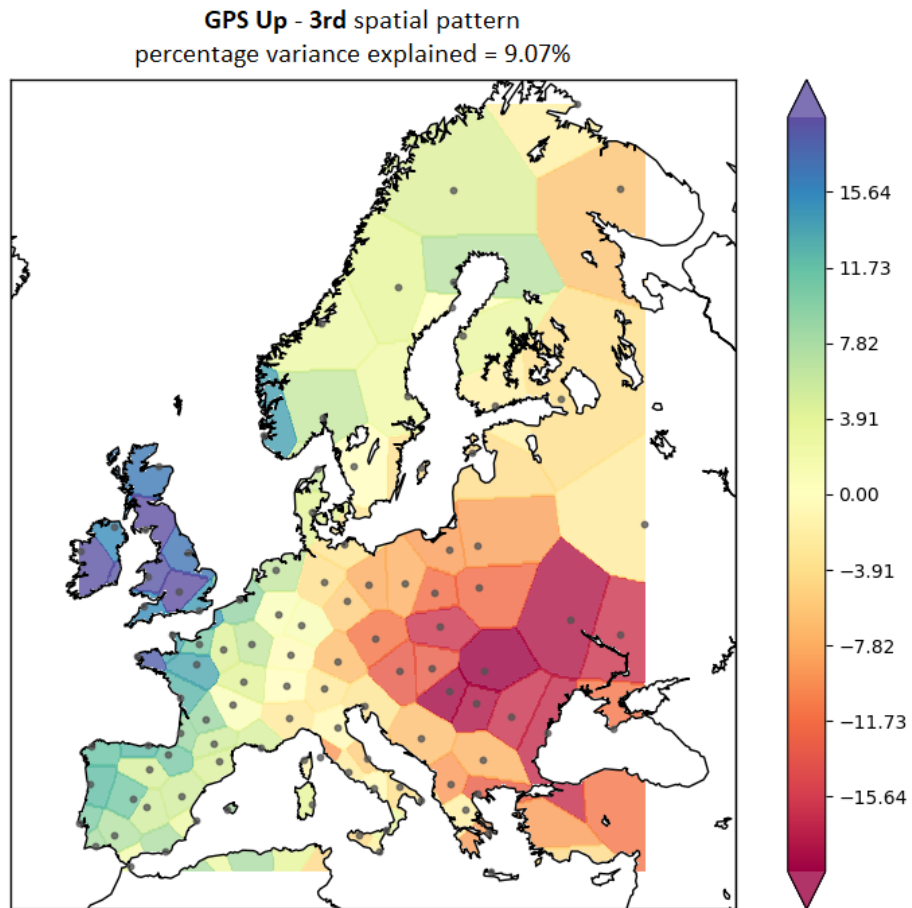


Figure 3.5: Third spatial pattern of the weekly GPS Up coordinate residuals.

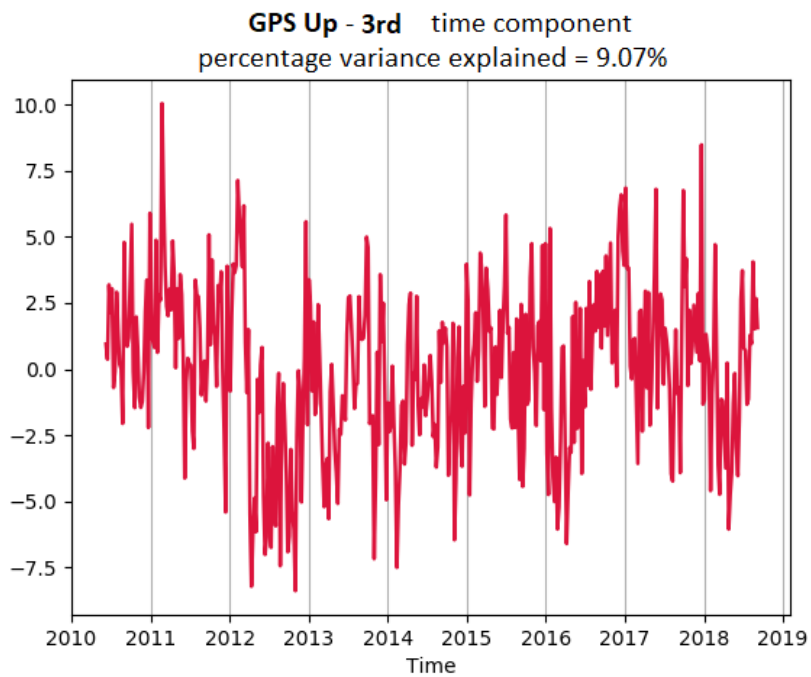


Figure 3.6: Third time component of the weekly GPS Up coordinate residuals.

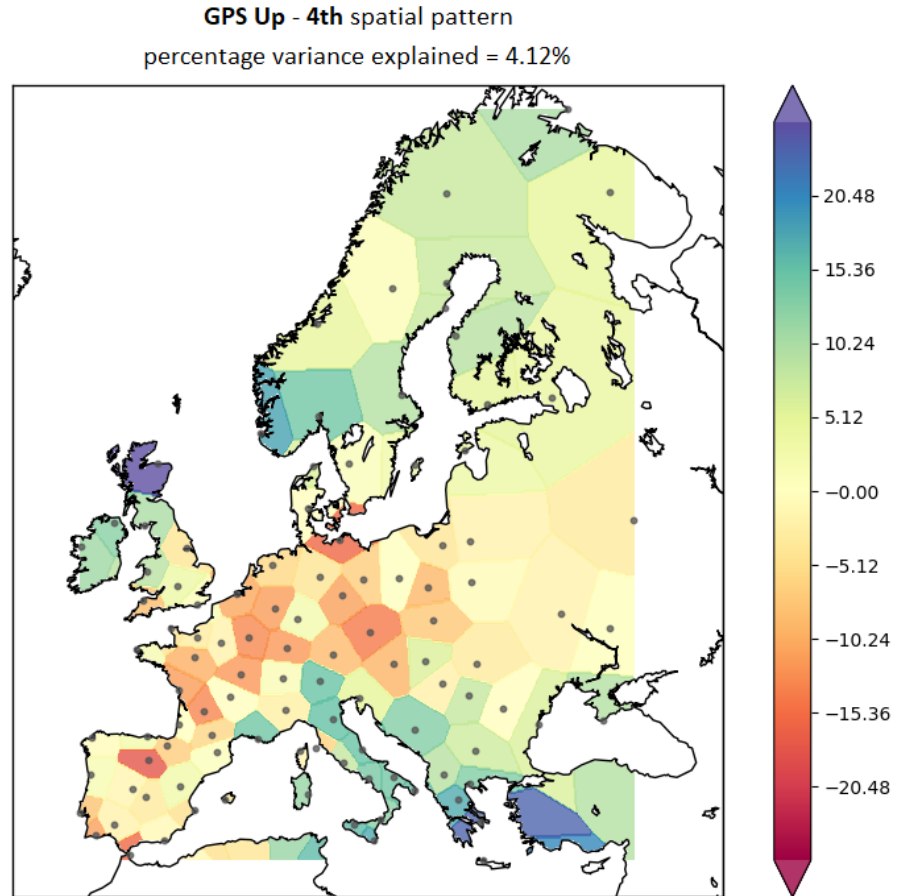


Figure 3.7: Fourth spatial pattern of the weekly GPS Up coordinate residuals.

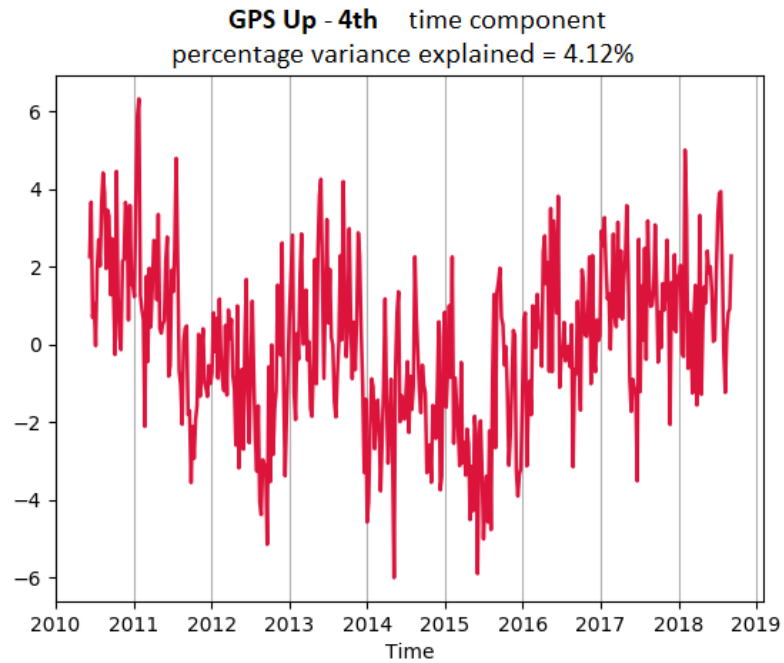


Figure 3.8: Fourth time component of the weekly GPS Up coordinate residuals.

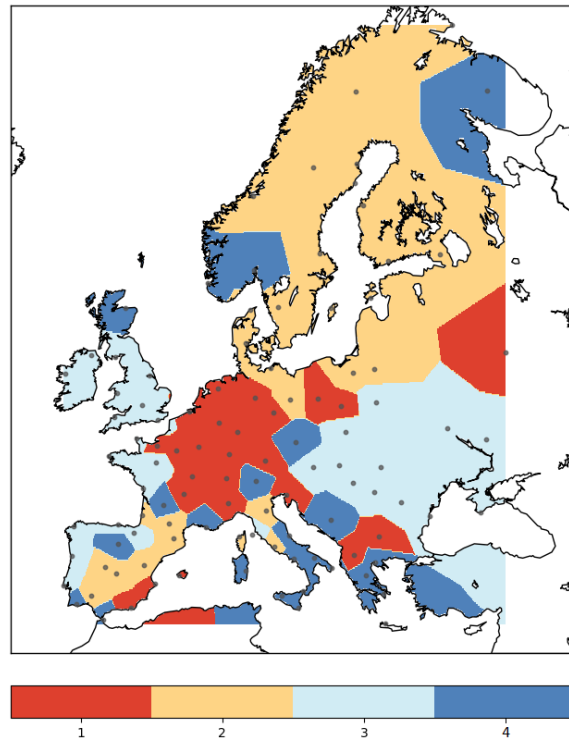


Figure 3.9: Regionalization map of the first four spatial patterns of the GPS Up coordinate residuals.

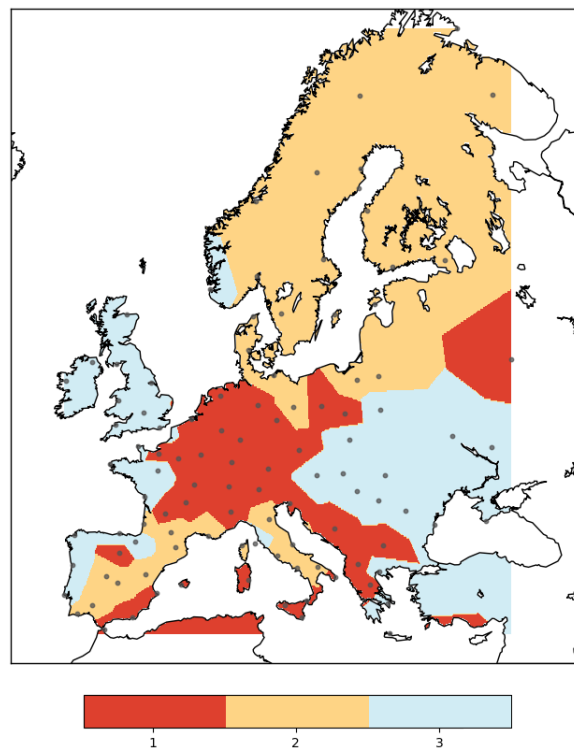


Figure 3.10: Regionalization map of the first three spatial patterns of the GPS Up coordinate residuals.

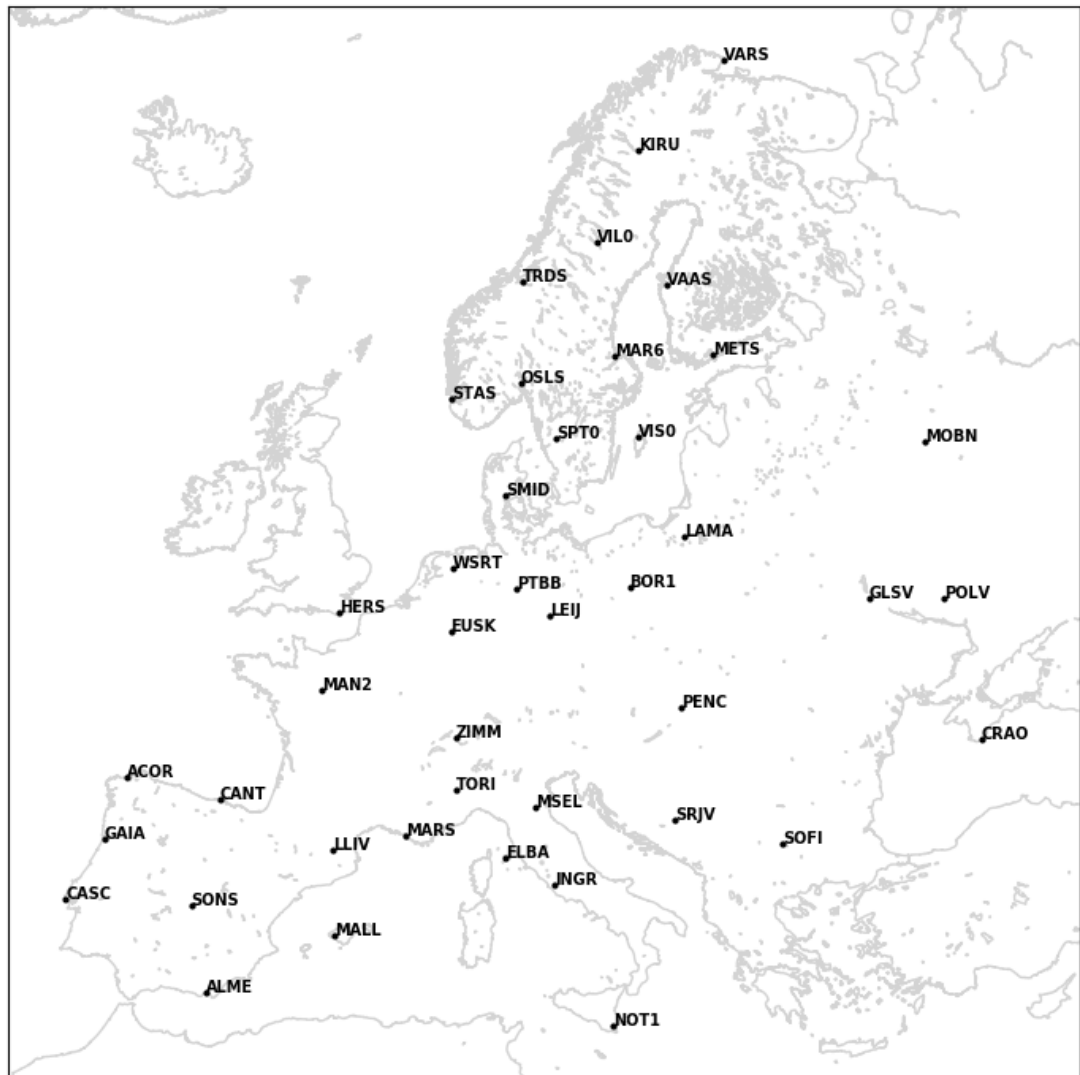


Figure 3.11: Location of the GPS stations related to the two decades time series.

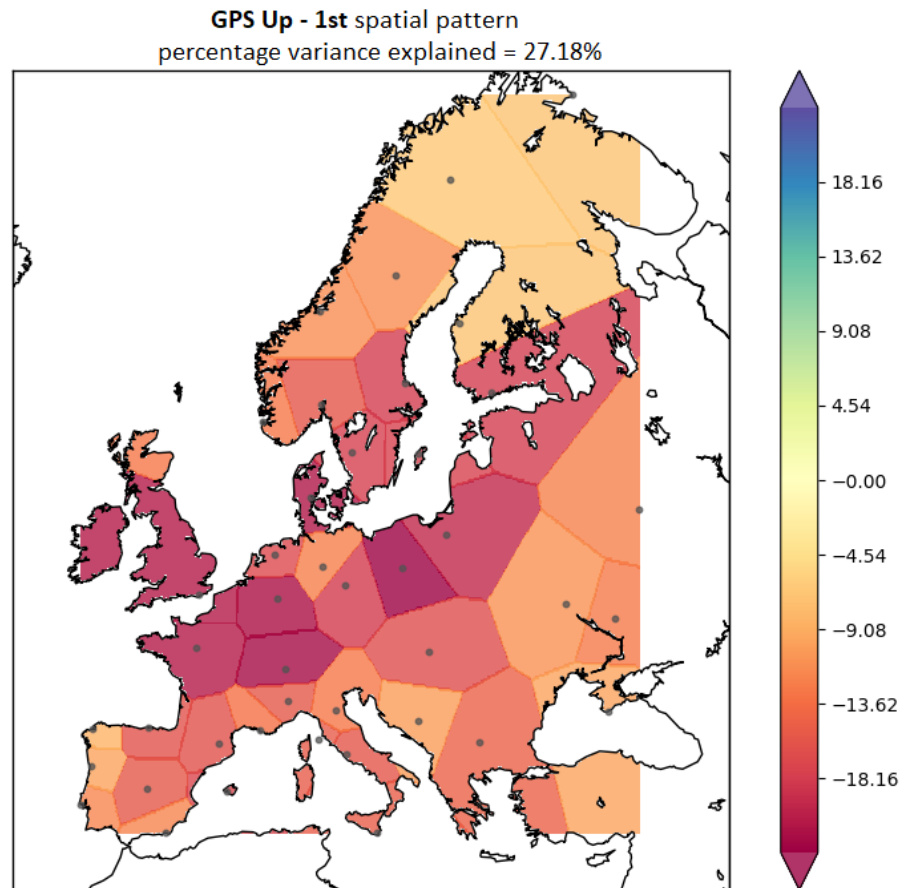


Figure 3.12: First spatial pattern of the two decades weekly GPS Up coordinate residuals.

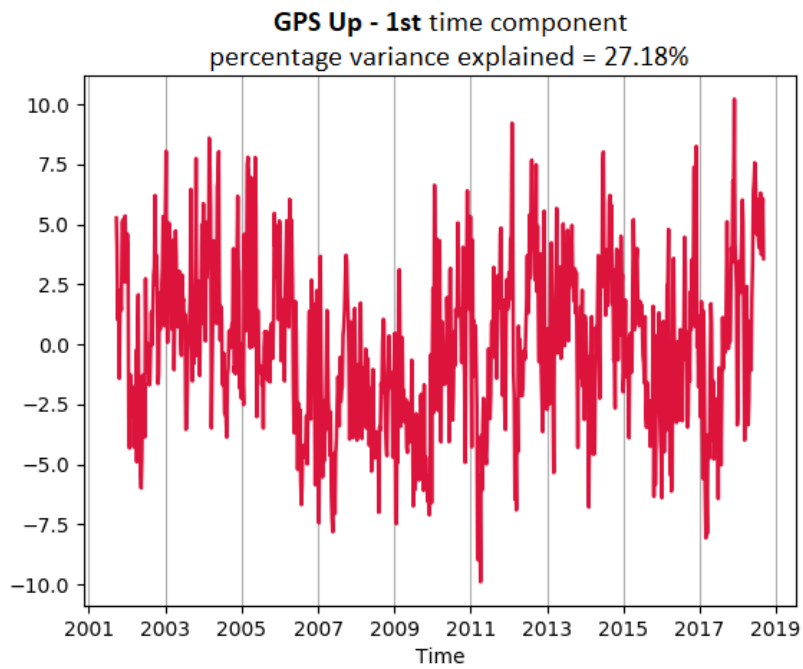


Figure 3.13: First time component of the two decades weekly GPS Up coordinate residuals.

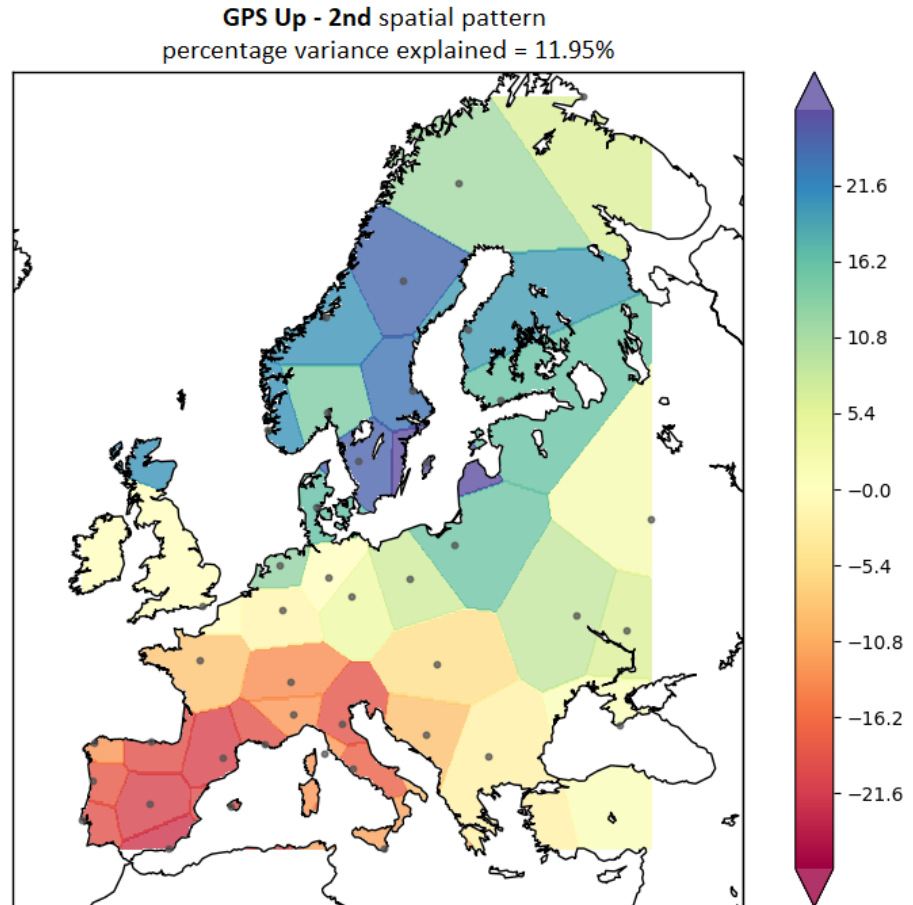


Figure 3.14: Second spatial pattern of the two decades weekly GPS Up coordinate residuals.

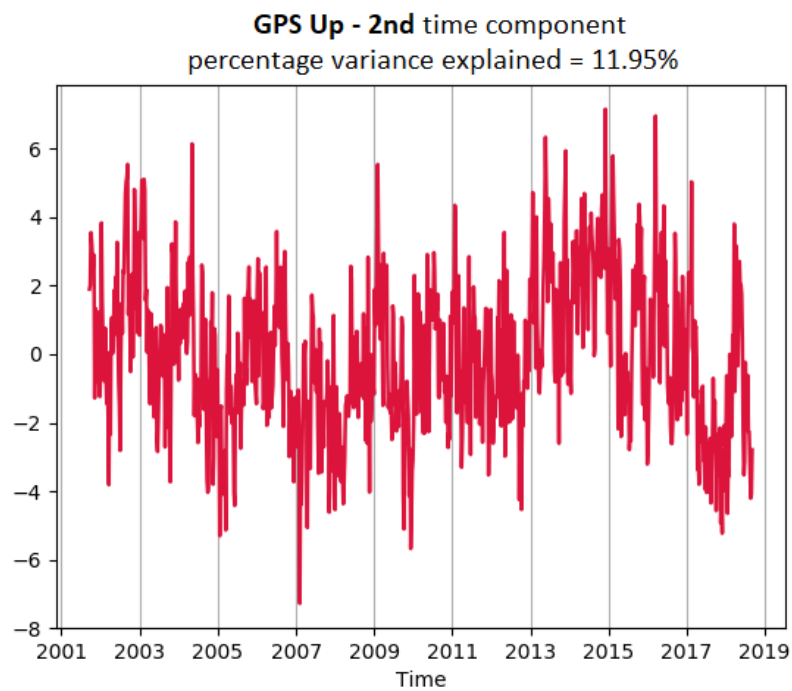


Figure 3.15: Second time component of the two decades weekly GPS Up coordinate residuals..

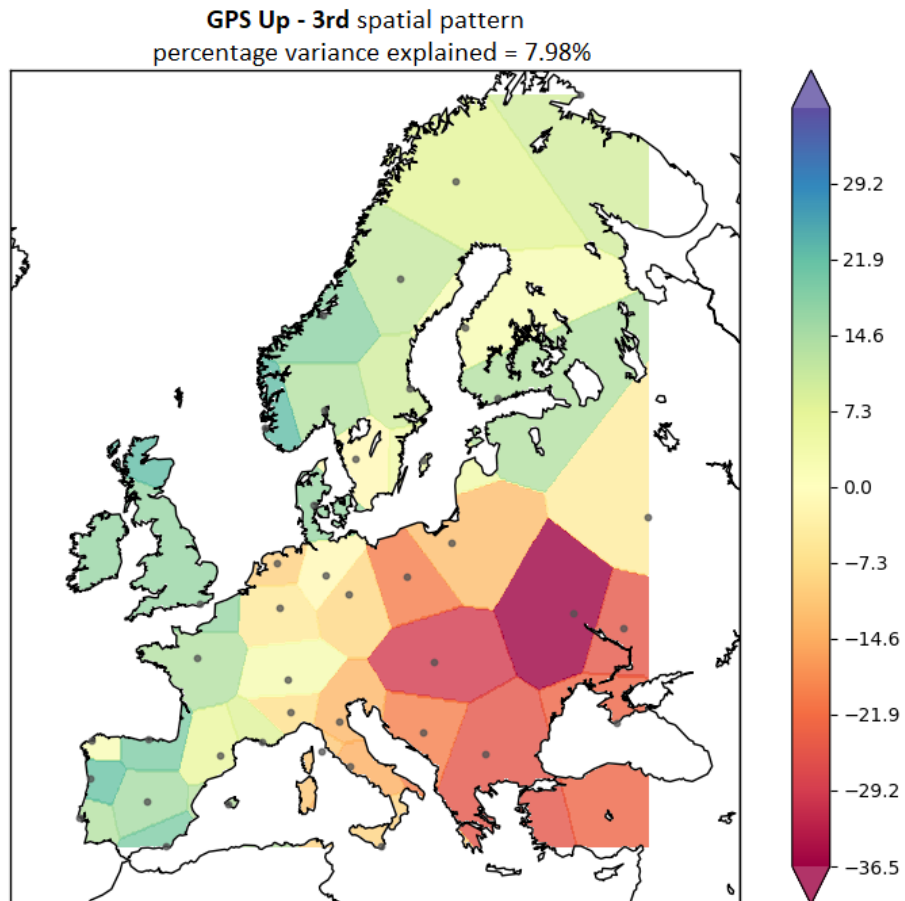


Figure 3.16: Third spatial pattern of the two decades weekly GPS Up coordinate residuals.

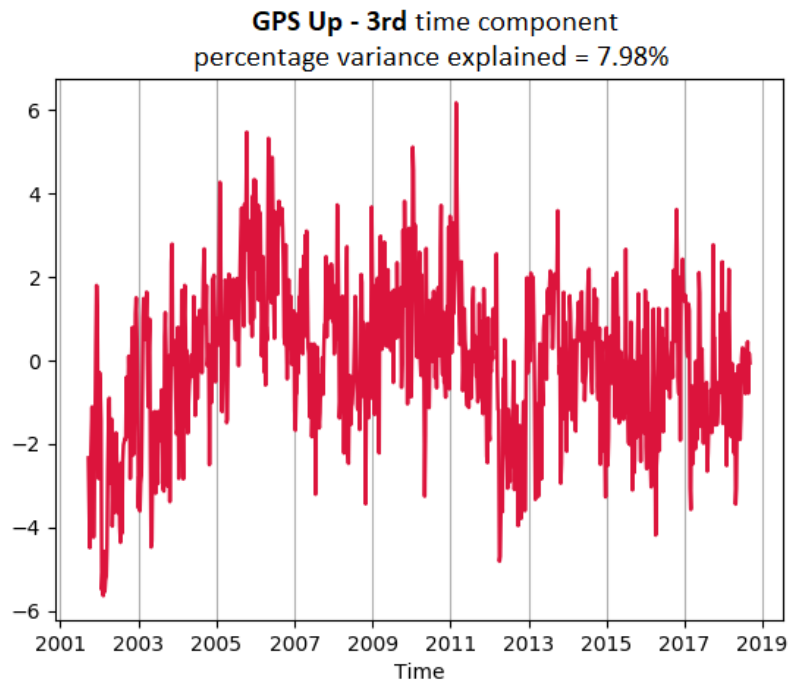


Figure 3.17: Third time component of the two decades weekly GPS Up coordinate residuals.

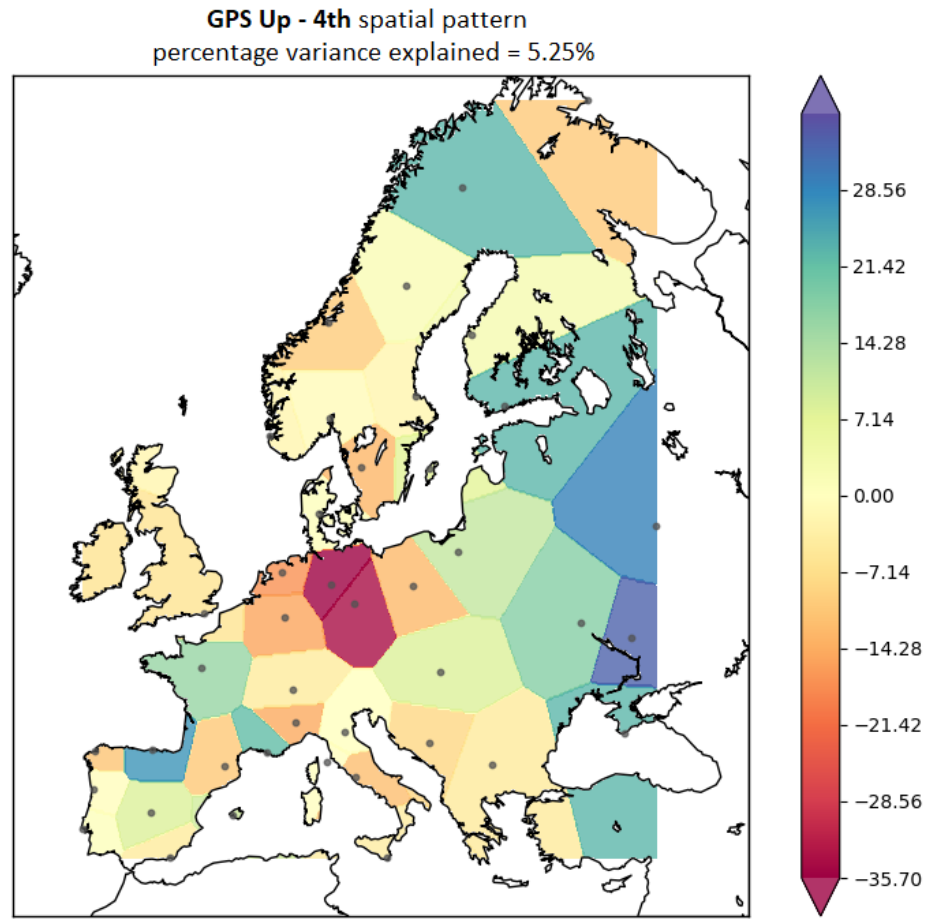


Figure 3.18: Fourth spatial pattern of the two decades weekly GPS Up coordinate residuals.

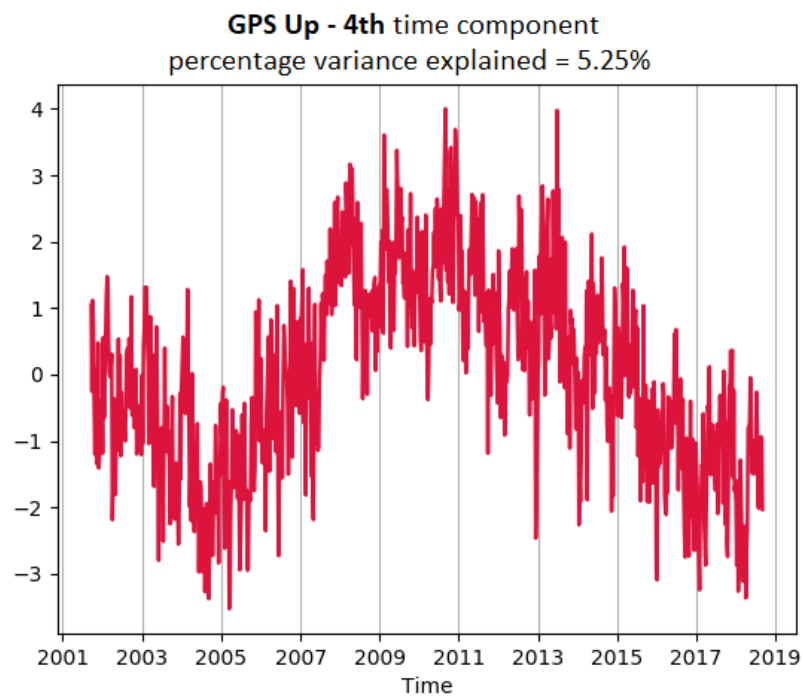


Figure 3.19: Fourth time component of the two decades weekly GPS Up coordinate residuals.

### 3.1.2 Surface pressure (SP)

The first four spatial patterns of the SP residuals explain almost 90% of the data variability; the first mode alone contributes 50% (Table 3.2). The time components, as well as the original data, are characterized by interannual variability, but also by very short period fluctuations. Thus, for graphical purposes only, the SP time components have been smoothed by using a 4-week adjacent averaging window.

The map of the first spatial pattern coefficients (Figure 3.20) shows a marked difference between the Northern, the Central and Southern part of the continent. Scandinavia and Northeastern Europe are characterized by values close to zero, while the rest of Europe and the Mediterranean are rather homogeneously represented by larger spatial pattern coefficients. The first time component (Figure 3.21) is characterized by positive and negative peaks. The negative peak at the beginning of the 2018 might be related to the anomalous cold weather conditions all over Europe that characterized the month of February 2018 (NOAA National Centers for Environmental Information, 2018d), related to an extratropical cold-core low<sup>1</sup>.

The map of the second spatial pattern coefficients shows a Northeast to Southwest gradient (Figure 3.22). The second time component (Figure 3.23) is characterized by a positive peak at the beginning of the 2012, which might be associated with the cold wave that started on January 27, 2012, and brought snow and freezing temperatures to much of the European continent. In fact, the cold weather was the result of an extensive area of very high pressure located over the north east of the continent (World Meteorological Organization (WMO), 2013). The second time component explains 21.86% of the variability (Table 3.2).

The map of the third spatial pattern coefficients presents a gradient orthogonal to that of the second mode (Figure 3.24). The coefficients are positive in Great Britain, Ireland, northern France, the Netherlands and north west Spain and Portugal, negative in Southeastern Europe. The correspondent time component (Figure 3.25), which explains 10.80% of the variance (Table 3.2), is characterized by an annual oscillation. An anomalous peak can be identified between the end of 2013 and beginning of 2014. In that period, namely December 17, 2013, and the February 14, 2014, the North East Atlantic and the British Isles were characterized by an exceptional negative pressure anomaly (S. Burt and T. Burt, 2019).

The map of the fourth spatial pattern coefficients (Figure 3.26) explains a small percentage of the variance (4.67%, Table 3.2). The coefficients are close to zero in Central Europe, positive over the British Isles and Southern Europe and negative

---

<sup>1</sup>An extratropical cold-core low is a low-pressure system which lies in the synoptic scale and occurs in mid-latitudes. Extratropical cold-core low are most of extratropical cyclones and are the result of the occlusions of the polar front, i.e. the interface between polar cold and tropical warm air.

over the Iberian Peninsula and Scandinavia. In the fourth time component (Figure 3.27), a long term oscillation might be recognized.

Modes	Percentage of variance explained
1	50.16%
2	21.86%
3	10.80%
4	4.67%

Table 3.2: Percentage of variance explained by each mode of variability of the SP data set.

In Figures 3.28 and 3.29 are shown the regionalization maps. In Figure 3.28 the regionalization was created using all four modes of variability. The resulting patterns are similar to the ones of the regionalization of the GPS Up coordinate residuals (Figure 3.9), in which Central Europe is best described by the first mode, while Scandinavia by the second, Great Britain and Southeastern Europe by the third. In this case, the fourth mode dominates in the Iberian Peninsula and in Northern Scandinavia. Figure 3.29 shows the map created using only the first three spatial patterns. In this case, Northern Scandinavia and most of the Iberian Peninsula are related to the second mode.

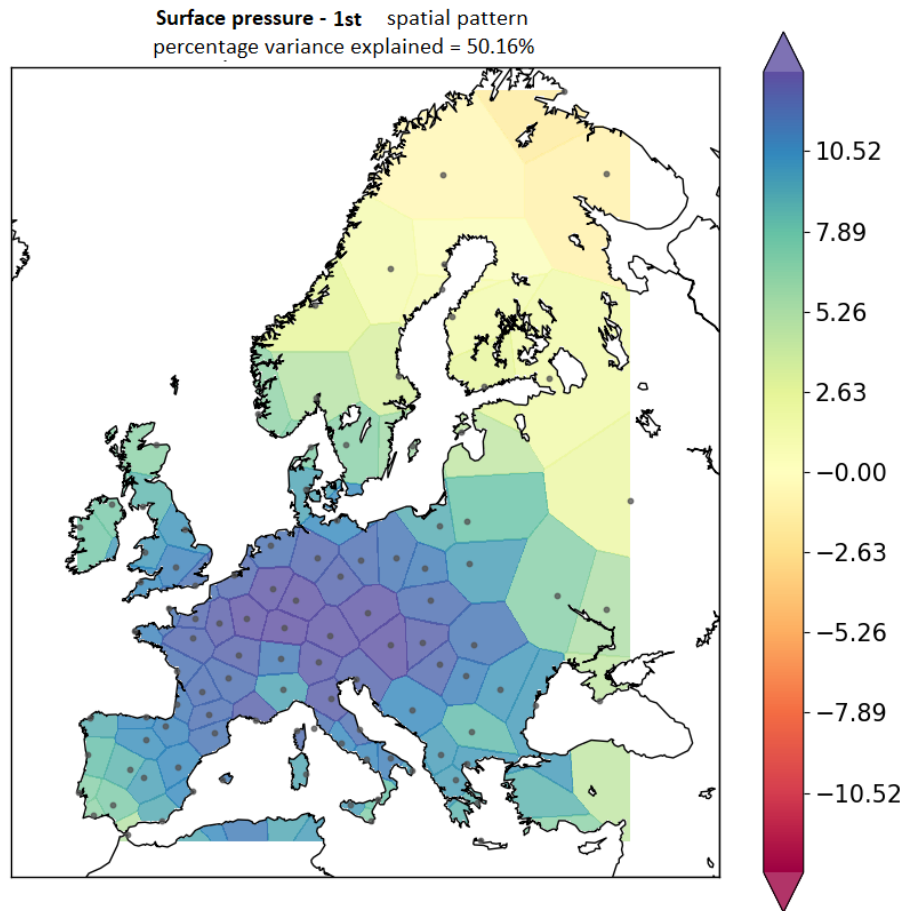


Figure 3.20: First spatial pattern of the weekly SP residuals.

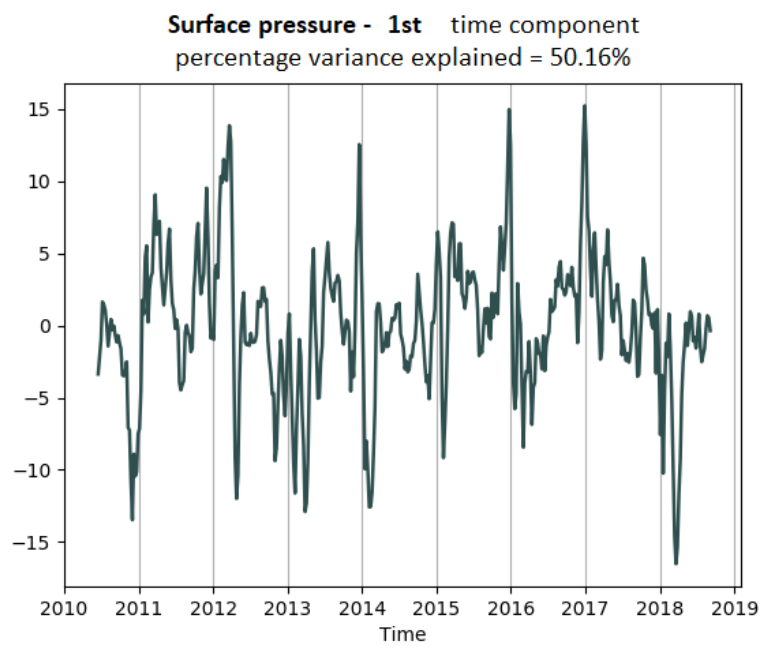


Figure 3.21: First time component of the weekly SP residuals.

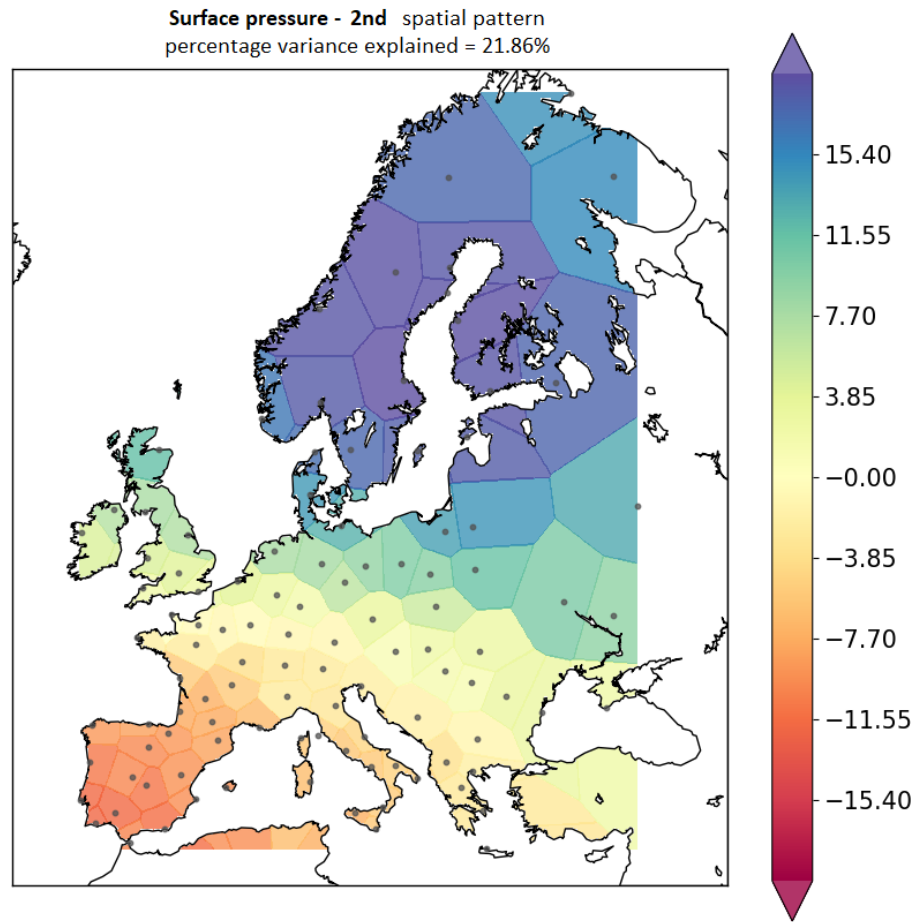


Figure 3.22: Second spatial pattern of the weekly SP residuals.

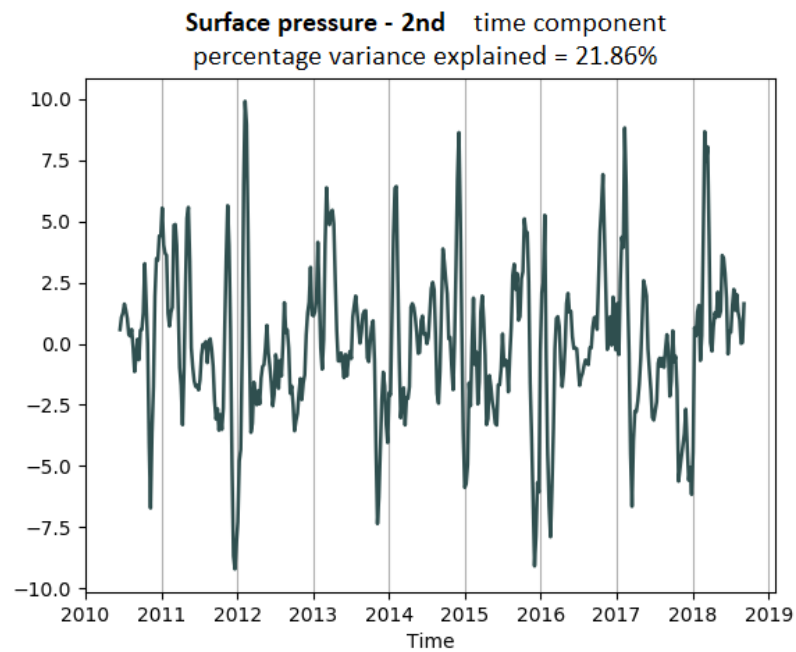


Figure 3.23: Second time component of the weekly SP residuals.

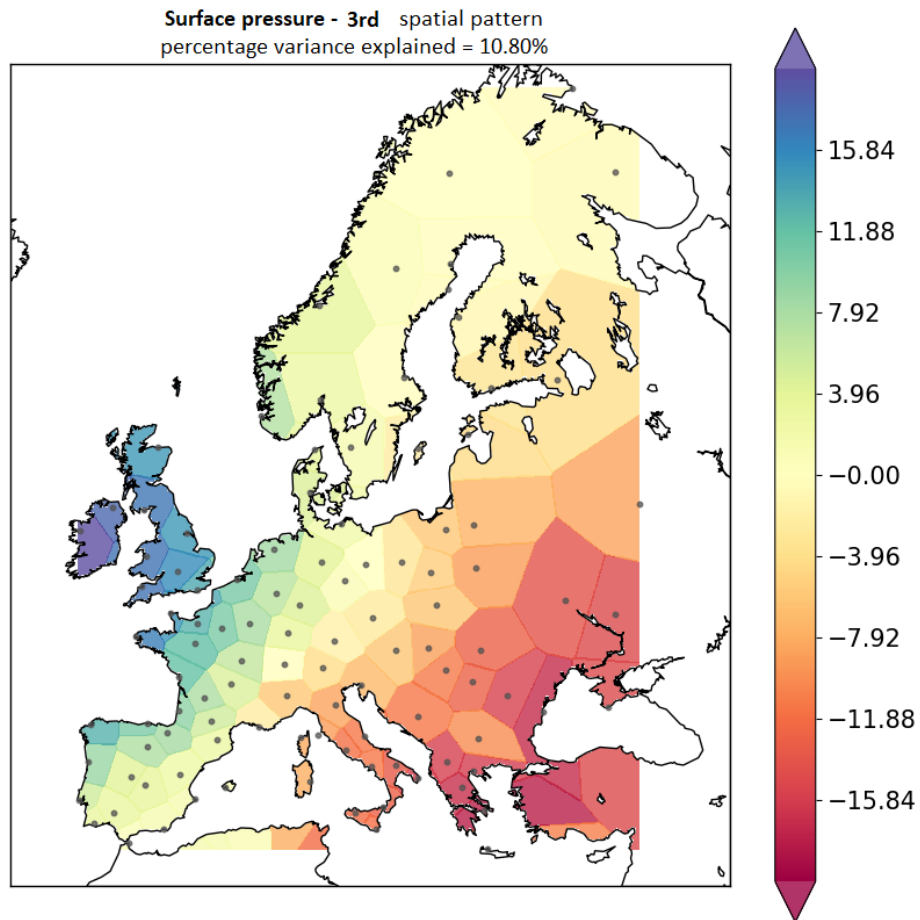


Figure 3.24: Third spatial pattern of the weekly SP residuals.

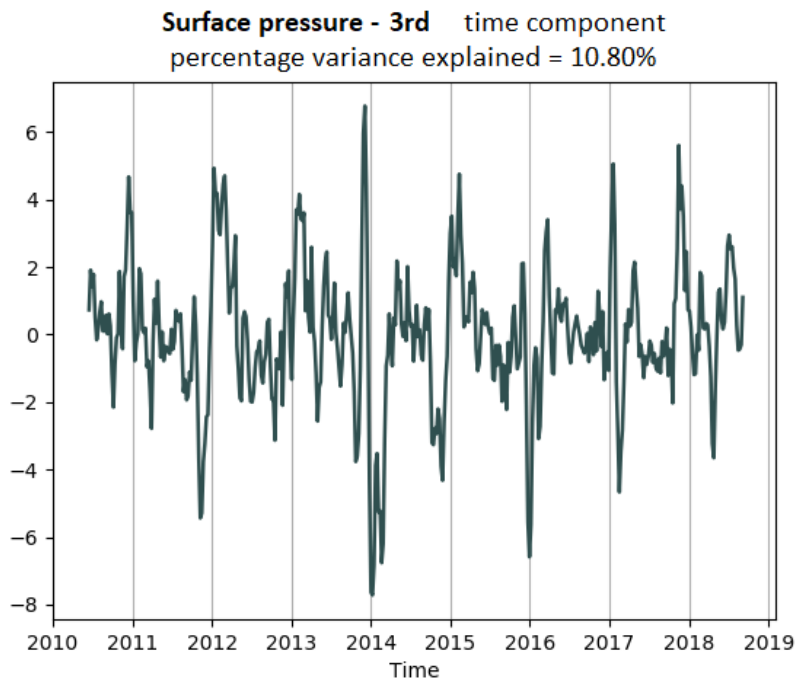


Figure 3.25: Third time component of the weekly SP residuals.

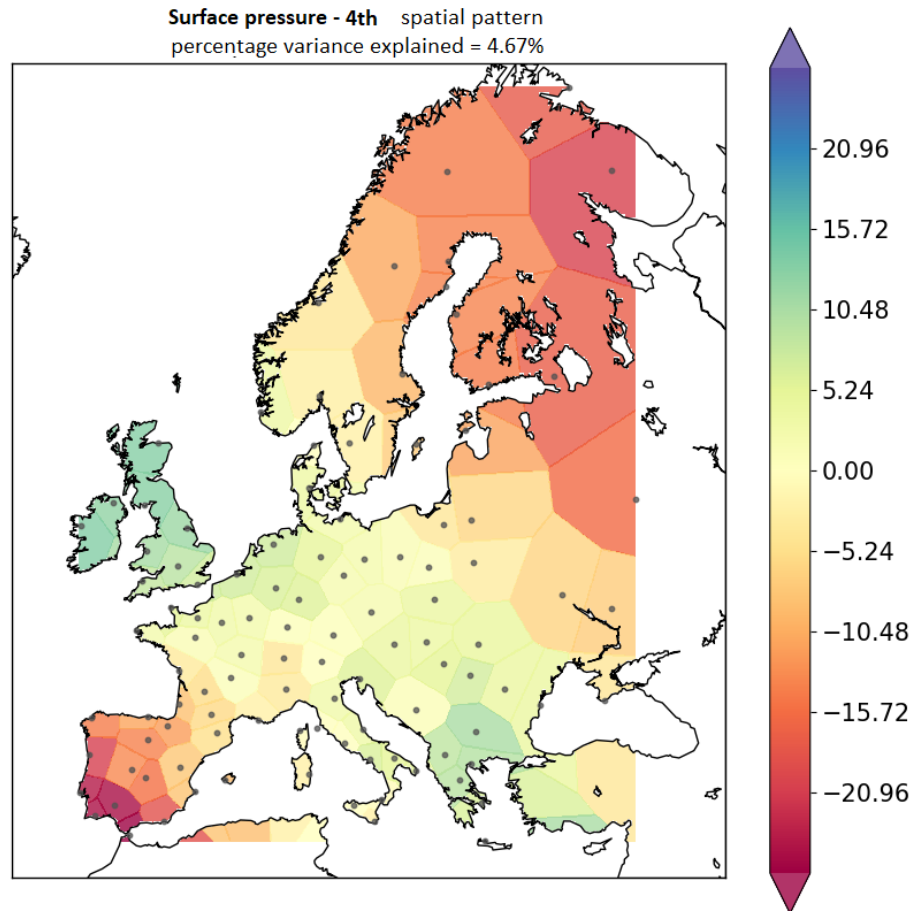


Figure 3.26: Fourth spatial pattern of the weekly SP residuals.

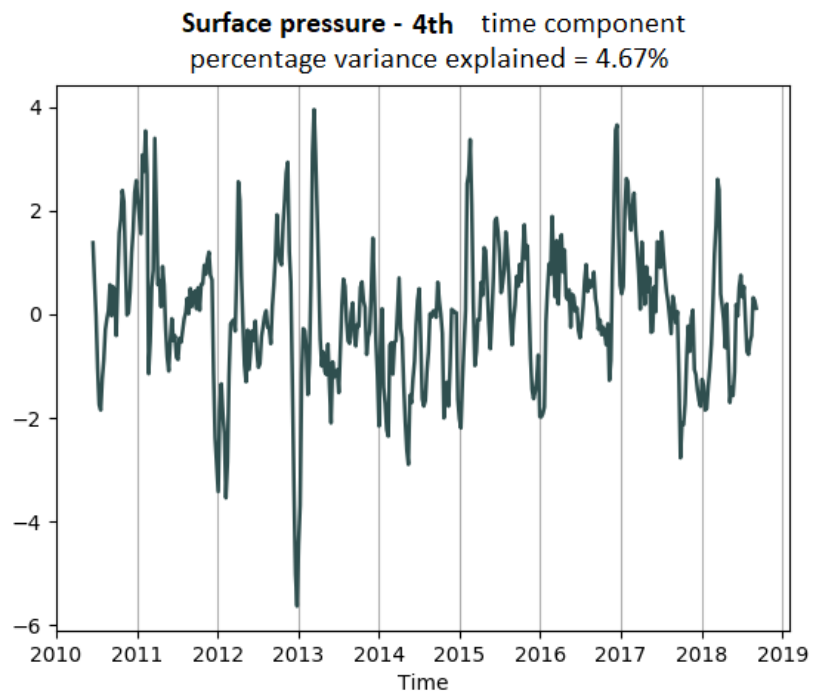


Figure 3.27: Fourth time component of the weekly SP residuals.

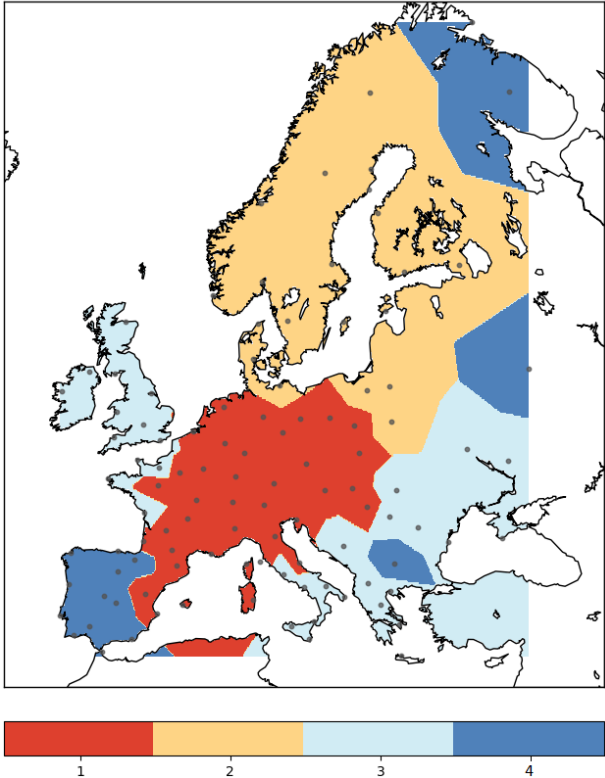


Figure 3.28: Regionalization map of the first four spatial patterns of the SP residuals.

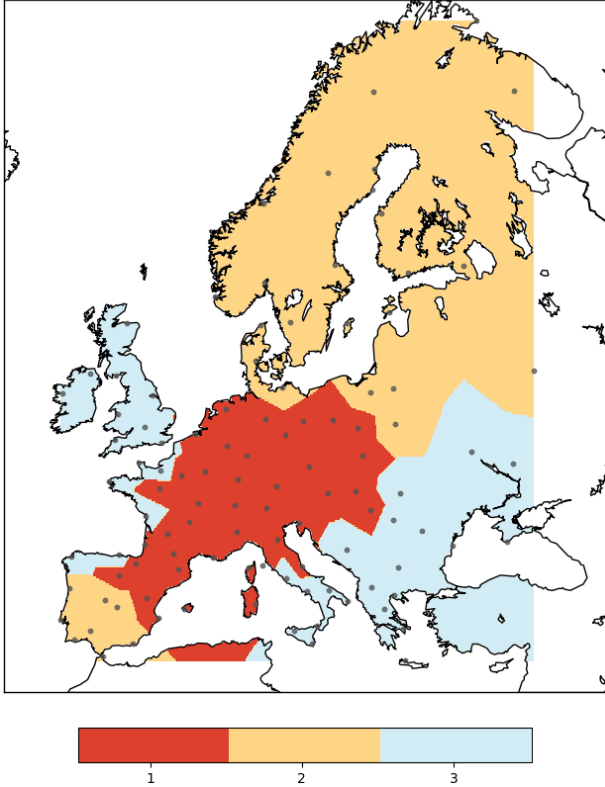


Figure 3.29: Regionalization map of the first three spatial patterns of the SP residuals.

### 3.1.3 Terrestrial water storage (TWS)

The first four spatial patterns of the TWS residuals explain almost 65% of the variance of the data set.

The map of the first spatial pattern coefficients (Figure 3.30) shows that the coefficients are positive all over Europe. In particular, the stations in Central and Southern Europe are characterized by larger magnitude of the first spatial pattern. The first time component (Figure 3.31), which explains 33.66% of the variance (Table 3.3), is characterized by a large oscillations, over periods of 1-to-2 years. A maximum value is recognizable in the beginning of the 2011 and a minimum in the first few months of the 2012. The 2011 maximum occurs after a period of heavy rainfalls. This period started in July 2010 and ended in December 2010<sup>2</sup>. In Figure 3.32 are shown the global precipitation anomalies relevant to November 2010. This month was characterized by the largest magnitude of the anomalies over Europe. The spring of 2011 was particularly dry in the western part of Europe, many areas of which received less than 40% of usual annual precipitation (Bissolli et al., 2012). In December 2011, drought conditions were basically confined to the Mediterranean area; from January to March 2012, the drought period first spread to Western Europe and then on Central and Southeastern Europe, where it peaked in March, i.e. when the minimum occurs in the first time component (Figure 3.31). The same explanation can be applied to the other minima and maxima. In fact, during the relevant periods, most Europe was affected respectively by severe drought or precipitation events, respectively.

The second TWS spatial pattern (Figure 3.33) is similar to the corresponding ones of the SP and of the GPS Up coordinate data sets (Figures 3.3 and 3.22). This spatial pattern shows a gradient from North-East to South-West and reaches the largest magnitude over the Scandinavia, the British Isles and the Iberian Peninsula. The second time component (Figure 3.34) shows a long-term oscillation on which are superimposed shorter period oscillations. It can be seen that:

- the minimum values correspond to a positive anomaly of the precipitation over the Iberian Peninsula, e.g. the minimum that occurs between mid 2014 and early 2015 (NOAA National Centers for Environmental Information, 2014);
- the maximum values correspond to a drought period in the Iberian Peninsula, e.g. the maximum that occur at the end of 2017 (NOAA National Centers

---

<sup>2</sup>NOAA National Centers for Environmental Information, 2018e; NOAA National Centers for Environmental Information, 2018a; NOAA National Centers for Environmental Information, 2018h; NOAA National Centers for Environmental Information, 2018g; NOAA National Centers for Environmental Information, 2018f; NOAA National Centers for Environmental Information, 2018b.

for Environmental Information, 2018c).

This time component explains 12.91% of the TWS data variability (Table 3.3), which is one third of the first one.

The third spatial pattern (Figure 3.35) presents a different behaviour with respect to the third spatial patterns of the SP and the GPS Up coordinate. South Britain and Northern France are characterized by the largest positive values, while the largest negative coefficients are identified in Eastern Europe. The third time component (Figure 3.36) explains the 11.04% of the variance (Table 3.3). A remarkable feature is a large oscillation over a period of about 6 years.

The map of the fourth spatial pattern coefficients map (Figure 3.37) explains about 7% of the total variance (Table 3.3) and it shows a pattern peaking positively in Eastern Europe and negatively in Ireland and northern Britain. The fourth time component, in general, is characterized by an annual oscillation. However, anomaly in this behaviour is recognized during 2013-2015, when the amplitude of the oscillation was large and the period was about 2 years. Figure 3.38 shows a relevant reduction of TWS from mid 2013 until the beginning of 2015. This shortage of TWS persisted during 2015 and this timing corresponds to the severe drought that affected Eastern Europe (Ionita et al., 2017; Boczoń et al., 2016).

Modes	Percentage of variance explained
1	33.66%
2	12.91%
3	11.04%
4	7.19%

Table 3.3: Percentage of variance explained by each mode of variability of the TWS data set.

The regionalizations are shown in Figures 3.39 and 3.40. The first one represents the first four spatial modes. The second concerns the first three ones. These regionalizations do not exhibit a clearly recognizable pattern. This might be attributable to a more local nature of the TWS with respect to that of the SP and of the GPS Up coordinate.

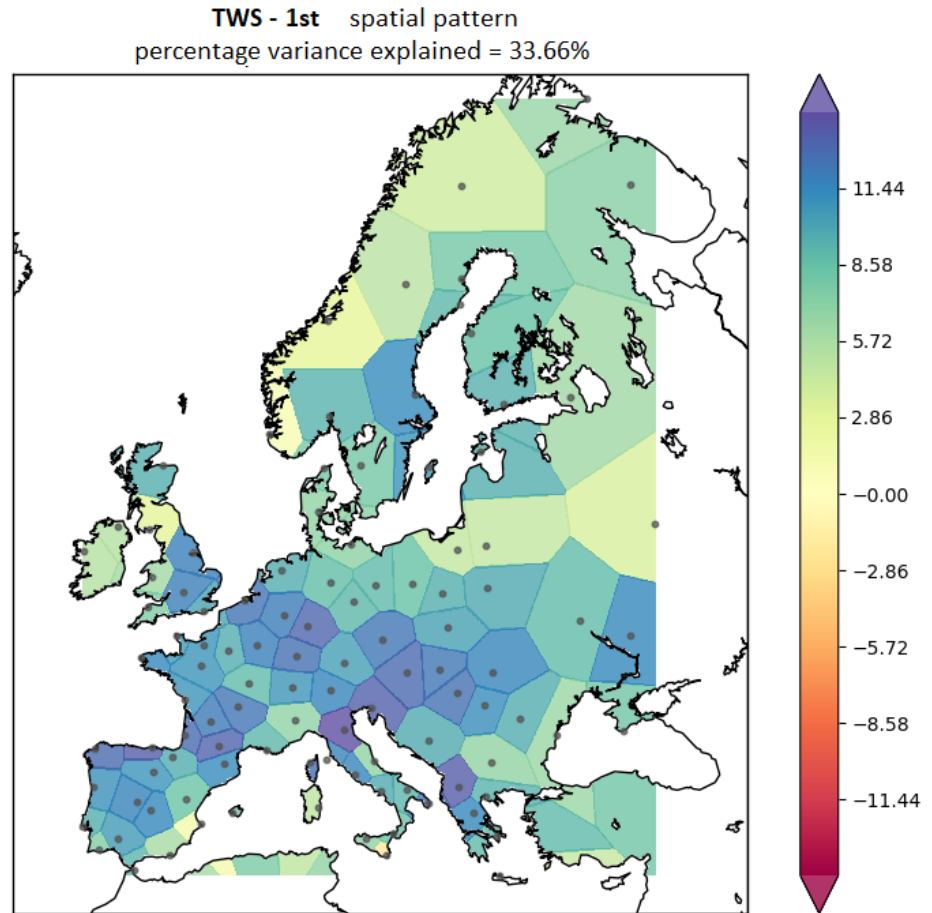


Figure 3.30: First spatial pattern of the weekly TWS residuals.

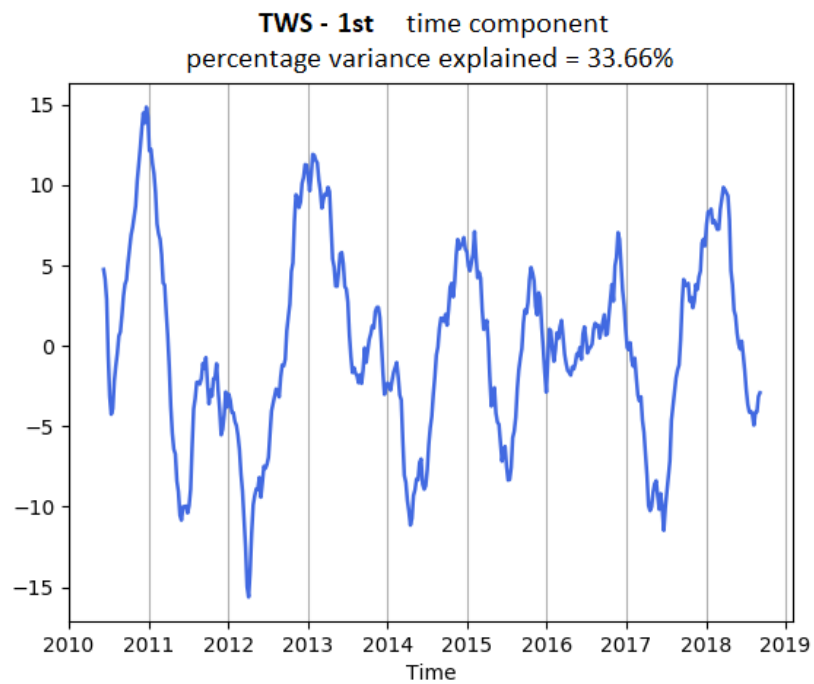


Figure 3.31: First time component of the weekly TWS residuals.

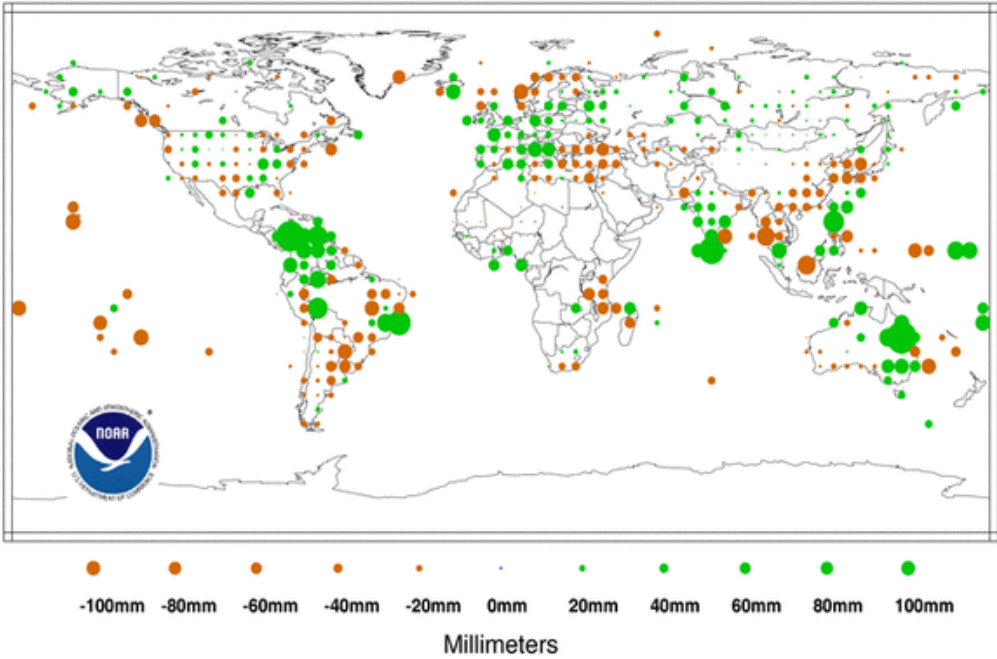


Figure 3.32: November 2010 Precipitation Anomalies in millimeters (NOAA National Centers for Environmental Information, 2018f).

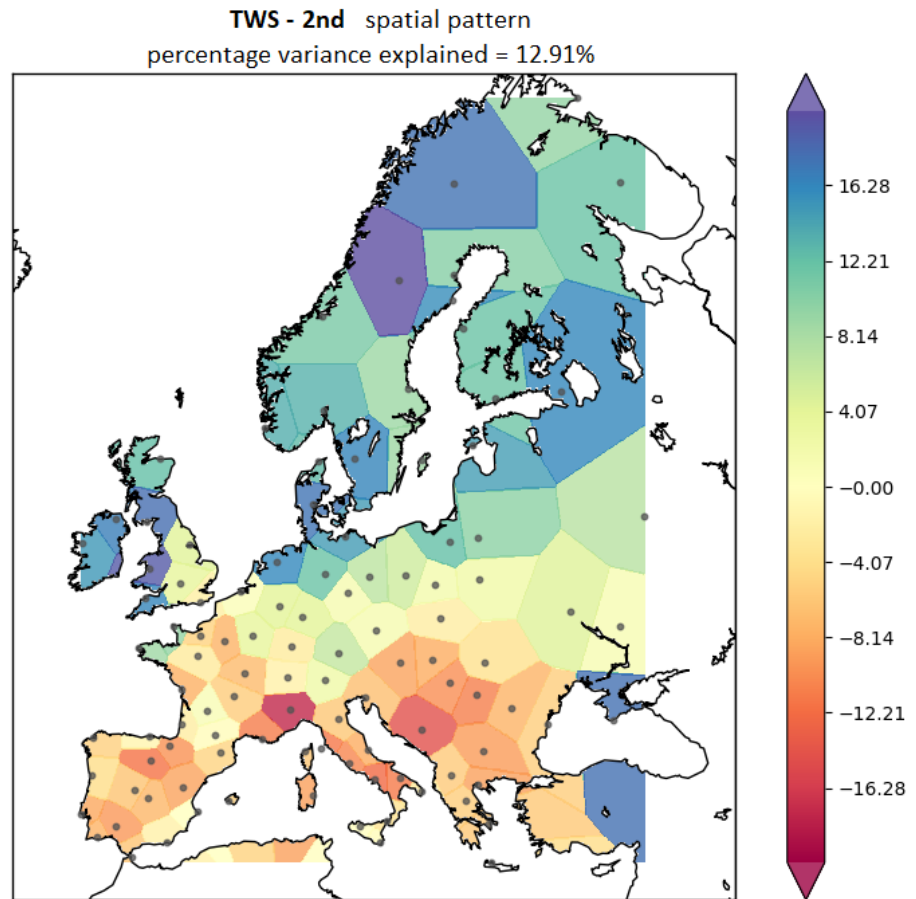


Figure 3.33: Second spatial pattern of the weekly TWS residuals.

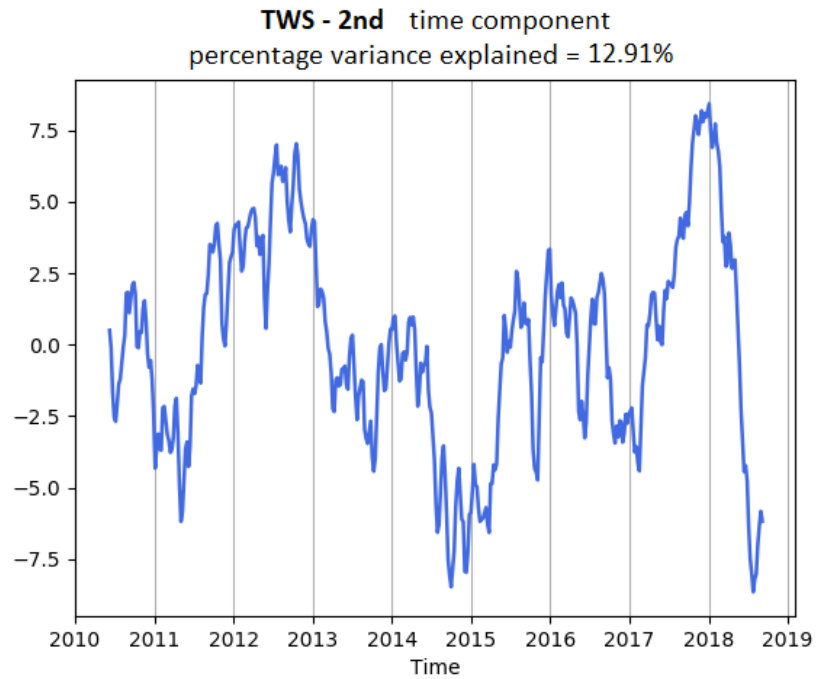


Figure 3.34: Second time component of the weekly TWS residuals.

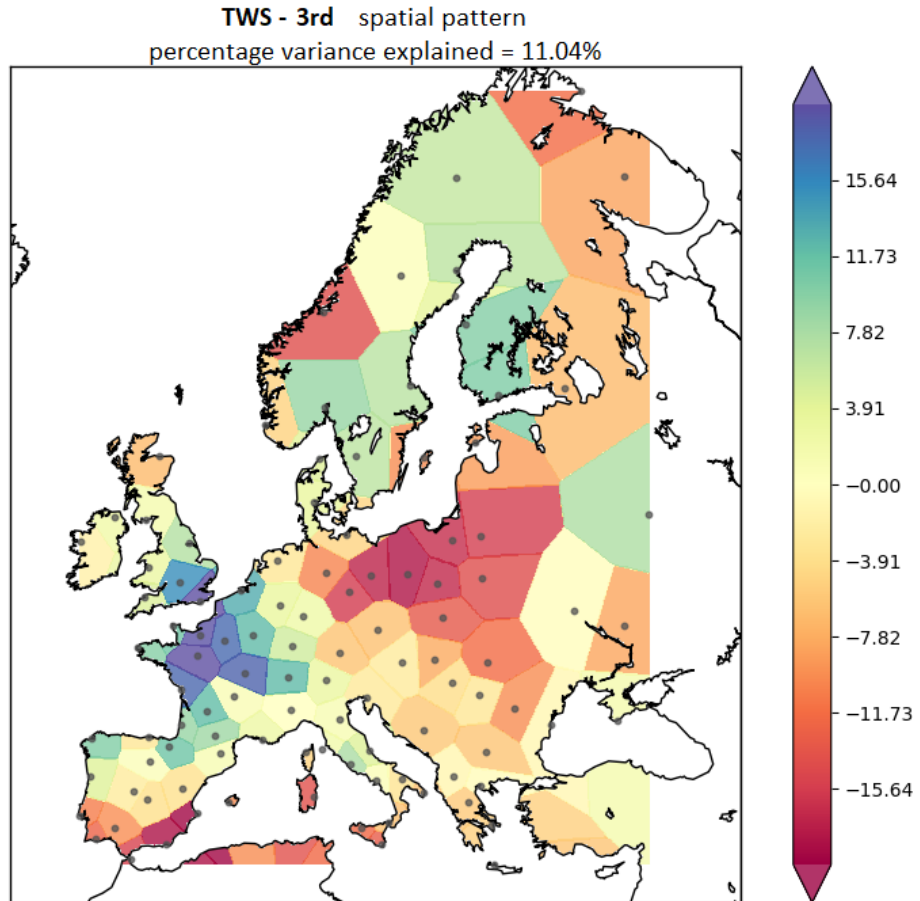


Figure 3.35: Third spatial pattern of the weekly TWS residuals.

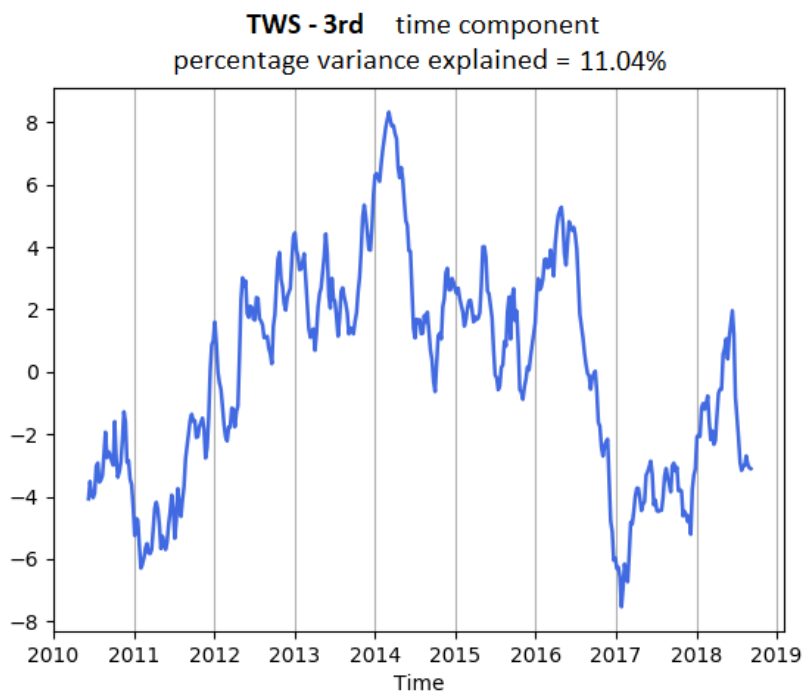


Figure 3.36: Third time component of the weekly TWS residuals.

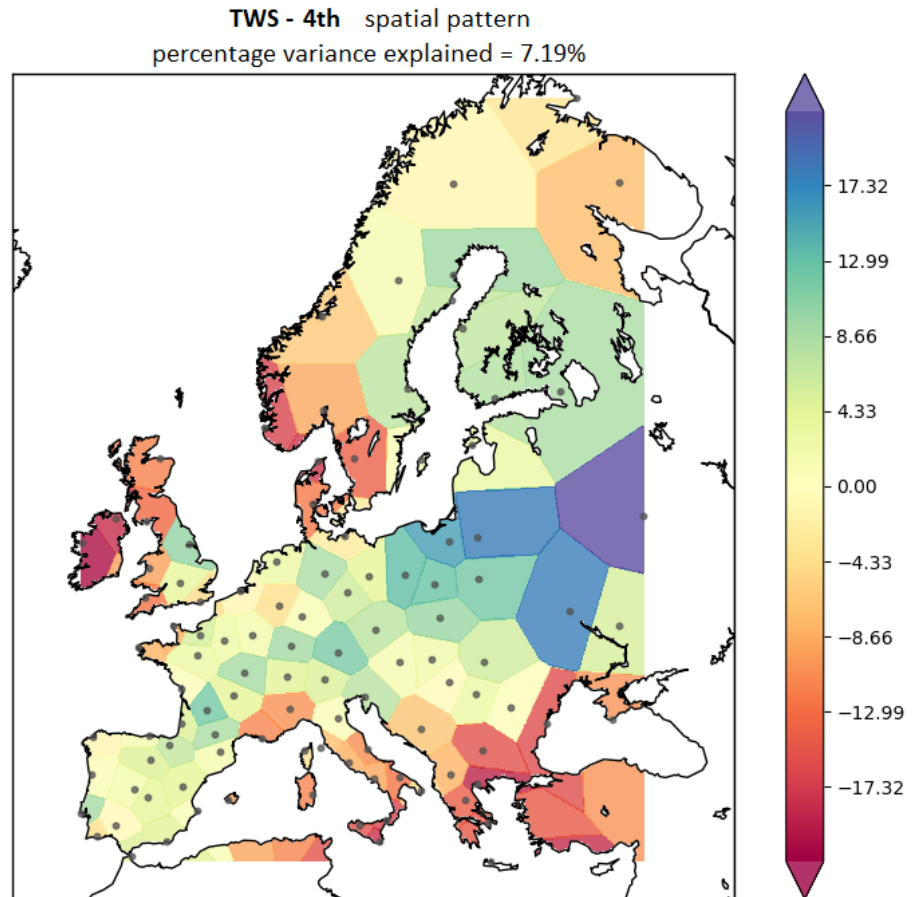


Figure 3.37: Fourth spatial pattern of the weekly TWS residuals.

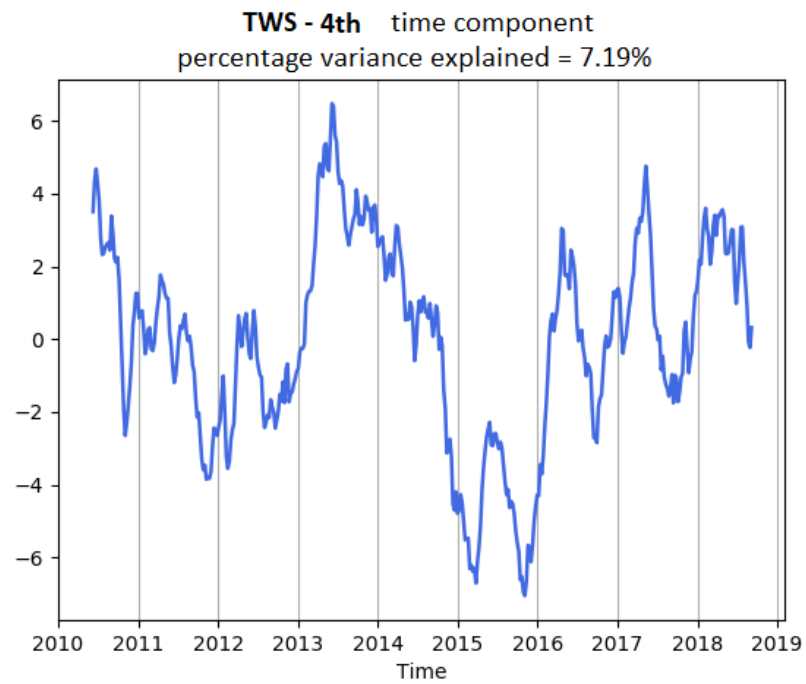


Figure 3.38: Fourth time component of the weekly TWS residuals.

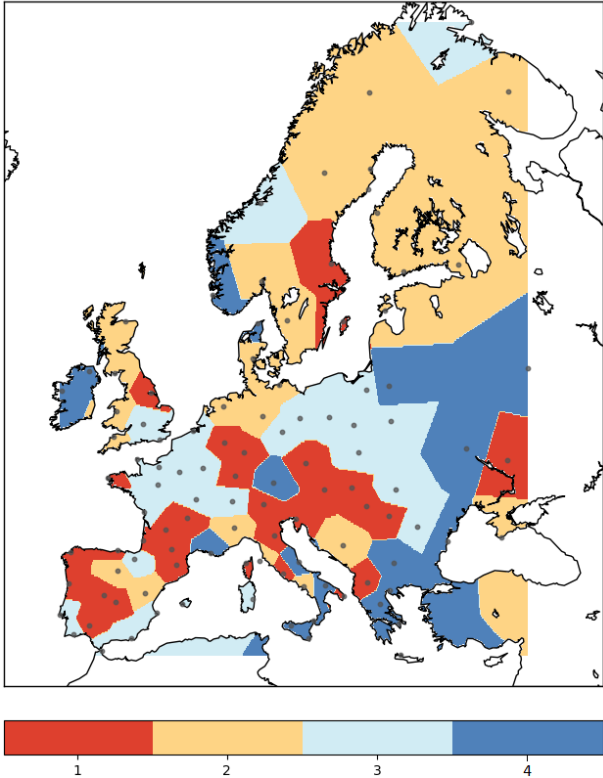


Figure 3.39: Regionalization map of the first four spatial patterns of the TWS residuals.

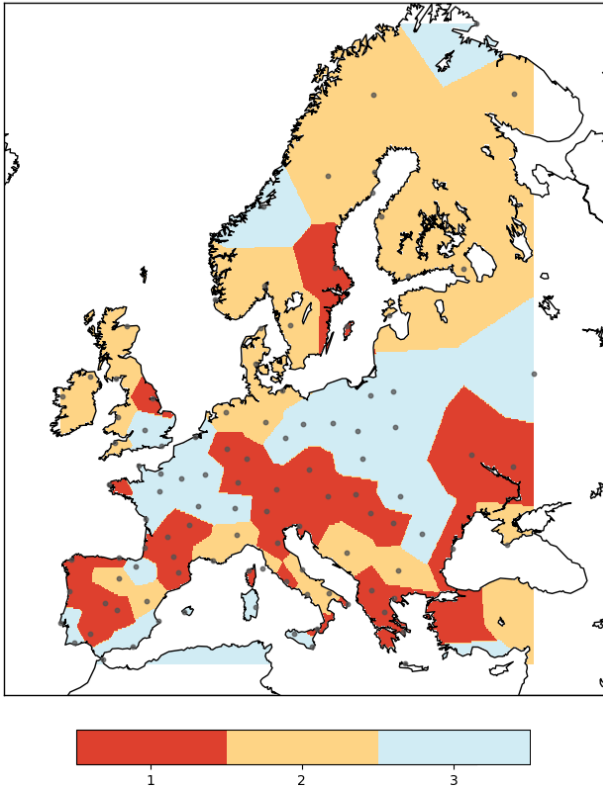


Figure 3.40: Regionalization map of the first three spatial patterns of the TWS residuals.

## 3.2 SVD

The SVD analysis allows identifying significant correlation between pair of variables (Section 1.2.3). In fact, the SVD analysis performed on two data fields identifies only those modes representing coupled variability. In this section, inter-annual variations observed in the residual series of the GPS Up coordinate of 107 stations (Figure 2.2, p. 17) located in the Mediterranean and European area are compared, by means of the SVD approach, with those present in the residual time series of the SP and TWS. Lastly, the results of the SVD study are discussed.

The result of the SVD analysis are coupled modes of variability. Each of these consists of two spatial patterns (one for each variable) and two time components. The maps of the SVD spatial pattern coefficients were obtained by assigning the corresponding value to the station point on the map and then filling the map through a nearest neighbors interpolation. The spatial pattern coefficients were multiplied by a factor 100, since they are always lower than 1. The plot color bar was created in such a way that the zero value is always in the middle of the bar. The time components of the corresponding SVD are also presented and show a similar time variability, as expected.

### 3.2.1 GPS Up coordinates and SP

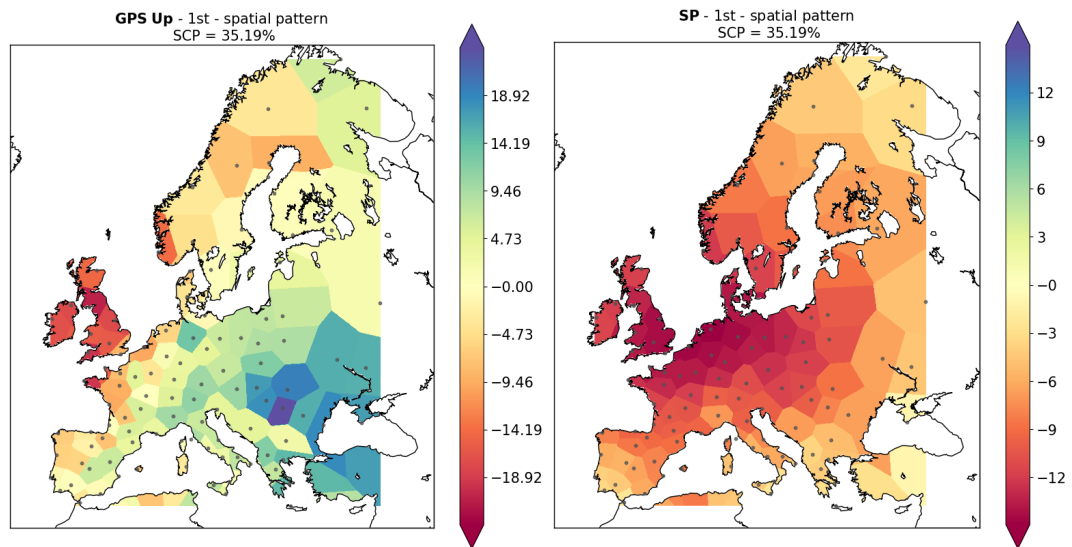
The first three leading SVD modes of the coupled SP and GPS Up coordinates variations account for 70.11% of the total covariance.

The first coupled mode of variability explains 35.19% of the total covariance. The first SVD spatial pattern of the GPS Up time series (Figure 3.41a) shows a gradient from North-West to South-East; the highest negative values characterize the British Isles, while positive values are found over Southeastern Europe. The first SVD spatial pattern of the SP (Figure 3.41b) is coherent and negative all over Europe. These patterns mean that, over the British Isles and Northern Europe, the SP and the GPS Up exhibit a similar behaviour while, in Southeastern Europe, they show an opposite one. The first SVD time components (Figure 3.41c) does not show any long-period oscillation. Short period oscillations are present, however without an easily recognizable period. As regards SP, a few large peaks characterize the time series, which should be further investigated. Shorter period oscillations are superimposed.

The second coupled mode of variability explains 22.93% of the total covariance. The second SVD spatial pattern of the GPS Up time series (Figure 3.42a) is coherent with negative values over most of Northern Europe. Exceptions are Scandinavia and part of the British Isles. Southern Europe is mostly coherent,

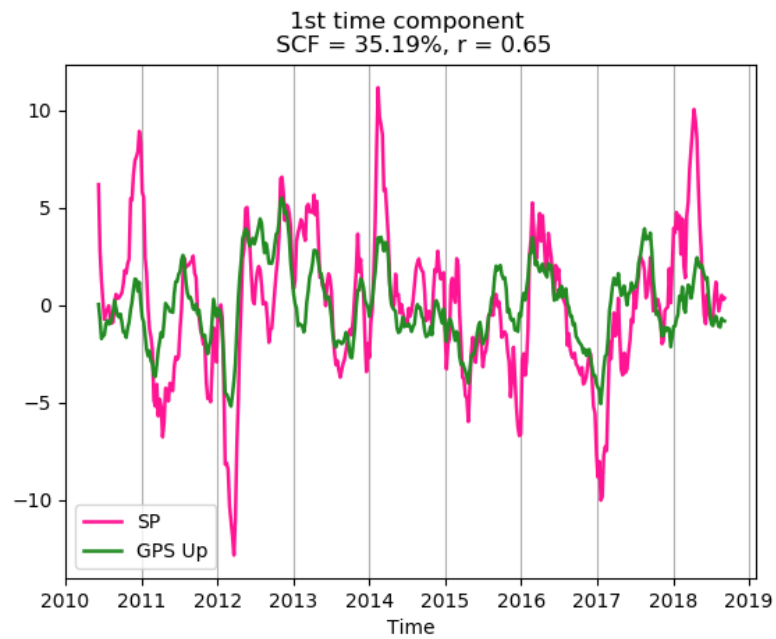
but is characterized by positive coefficients. The second SVD spatial pattern of the SP (Figure 3.42b) shows the highest positive values in the British Isles and Scandinavia passing to negative values in Central-Southern Europe and across the Mediterranean. These patterns present a general anticorrelation that suggest that this mode could be representative of the vertical crustal deformation induced by the atmospheric loading. The second SVD time components (Figure 3.42c) show a long period variability (of about 7 years) on which is superimposed a short-period (about 1 year) oscillation.

The third coupled mode of variability explains 11.99% of the total covariance. The third SVD spatial pattern of the GPS Up time series (Figure 3.43a) is characterized by low values all over Europe. Exceptions are found in Eastern Europe and on the coastlines of Western and Northern Europe. The third SVD spatial pattern of the SP (Figure 3.43b) shows a zonal gradient and is characterized by negative values in Western Europe and positive elsewhere. The third SVD time components (Figure 3.43c) show short period oscillations, characterized by high intrannual variability.



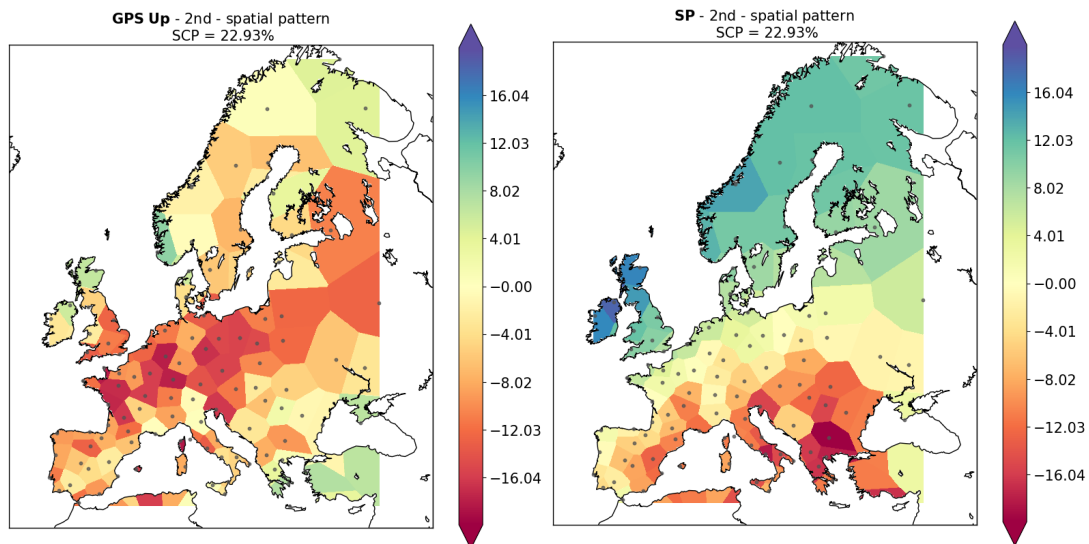
(a) First spatial pattern of the GPS Up component.

(b) First spatial pattern of the SP.



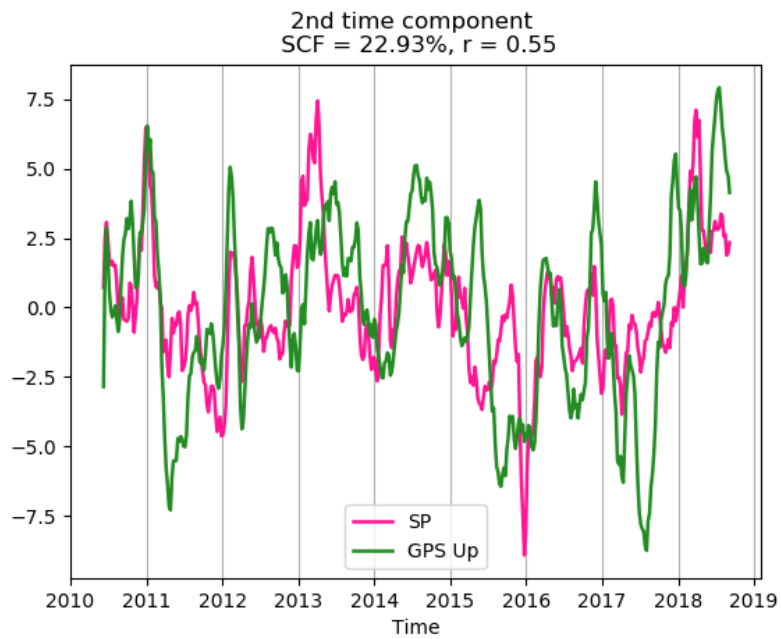
(c) First time component of SP (magenta line) and GPS Up component (green line).

Figure 3.41: First SVD of GPS Up component and SP.



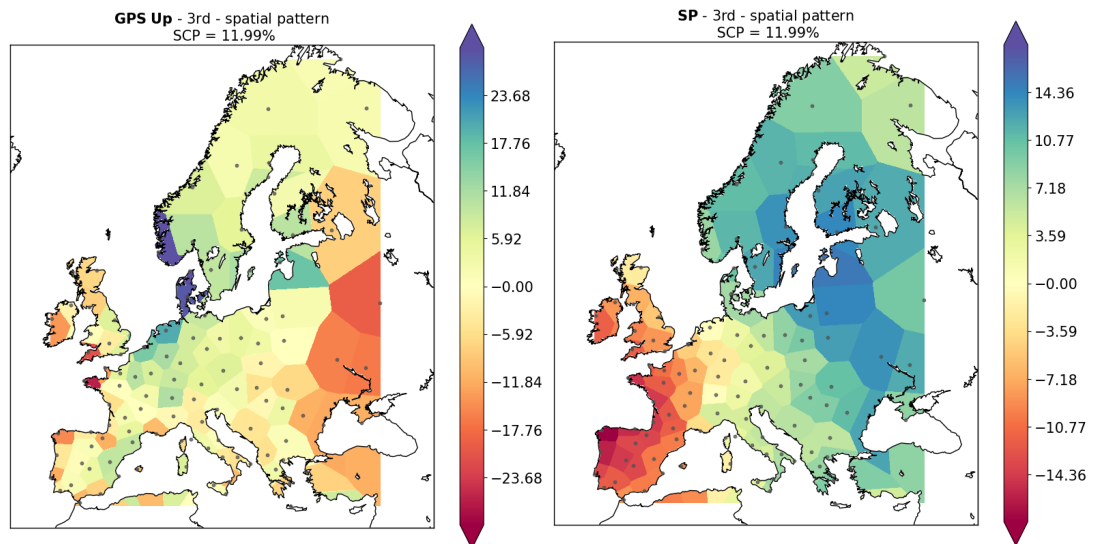
(a) Second spatial pattern of the GPS Up component.

(b) Second spatial pattern of the SP.



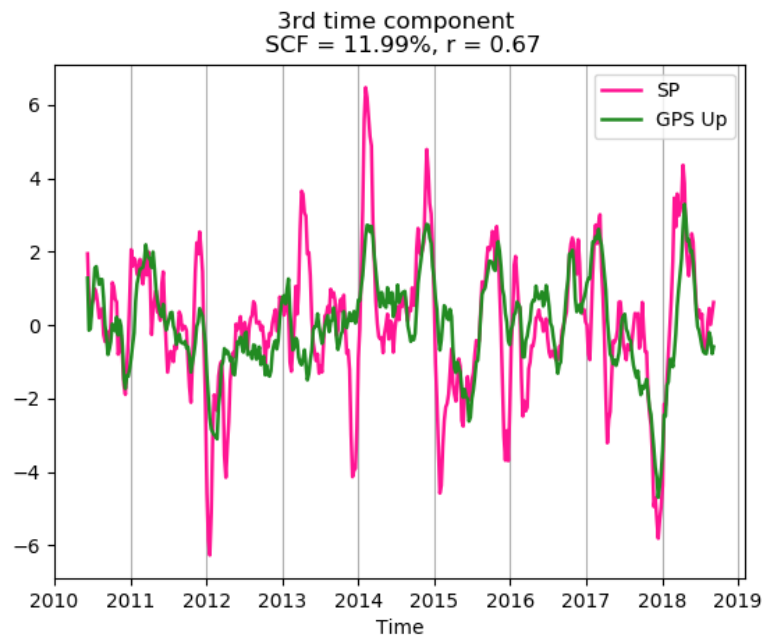
(c) Second time component of SP (magenta line) and GPS Up component (green line).

Figure 3.42: Second SVD of GPS Up component and SP.



(a) Third spatial pattern of the GPS Up component.

(b) Third spatial pattern of the SP.



(c) Third time component of SP (magenta line) and GPS Up component (green line).

Figure 3.43: Third SVD of GPS Up component and SP.

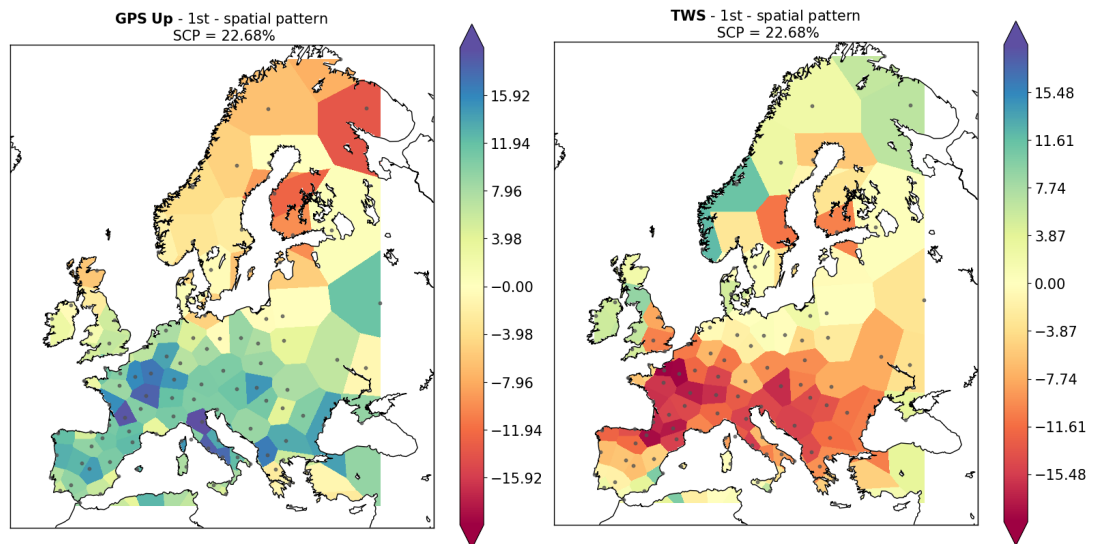
### 3.2.2 GPS Up coordinate and TWS

The three leading SVD modes of the coupled TWS and GPS Up coordinate variations account for 48.1% of the total covariance.

The first coupled mode of variability explain 22.68% of the total covariance. The first SVD spatial pattern of the GPS Up time series (Figure 3.44a) shows a gradient from North (negative values) to South Europe (positive values). The first SVD spatial pattern of the TWS (Figure 3.44b) exhibits an opposite behaviour. These patterns mean that, if the TWS has a negative variation over a certain area, the GPS Up has a positive variation in the same area. The observed anticorrelation suggests this mode could be representative of the vertical deformation due to loading of the TWS on the Earth's crust. The first SVD time components (Figure 3.44c) show a long-period variability (6-to-7 years) on which are superimposed short-period oscillations.

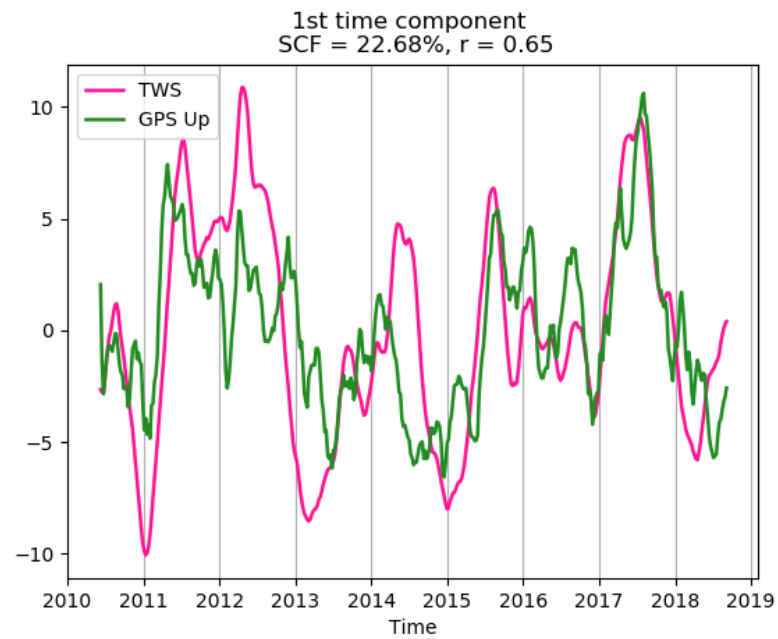
The second coupled mode of variability explains 13.81% of total covariance. The second SVD spatial pattern of the GPS Up time series (Figure 3.45a) is characterized by negative values in Western Europe and the Mediterranean and positive values elsewhere. The second SVD spatial pattern of the TWS (Figure 3.45b) exhibit the same behaviour in the western part of Europe (Iberian Peninsula, Italy, British Isles and France) and an opposite behaviour over the eastern part. The second SVD time components (Figure 3.45c) is characterized by a long-term oscillation, with increasing values till about 2015 followed by a decrease.

The third coupled mode of variability explain 11.61% of the total covariance. The third SVD spatial pattern of the GPS Up time series (Figure 3.46a) is characterized by negative values all over Europe, except in the Balkan region. The third SVD spatial pattern of the TWS (Figure 3.46b) shows an opposite pattern, except in the Mediterranean. The third SVD time components (Figure 3.46c) is characterized by a long-period oscillation, on which are superimposed higher frequency oscillations.



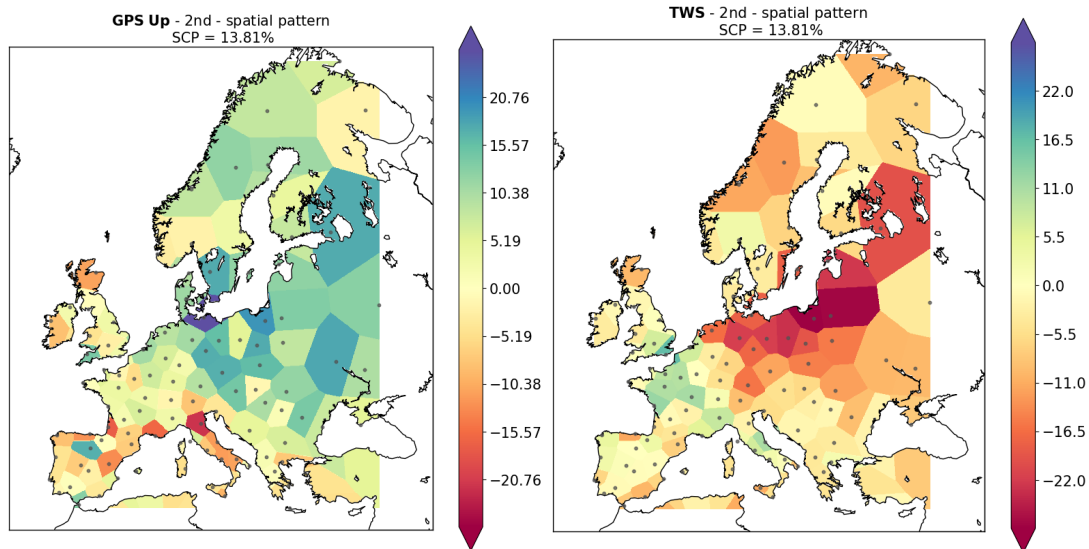
(a) First spatial pattern of the GPS Up component.

(b) First spatial pattern of the TWS.



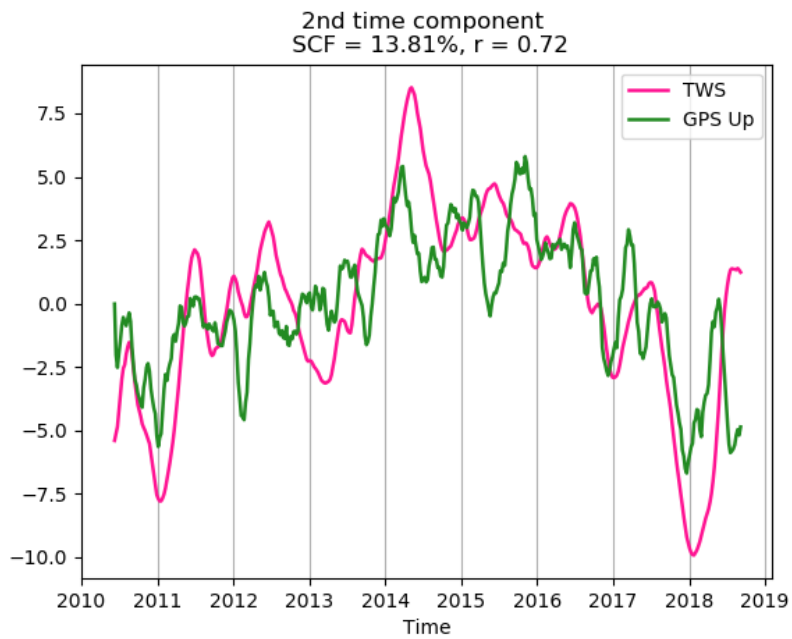
(c) TWS (magenta line) and GPS Up component (green line) first expansion coefficients.

Figure 3.44: First SVD of GPS Up component and TWS.



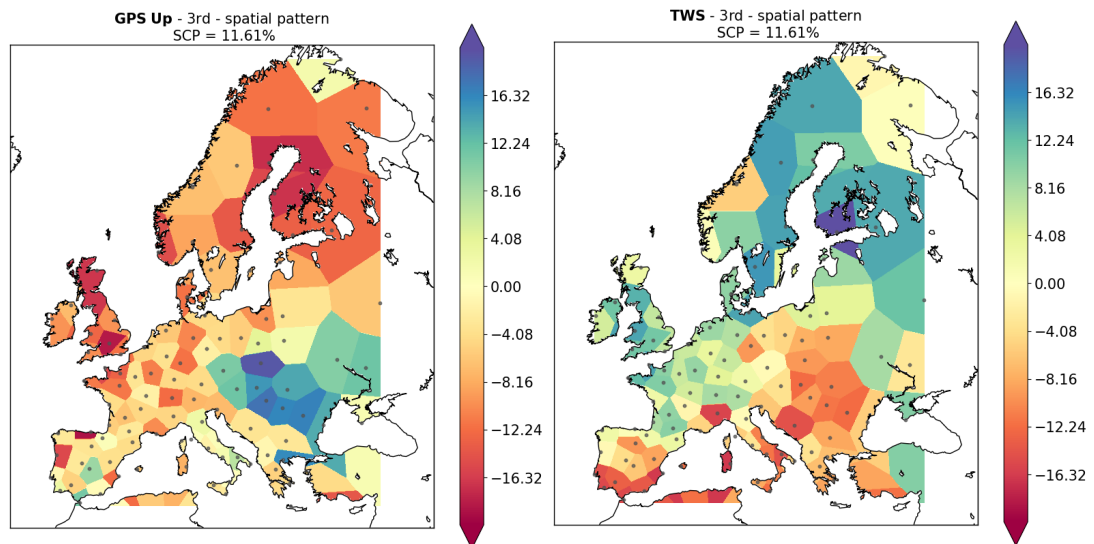
(a) Second spatial pattern of the GPS Up component.

(b) Second spatial pattern of the TWS.



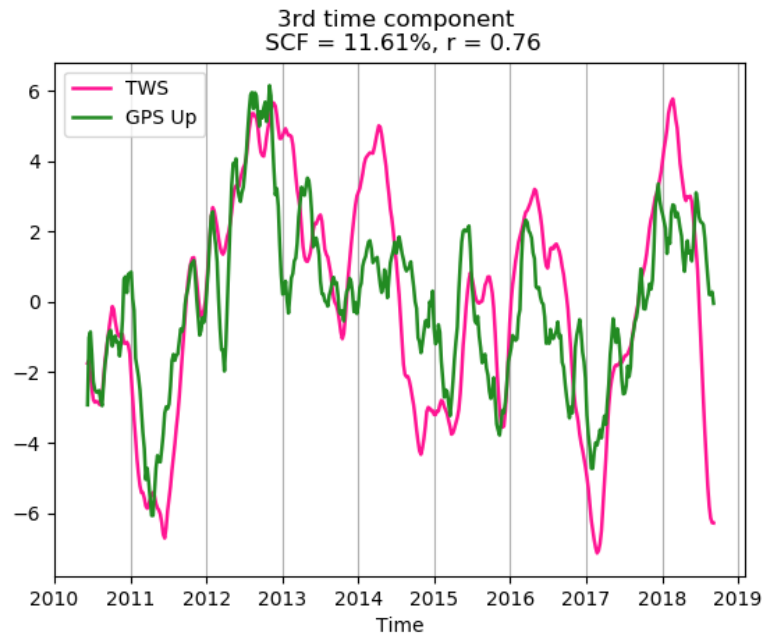
(c) TWS (magenta line) and GPS Up component (green line) second expansion coefficients.

Figure 3.45: Second SVD of GPS Up component and TWS.



(a) Third spatial pattern of the GPS Up component.

(b) Third spatial pattern of the TWS.



(c) TWS (magenta line) and GPS Up component (green line) third expansion coefficients.

Figure 3.46: Third SVD of GPS Up component and TWS.

# GPS Up and climate indices

---

4.1	Northern Hemisphere Indices . . . . .	72
4.1.1	North Atlantic Oscillation (NAO) . . . . .	73
4.1.2	East Atlantic (EA) . . . . .	77
4.1.3	Scandinavia (SCAND) . . . . .	81
4.2	Arctic Oscillation (AO) . . . . .	85
4.3	Tropical North Atlantic (TNA) . . . . .	89
4.4	Multivariate ENSO Index Version 2 (MEI v2) . . . . .	92

---

In this chapter, the main climate indices will be introduced and the correlation with stations GPS Up time series will be studied. In order to reduce potential effect of local anomalies, the GPS Up residuals were represented using the first four modes of variability<sup>1</sup> previously identified<sup>2</sup> (Section 3.1.1). Since climate indices are provided as series of monthly values, monthly Up residuals were also estimated.

In order to investigate possible correlation between climate indices and the GPS Up residuals, correlation maps were created. For each climate index, the map was produced as follows:

- the percentage of correlation between the climate index and the GPS Up time series of each location (Figure 2.2, p. 17) was estimated;
- the values obtained were assigned to each location;
- a nearest neighbour interpolation was performed.

The climate indices studied in this work are the following:

- East Atlantic (EA) teleconnection pattern;
- North Atlantic Oscillation (NAO);

---

<sup>1</sup>This procedure is called dimensionality-reduction (Section 1.2.1).

<sup>2</sup>This procedure is called dimensional reduction reference background

- Scandinavia (SCAND) teleconnection pattern;
- Arctic Oscillation (AO);
- Tropical North Atlantic (TNA);
- Multivariate ENSO Index (MEI).

A study of the relevant literature shows that the methodologies adopted to calculate these climate indices are different, but they are all based on a Principal Component Analysis (PCA).

## 4.1 Northern Hemisphere Indices

Northern Hemisphere indices are an ensemble of climate indices that arise from the same type of analysis. Northern Hemisphere teleconnection indices are calculated using the Rotated Principal Component Analysis<sup>3</sup> (RPCA; Barnston and Livezey, 1987). This procedure isolates the main teleconnection patterns for all months and allows the construction of the time series of these patterns (i.e., the climate indices).

Northern Hemisphere teleconnection patterns and the related indices are calculated by applying the RPCA to monthly mean standardized 500-mb pressure height anomalies obtained from the CDAS<sup>4</sup> in the region between 20°N and 90°N. The anomalies are standardized by the 1950-2000 base period monthly means and standard deviations. The results of this analysis are sets of ten rotated modes (one set for each month), which are the dominant teleconnection patterns, that account for most of the spatial variance of the observed standardized anomaly map in the month. These patterns are referred to as the North Atlantic Oscillation (NAO), the Pacific/North American (PNA) teleconnection pattern, the East (EA) Atlantic pattern, the West Pacific (WP) pattern, the East Pacific–North Pacific (EP–NP) pattern, the East Atlantic/Western Russia (EA/WR) pattern, the Tropical/Northern Hemisphere (TNH) pattern, the Polar-Eurasian pattern, the Scandinavia (SCAND) pattern, and the Pacific Transition (PT) pattern. The relevant time series are known as climate indices.

---

<sup>3</sup>The Rotated Principal Component Analysis (RPCA) consists in scaling the eigenvectors (i.e., the spatial patterns) of the data correlation matrix according to the amount of total variance they explain in the PCA, and then linearly transforming (i.e. rotating) the scaled eigenvalues under certain constraints to obtain the main circulation patterns. In order to derive the Northern Hemisphere teleconnection indices, the RPCA method adopted is the varimax, which preserves the orthogonality of the eigenvectors.

<sup>4</sup>Climate Data Assimilation System.

In this work, it was decided to investigate only those indices, among the ones mentioned above, which have a recognized pattern over Europe and the North Atlantic and that may influence the European and Mediterranean weather and climate. The objective is to investigate if significant correlations exist between the indices and the GPS Up time series of the stations in the network.

#### 4.1.1 North Atlantic Oscillation (NAO)

The North Atlantic Oscillation (NAO) is one the most prominent teleconnection pattern in all seasons (Barnston and Livezey, 1987) and is the leading rotated spatial pattern identified by the RPCA procedure. The NAO consists of a north-south dipole of anomalies, with one center located over Greenland and the other center of opposite sign spanning the central latitudes of the North Atlantic, between 35°N and 40°N (Figure 4.1).

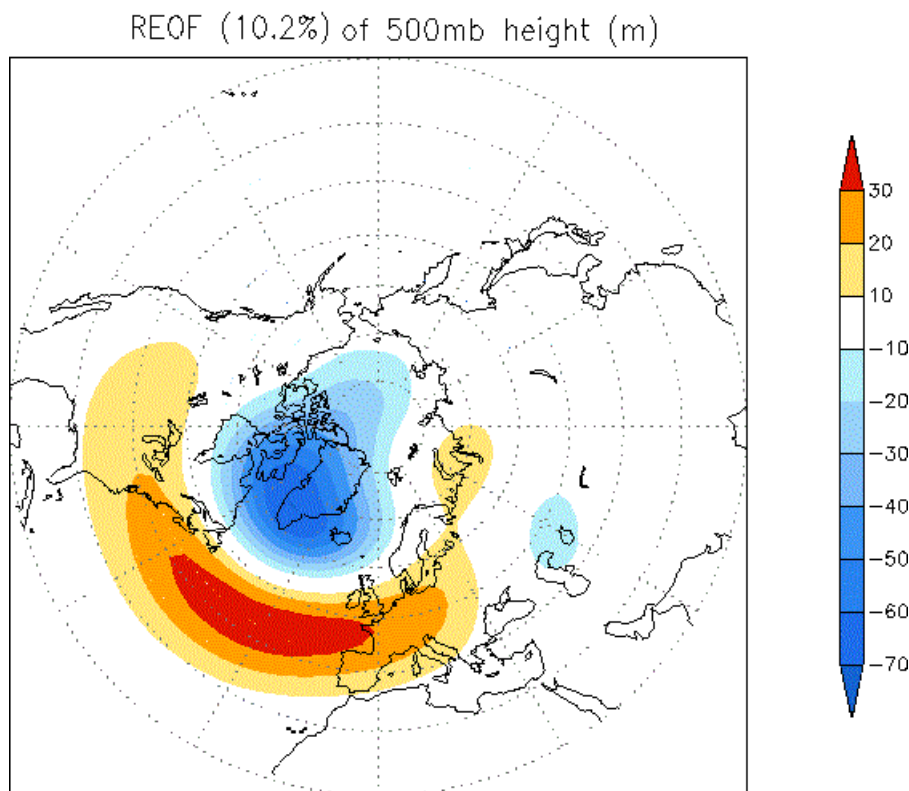


Figure 4.1: Spatial pattern of the NAO from January 1950 to January 2000 (NOAA CPC, 2000).

The NAO index time series is characterized by intrannual and interannual variability and exhibits positive and negative phases, which occasionally persists over periods of several months (Figure 4.2).

Strong positive phases of the NAO tend to be associated with above-average temperature across Northern Europe and, in winter, with above-average precipita-

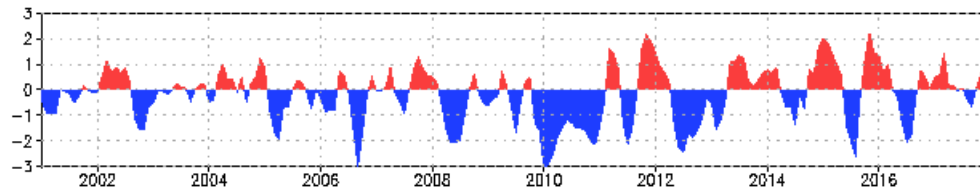


Figure 4.2: The NAO standardized 3-month running mean index (NOAA CPC, 2020e).

tion over Northern Europe and Scandinavia and below-average precipitation over Central and Southern Europe. Opposite patterns of temperature and precipitation anomalies are typically observed during strong negative phases of the NAO.

The principal time components of the GPS Up time series does not show any significant correlation with the NAO index. The second (Figure 4.3) and third (Figure 4.4) time components show a positive correlation with the NAO index on the order of 20%, but with a significance level less than 95% (i.e., a p-value higher than 0.05).

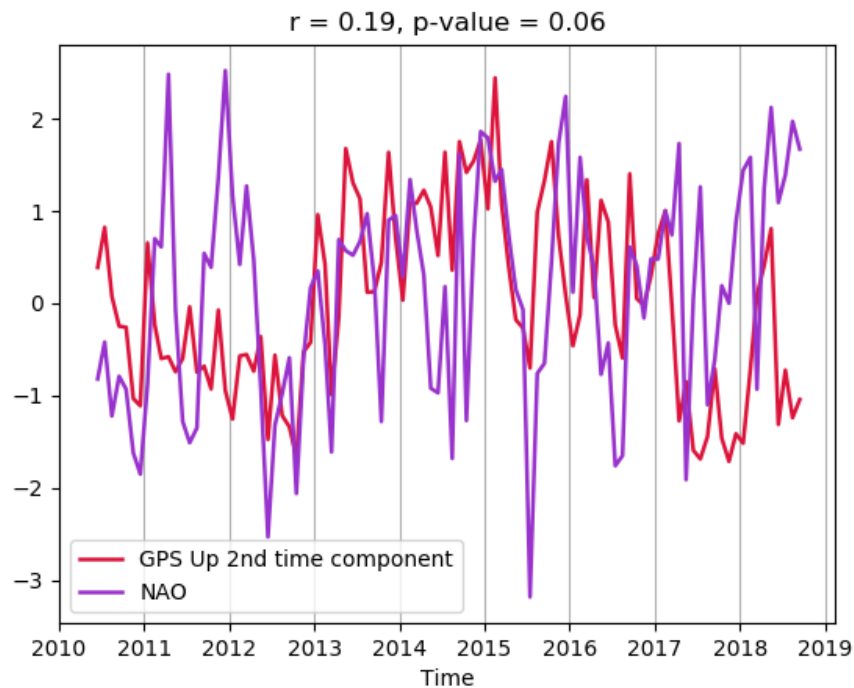


Figure 4.3: Comparison between the GPS Up second time component and the NAO index.

The correlation map between the GPS Up time series, represented through the four main modes of variability, and the NAO index (Figure 4.5) shows a gradient going from Northern to Southern Europe. In particular, positive correlation coefficients characterize Scandinavia and the British Isles, while negative correlation coefficients are found in Southeastern Europe and the Mediterranean region. Among the 107 stations, only 12 GPS Up time series show a correlation with the NAO

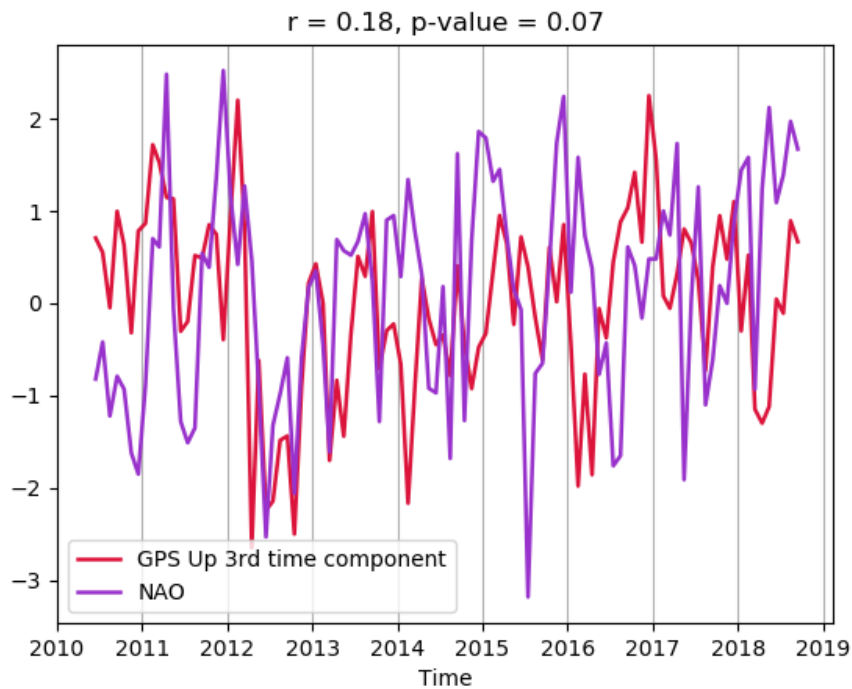


Figure 4.4: Comparison between the GPS Up third time component and the NAO index.

index higher than 10% and a significance level above 95% (Table 4.1). The relative GPS sites are identified with lilac dots in the map.

	N. GPS Up time series
$ r  \geq 10\%$	58
significance level $\leq 95\%$	46
$ r  \geq 10\%$ & significance level $> 95\%$	12
$ r  \geq 10\%$ & significance level $> 99\%$	0

Table 4.1: Number of GPS sites for each of the following conditions: correlation coefficient ( $r$ ) in absolute value higher or equal to 10%; significance level lower or equal to 95%; correlation coefficient ( $r$ ) in absolute value higher or equal to 10% and significance level larger than 95%; correlation coefficient ( $r$ ) in absolute value higher or equal to 10% and significance level larger than 99%.

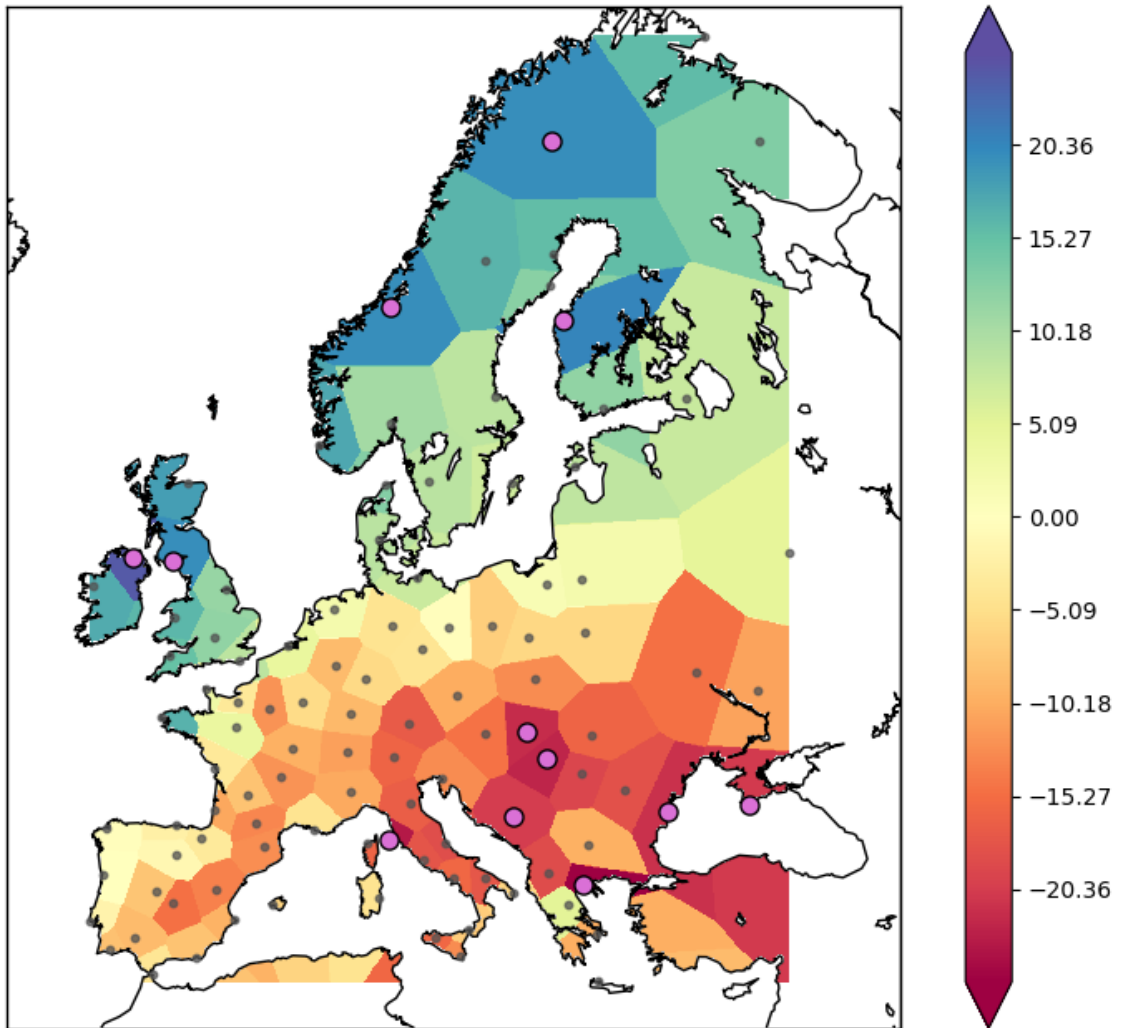


Figure 4.5: Correlation map between GPS Up time series and the NAO index. Lilac points identify the GPS sites whose time series has a significant correlation larger than 10%.

### 4.1.2 East Atlantic (EA)

The East Atlantic (EA) pattern is the second prominent mode of variability over the North Atlantic and appears as a leading mode in all months. The EA pattern consists of a north-south dipole of anomaly centers, spanning the North Atlantic from west to east (Figure 4.6). These anomaly centers are displaced southeastward with respect to the NAO pattern.

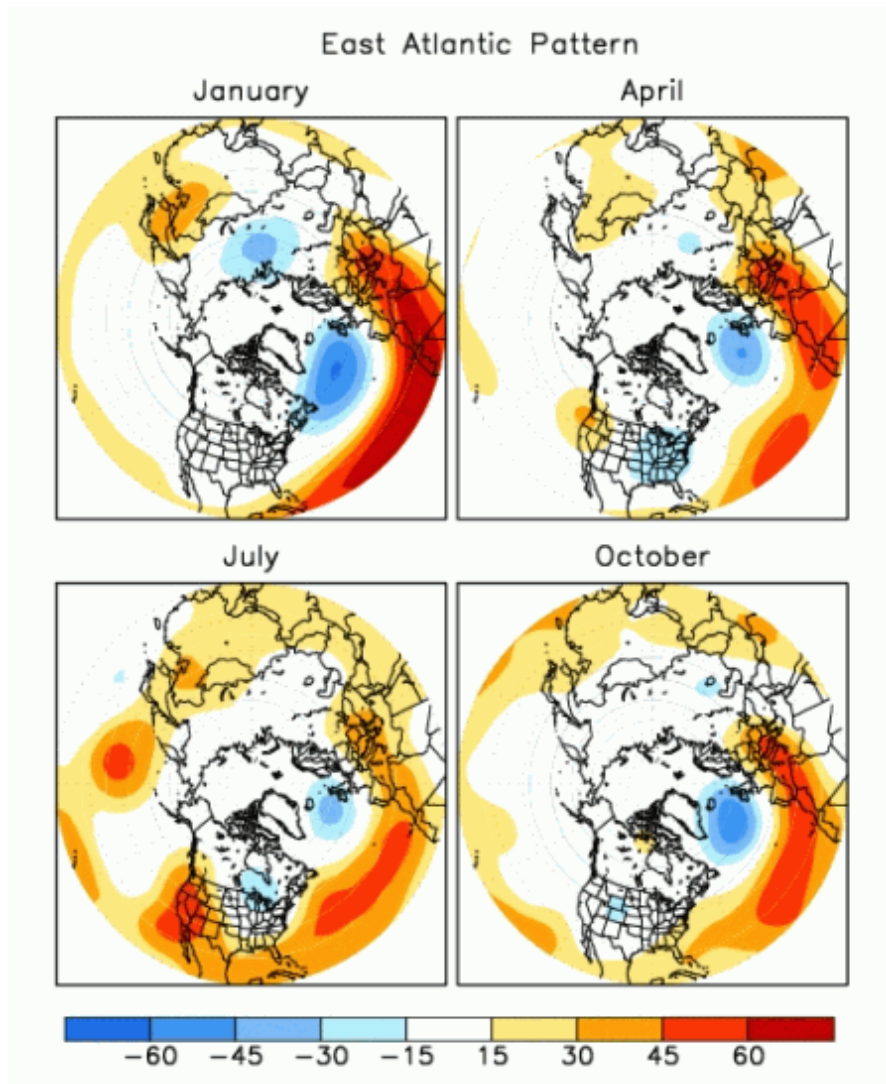


Figure 4.6: The EA positive phase spatial pattern during January, April, July and October (NOAA CPC, 2020b).

The EA pattern exhibits positive and negative phases; however, during the last 20 years, the EA index shows a positive phase that is strong and persistent (Figure 4.7). The positive phase of the EA pattern is associated with above-average surface temperatures in Europe in all months, with above-average precipitation over Northern Europe and Scandinavia and below-average precipitation across Southern Europe.

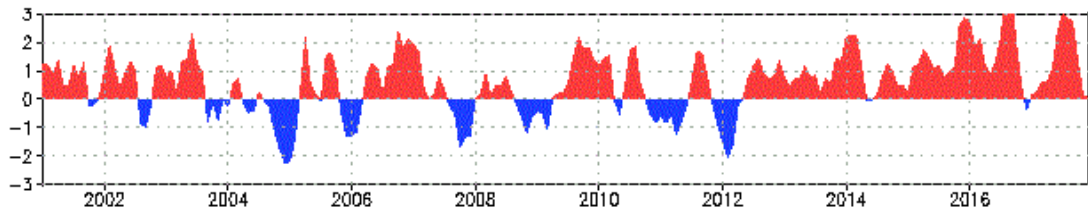


Figure 4.7: The EA standardized 3-month running mean index (NOAA CPC, 2020c).

The EA index shows a significant anticorrelation, about -30% with a significance level equal or larger than 99%, with the first and the fourth time components of the GPS Up time series (Figures 4.8 and 4.9). In both cases, the spatial pattern coefficients are negative in Central Europe (Figures 3.1 and 3.7).

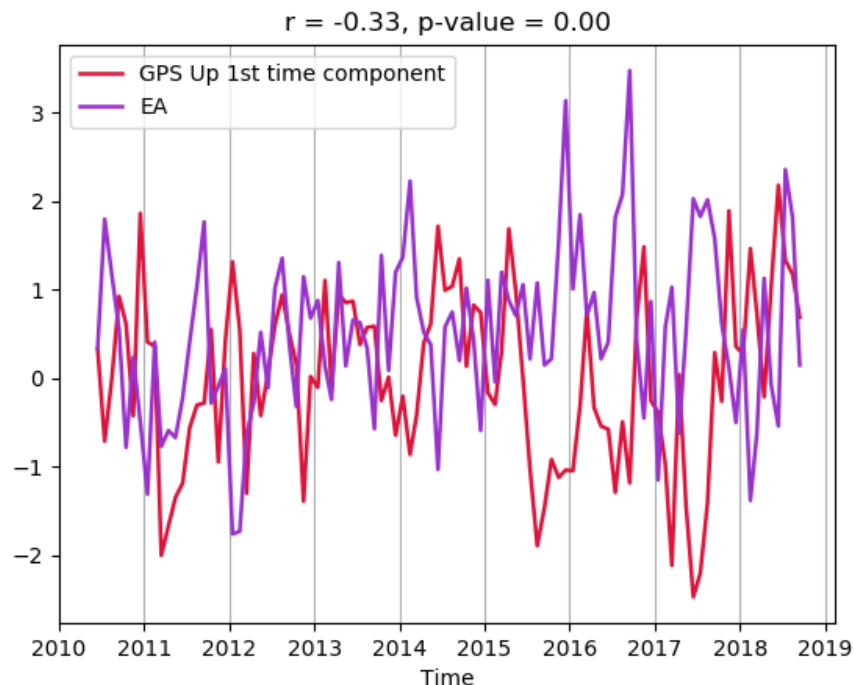


Figure 4.8: Comparison between the GPS Up first time component and the EA index.

The correlation map between the EA index and the GPS Up time series, described through the first four time components, shows a pattern coherent in Central and Southern Europe and over the Mediterranean. Among the 107 time series, 63 have a significant positive correlation with the EA index (significance level higher than 95%), of which 41 with a significance level higher than 99% (Table 4.2).

In Section 3.2.2, it was described that the first SVD mode of variability shows anticorrelation between the GPS Up coordinate and the TWS. Considering that the positive phase of the EA is associated to below-average precipitation across Southern Europe and, likely, to below-average TWS in the same area, the correlation found

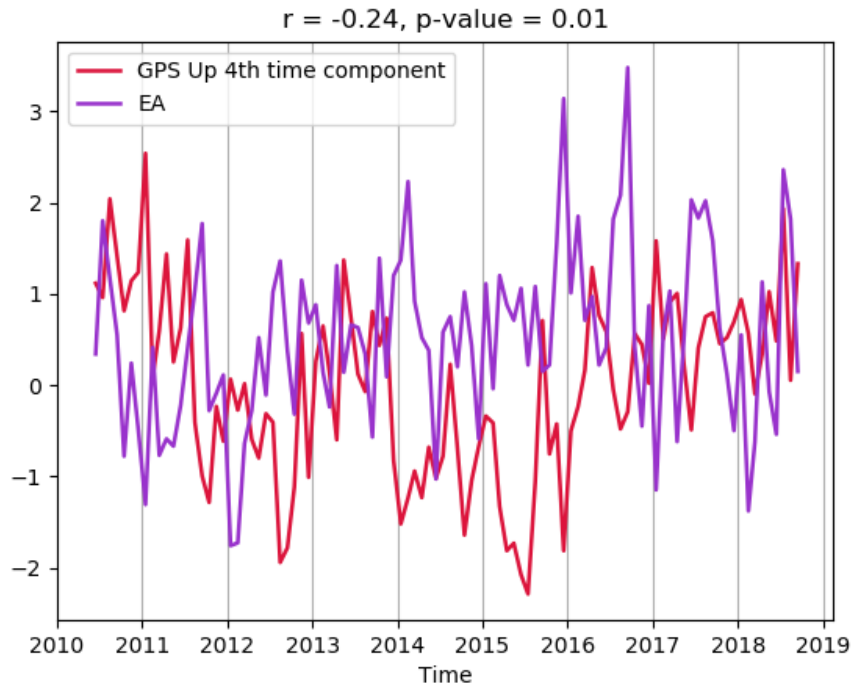


Figure 4.9: Comparison between the GPS Up fourth time component and the EA index.

	N. GPS Up time series
$ r  \geq 10\%$	90
significance level $\leq 95\%$	27
$ r  \geq 10\%$ & significance level $> 95\%$	63
$ r  \geq 10\%$ & significance level $> 99\%$	41

Table 4.2: Number of GPS sites for each of the following conditions: correlation coefficient ( $r$ ) in absolute value higher or equal to 10%; significance level lower or equal to 95%; correlation coefficient ( $r$ ) in absolute value higher or equal to 10% and significance level larger than 95%; correlation coefficient ( $r$ ) in absolute value higher or equal to 10% and significance level larger than 99%.

between the EA index and the series of GPS Up coordinates might be representative of the loading effects on the Earth's crust.

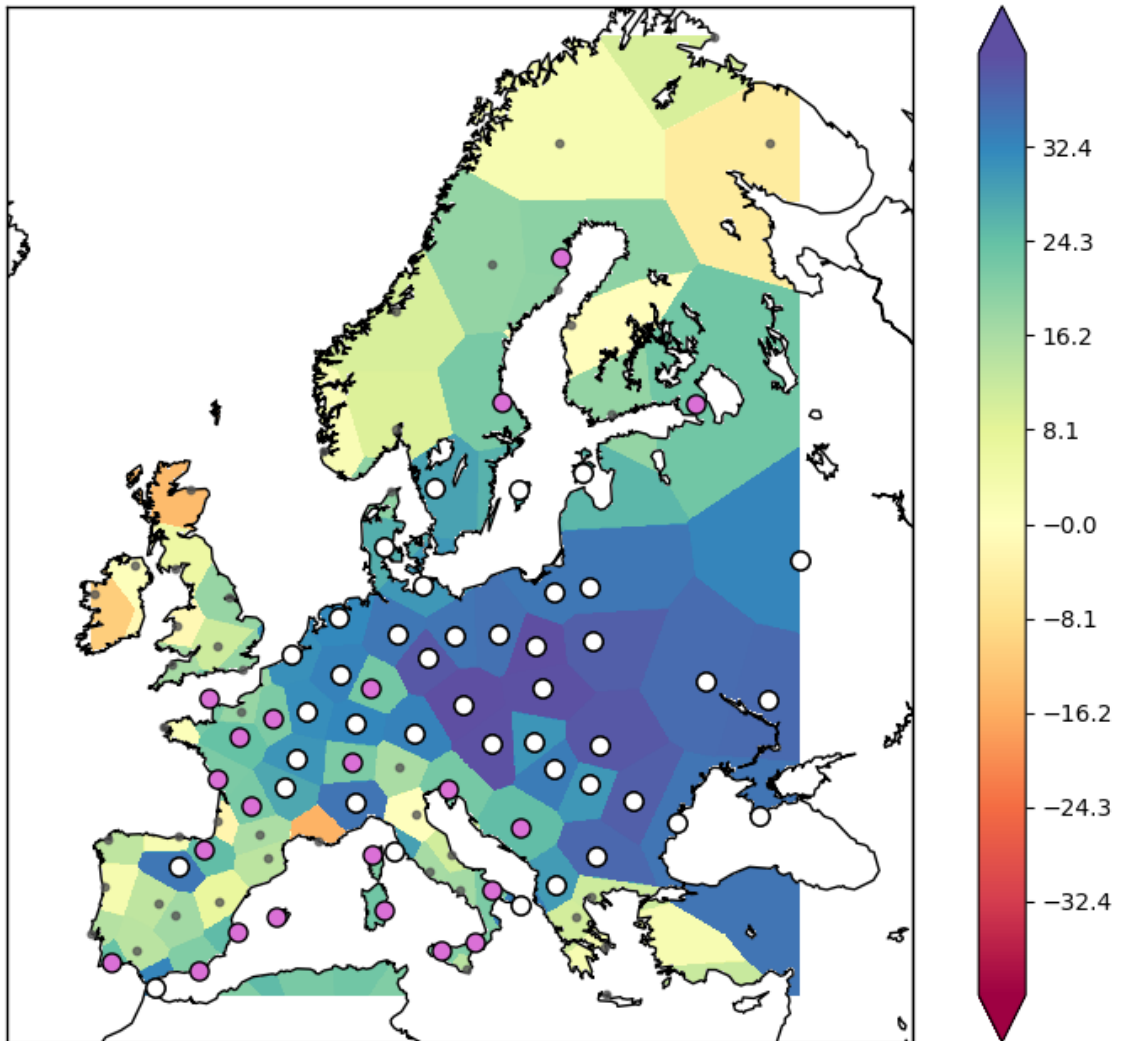


Figure 4.10: Correlation map of the GPS Up time series and the EA index. The GPS sites the Up time series of which show a correlation with the EA index larger than 10% and a significance level larger than 95% are identified by lilac points; those sites with correlation above the same threshold and a significance level larger than 99% are identified by white points.

### 4.1.3 Scandinavia (SCAND)

The Scandinavia pattern (SCAND) consists of a primary circulation center over Scandinavia and a weaker center of opposite sign over Western Europe, Eastern Russia and Western Mongolia. The SCAND consists of a succession of positive and negative phases. The positive phase (Figure 4.11) is characterized by:

- positive pressure anomalies, typically associated to major blocking anticyclones over Scandinavia and Western Russia;
- below-average temperature across central Russia and Western Europe;
- above-average precipitation across Central and Southern Europe;
- below-average precipitation over Scandinavia.

The negative phase behaves in the opposite way.

In the last twenty years, neither the positive nor the negative phase persisted over long periods (Figure 4.12).

The SCAND index shows a significant correlation (25%) with the second time component of the GPS Up time series (Figure 4.13), the spatial pattern of which describes the Scandinavian region and the Iberian and Italian Peninsula (Figure 3.3, p. 38).

Moreover, the correlation map between SCAND index and GPS Up time series (Figure 4.14) shows significant correlations over the Scandinavian region and anticorrelations over the Iberian and Italian peninsula, i.e. the regions best described by the second PCA mode of variability. In addition, in Section 3.2.2, it was found that the second PCA mode of the GPS Up time series was similar to the second coupled mode of variability between GPS Up and TWS, and the latter is associated to precipitations, which are strongly correlated with the SCAND pattern.

The number of GPS Up time series that have a significant correlation with the SCAND index is 35 (Table 4.3), and the related sites are located both in the Scandinavian and in the Iberian and Italian Peninsula.

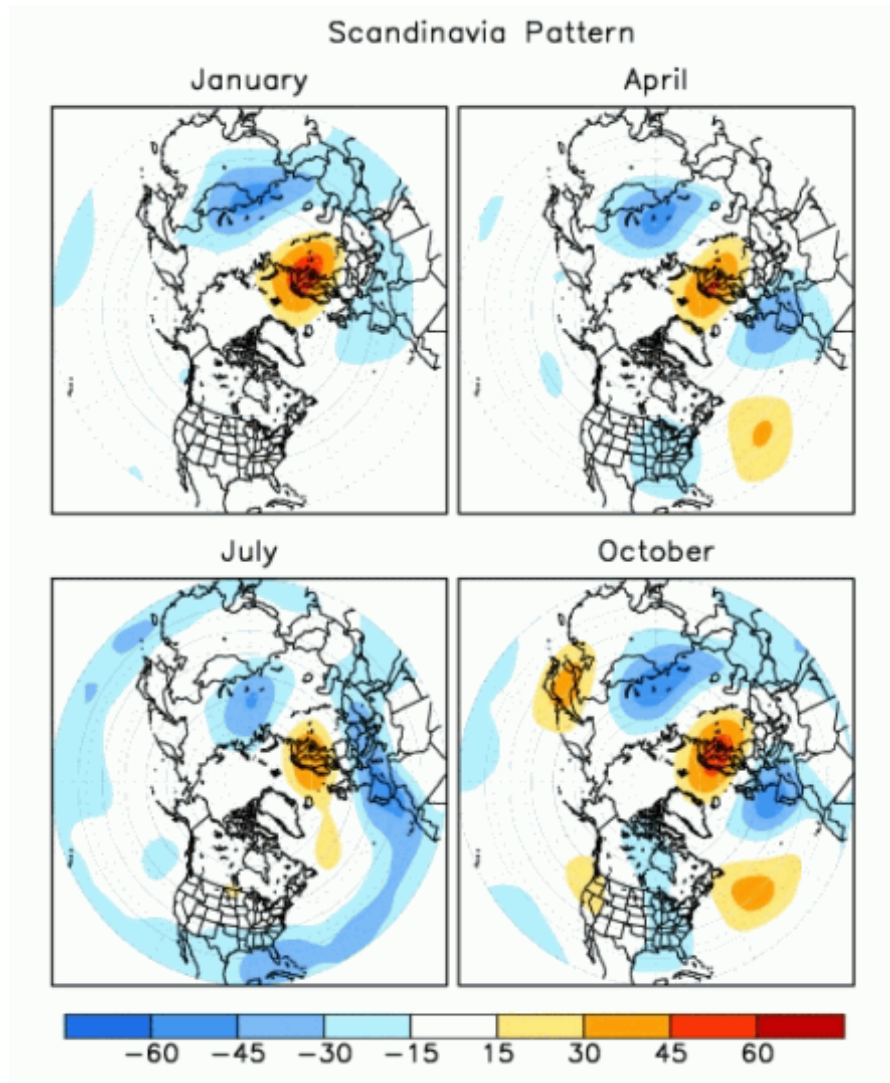


Figure 4.11: The SCAND positive phase spatial pattern during January, April, July and October (NOAA CPC, 2020f).

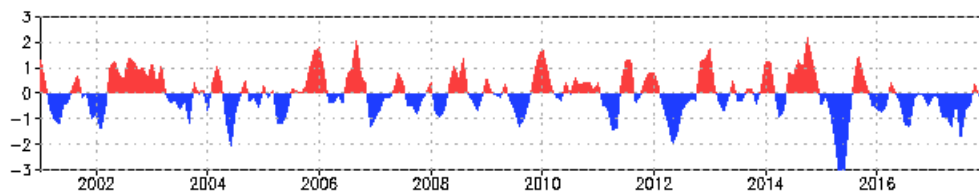


Figure 4.12: The SCAND standardized 3-month running mean index (NOAA CPC, 2020g).

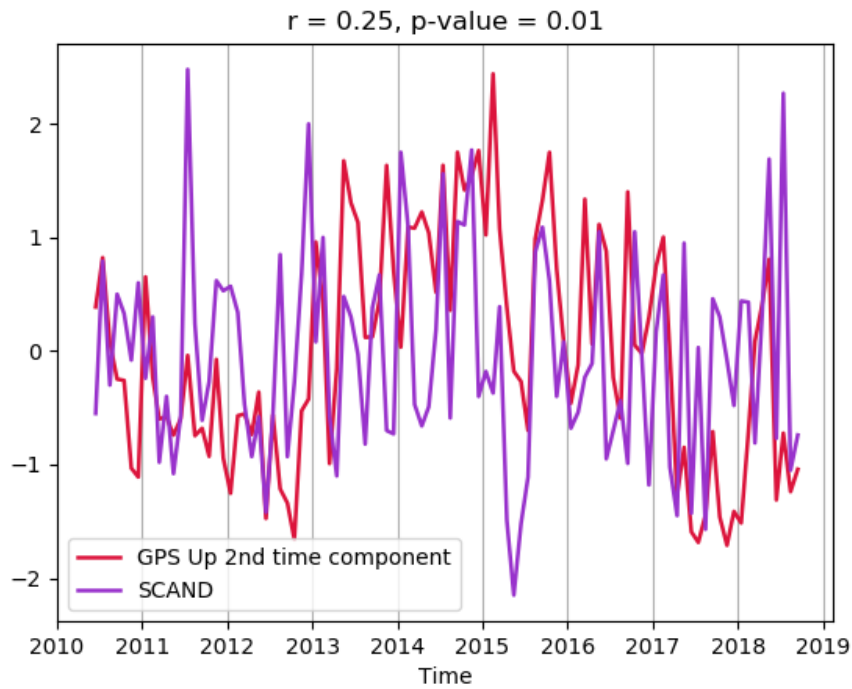


Figure 4.13: Comparison between the GPS Up second time component and the SCAND index.

	N. GPS Up time series
$ r  \geq 10\%$	79
significance level $\leq 95\%$	44
$ r  \geq 10\%$ & significance level $> 95\%$	35
$ r  \geq 10\%$ & significance level $> 99\%$	11

Table 4.3: Number of GPS sites for each of the following conditions: correlation coefficient ( $r$ ) in absolute value higher or equal to 10%; significance level lower or equal to 95%; correlation coefficient ( $r$ ) in absolute value higher or equal to 10% and significance level larger than 95%; correlation coefficient ( $r$ ) in absolute value higher or equal to 10% and significance level larger than 99%.

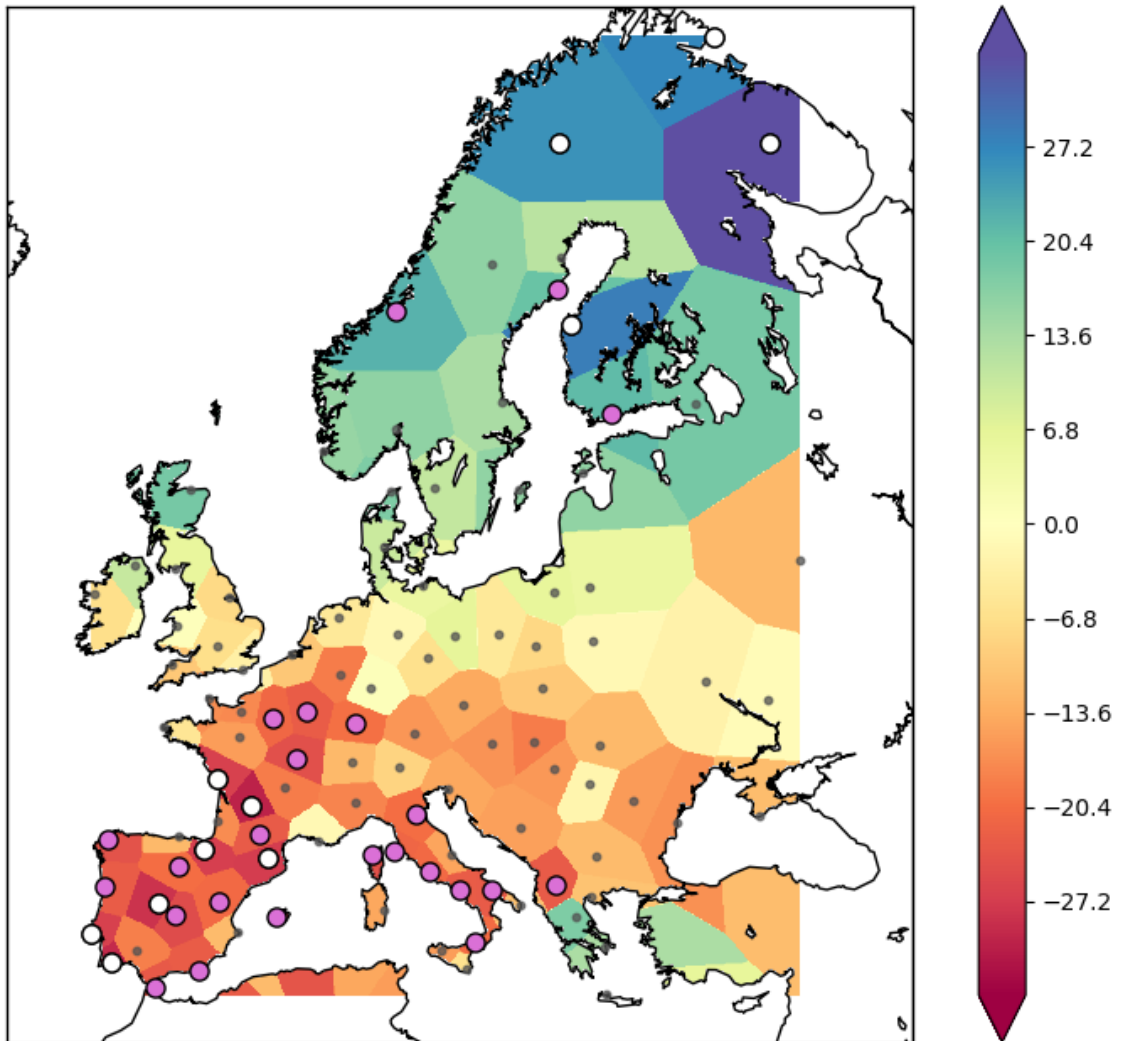


Figure 4.14: Correlation map of the GPS Up time series and the SCAND index. The GPS sites the Up time series of which show a correlation with the SCAND index larger than 10% and a significance level larger than 95% are identified by lilac points; those sites with correlation above the same threshold and a significance level larger than 99% are identified by white points.

## 4.2 Arctic Oscillation (AO)

The Arctic Oscillation (AO) pattern is a climate pattern that characterizes the northern hemisphere (Figure 4.15).

The AO is the leading mode of a PCA analysis applied to the monthly mean 1000-mb pressure height anomalies over latitudes in the range 20°N-90°N (Figure 4.15). The monthly AO index (Figure 4.16) is constructed by projecting the monthly mean 1000-mb pressure height anomalies onto the leading mode. The pressure height anomalies time series are normalized by the standard deviation of the monthly index (1979-2000 base period).

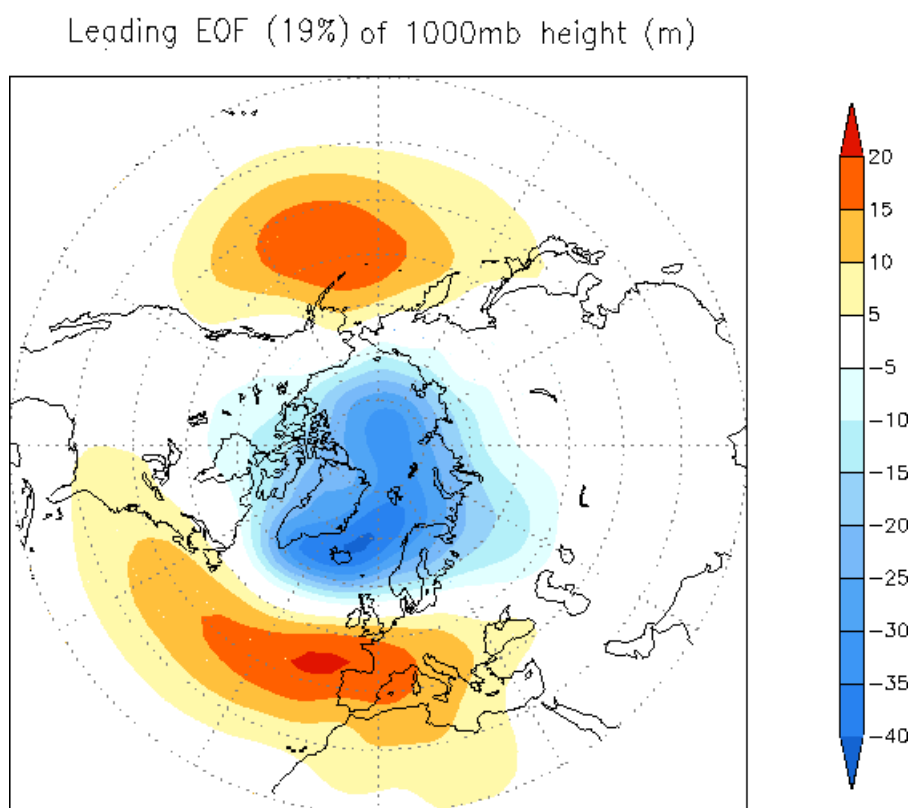


Figure 4.15: The AO spatial pattern (NOAA CPC, 2020a).

The AO pattern is likely related to global weather patterns. In fact, at approximately 55°N latitude there are winds circulating counterclockwise around the Arctic<sup>5</sup> and, when the AO is in its positive phase, these winds become stronger and act in such a way to confine colder air across polar regions. On the contrary, this belt of winds becomes weaker during the negative phase of the AO, which allows an easier southward penetration of colder arctic air masses and increased storminess into the mid-latitudes (Thompson and Wallace, 2001). The positive phase is associated to a negative pressure anomaly over the Polar region and to a

<sup>5</sup>Westerlies are eastward winds specific of the Ferrel circulation cell, which oscillate around the mid-latitudes and generate a jet-stream at high altitudes (9-12 km).

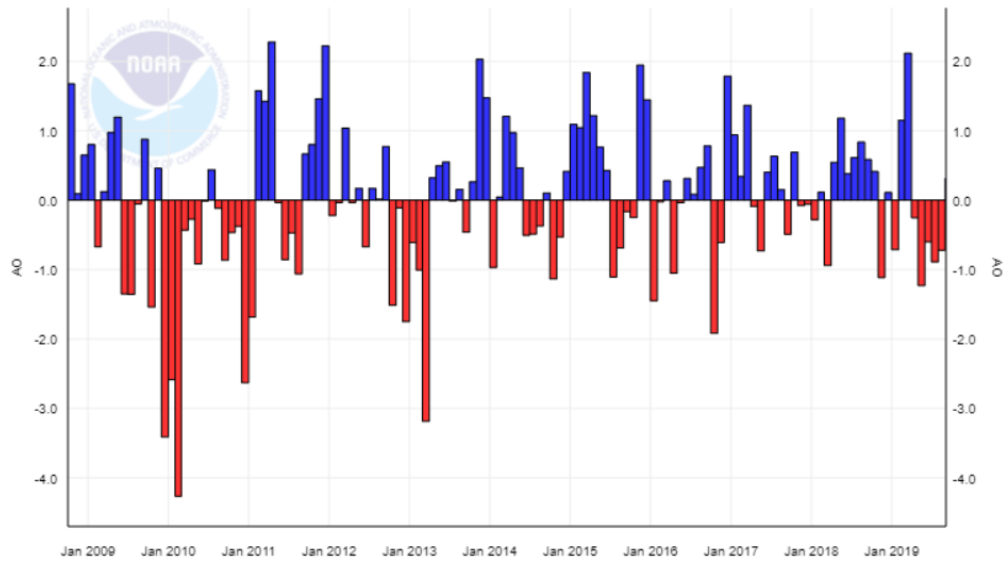


Figure 4.16: AO positive and negative phases (NOAA NCDC, 2010).

positive one over mid-latitudes, while an opposite behaviour is detected during the negative phase (Figure 4.17).

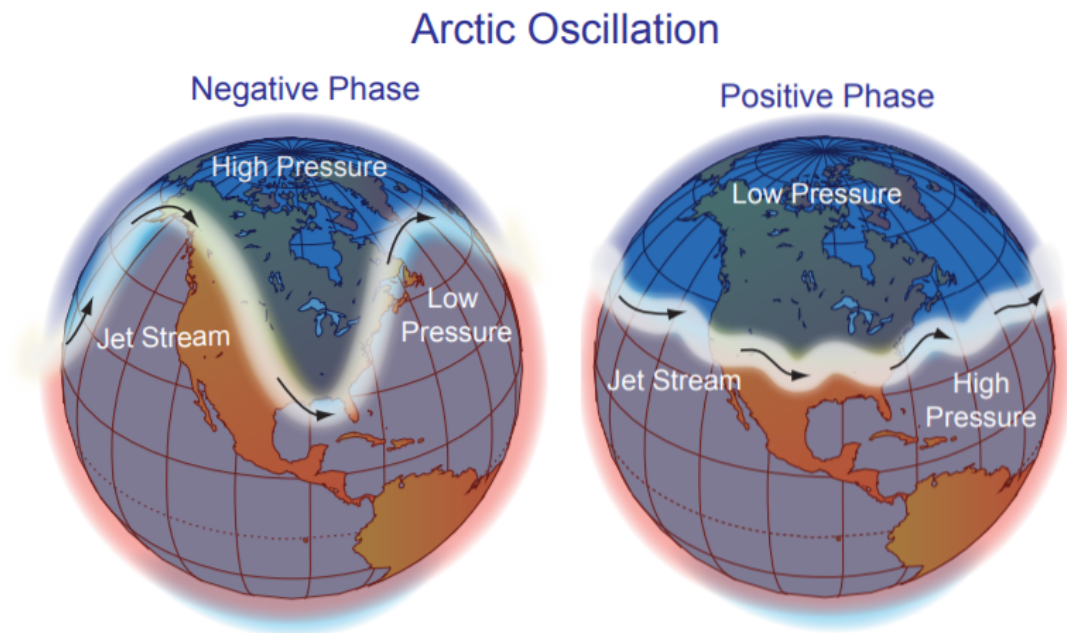


Figure 4.17: Graphic representation of the AO positive and negative phases (NOAA NCDC, 2010).

The AO index shows a significant correlation with the third GPS Up time component (Figure 4.18), which best describes the British Isles and Southeastern Europe (Figure 3.5, p. 39). In fact, the correlation map (Figure 4.19) shows significant positive correlations over Western Europe (the British Isles, Northwestern France, Denmark, Netherlands, Belgium, the Iberian and Scandinavian Peninsula), where the number of GPS sites showing a correlation larger than 10% with a

significance level larger than 95% is 32 (Table 4.4).

Two additional GPS Up time series are correlated with the AO index; they are MOBN (with a positive correlation coefficient) in Western Russia and AUT1 (with a negative correlation coefficient) in the Balkans.

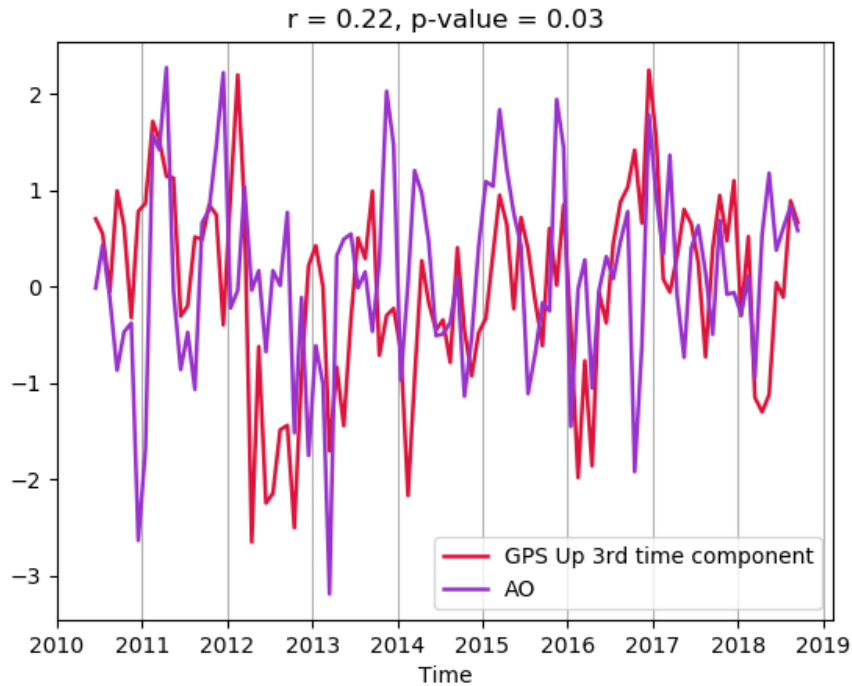


Figure 4.18: Comparison between the GPS Up third time component and the AO index.

	N. GPS Up time series
$ r  \geq 10\%$	69
significance level $\leq 95\%$	37
$ r  \geq 10\%$ & significance level $> 95\%$	31
$ r  \geq 10\%$ & significance level $> 99\%$	14

Table 4.4: Number of GPS sites for each of the following conditions: correlation coefficient ( $r$ ) in absolute value higher or equal to 10%; significance level lower or equal to 95%; correlation coefficient ( $r$ ) in absolute value higher or equal to 10% and significance level larger than 95%; correlation coefficient ( $r$ ) in absolute value higher or equal to 10% and significance level larger than 99%.

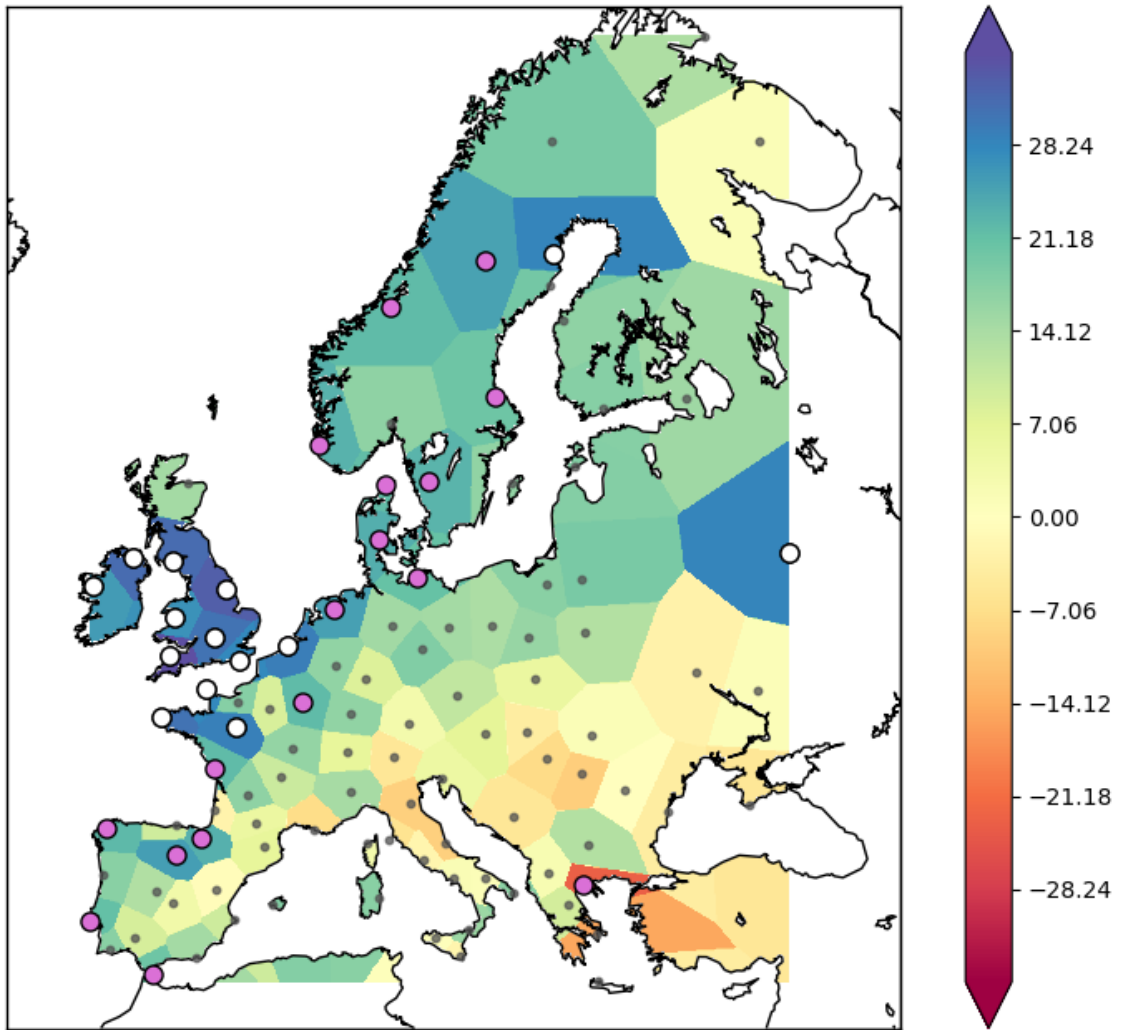


Figure 4.19: Correlation map of the GPS Up time series and the AO index. The GPS sites the Up time series of which show a correlation with the AO index larger than 10% with a significance level larger than 95% are identified by lilac points; those sites with correlation above the same threshold and a significance level larger than 99% are identified by white points.

### 4.3 Tropical North Atlantic (TNA)

The Tropical North Atlantic (TNA) is a climate index calculated using sea surface temperature (SST) data and the Reynolds Optimum Interpolation (Reynolds and Smith, 1994). Since the TNA is calculated with SST in the area identified by the longitude and latitude ranges  $55^{\circ}\text{W} - 15^{\circ}\text{W}$ ,  $5^{\circ}\text{N} - 25^{\circ}\text{N}$  (Figure 4.20), this index is an indicator of the surface temperatures in the tropical Northeastern Atlantic Ocean. The TNA definition implies that positive values of the climate index are associated to positive anomalies of the SST in the North Atlantic Tropical Zones, while negative values are associated to negative anomalies.

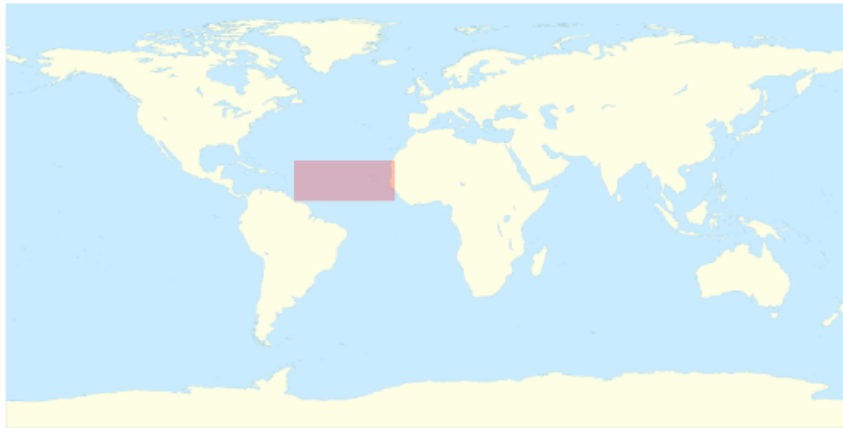


Figure 4.20: Area relevant to the TNA SST index.

The TNA index shows a significant negative correlation ( $-20\%$ ) with the first time components of the GPS Up time series (Figure 4.21), and a significant correlation ( $32\%$ ) with the fourth one (Figure 4.22).

The correlation map (Figure 4.23) is characterized by correlation values which are positive and larger in Western and Northern Europe and the Mediterranean, while they tend to zero in Eastern Europe, with a few negative values towards South-West Russia and Ukraine. This pattern might suggest a link between variations of the SST in the Atlantic Ocean and the observed GPS Up coordinate variations over Europe and the Mediterranean.

The number of GPS Up time series which exhibit a significant correlation with the TNA index is 40, 19 of which with a significance level larger than  $99\%$  (Table 4.5).

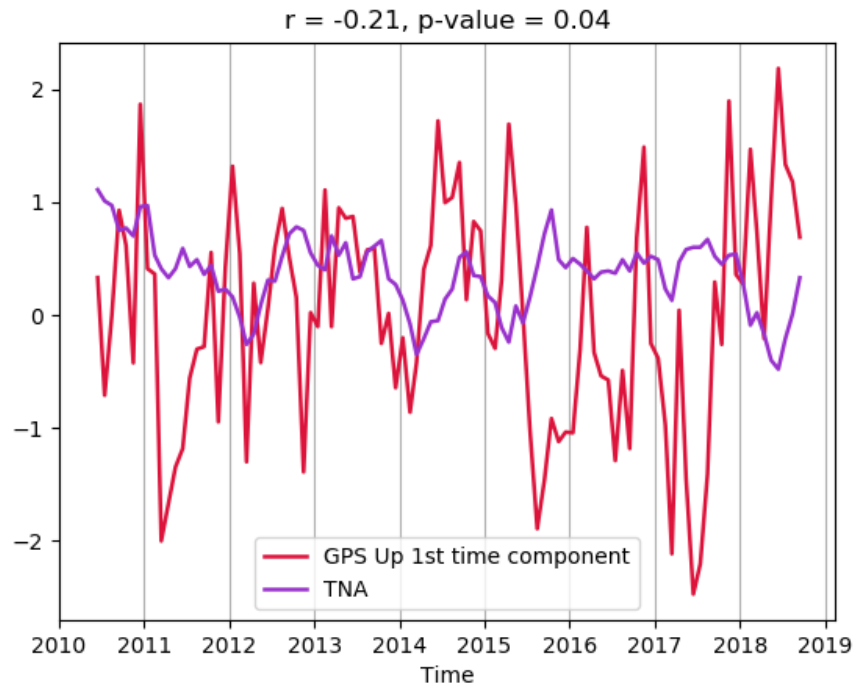


Figure 4.21: Comparison between the GPS Up first time component and the TNA index.

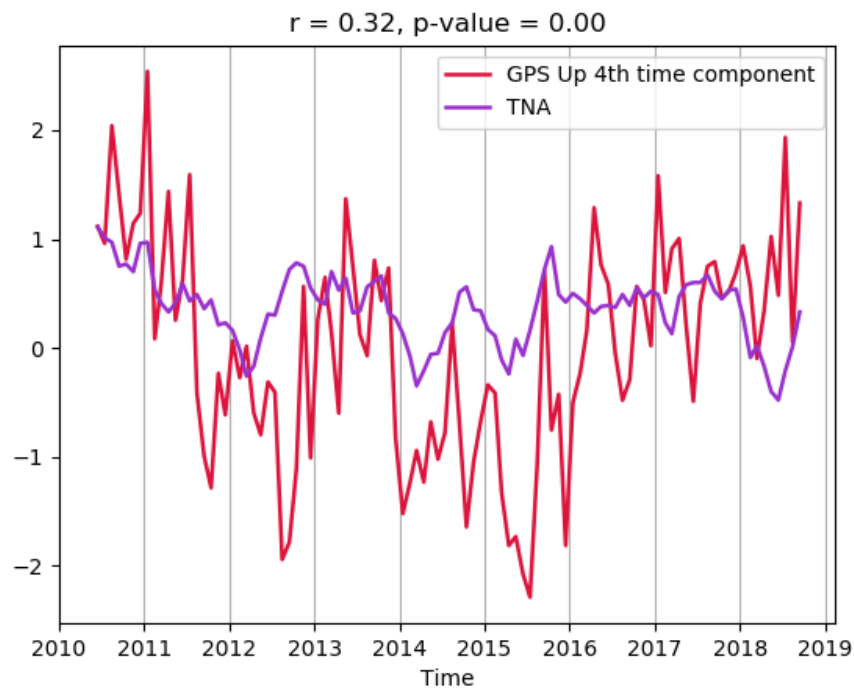


Figure 4.22: Comparison between the GPS Up fourth time component and the TNA index.

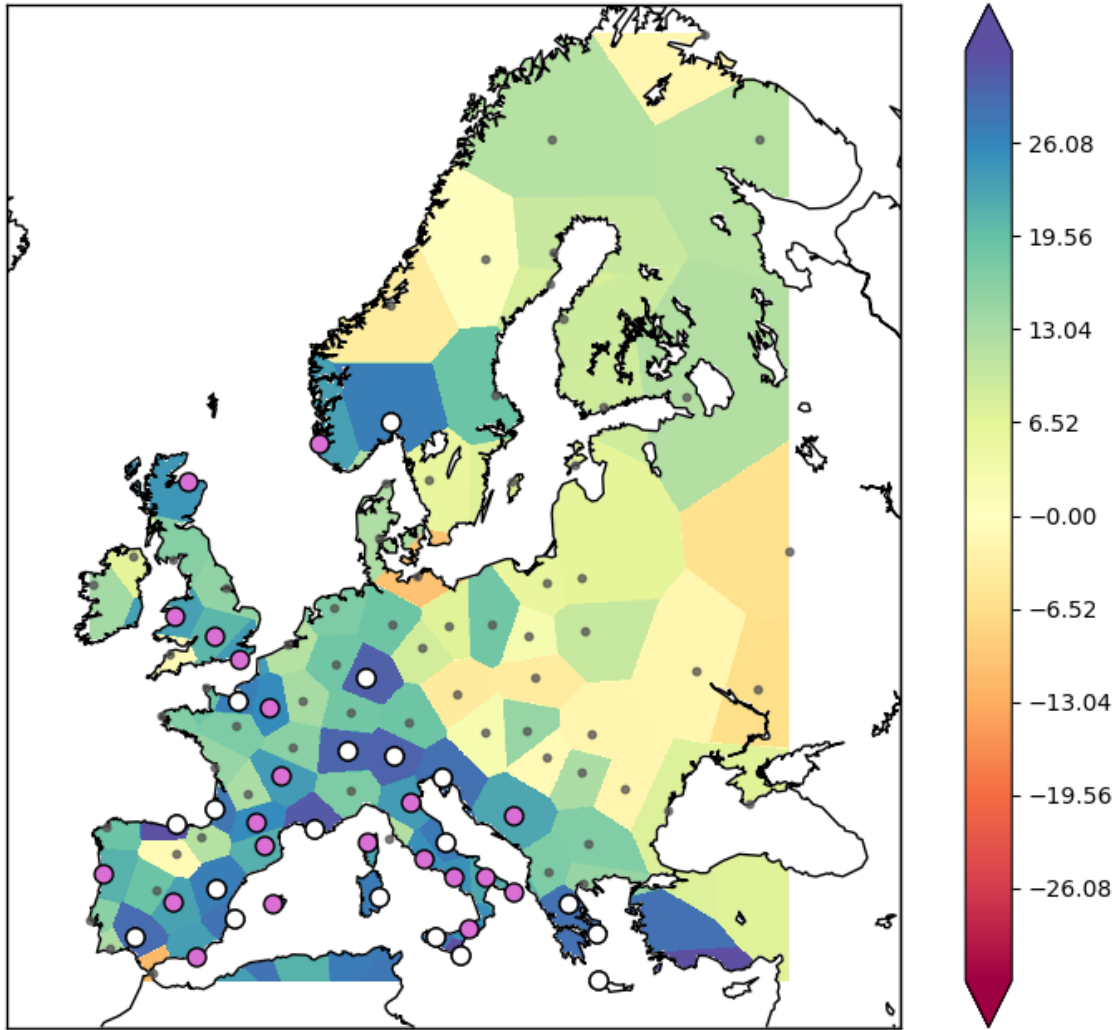


Figure 4.23: Correlation map of the GPS Up time series and the TNA index. The GPS sites the Up time series of which show a correlation with the TNA index larger than 10% with a significance level larger than 95% are identified by lilac points; those sites with correlation above the same threshold and a significance level larger than 99% are identified by white points.

	N. GPS Up time series
$ r  \geq 10\%$	78
significance level $\leq 95\%$	38
$ r  \geq 10\%$ & significance level $> 95\%$	40
$ r  \geq 10\%$ & significance level $> 99\%$	19

Table 4.5: Number of GPS sites for each of the following conditions: correlation coefficient ( $r$ ) in absolute value higher or equal to 10%; significance level lower or equal to 95%; correlation coefficient ( $r$ ) in absolute value higher or equal to 10% and significance level larger than 95%; correlation coefficient ( $r$ ) in absolute value higher or equal to 10% and significance level larger than 99%.

## 4.4 Multivariate ENSO Index Version 2 (MEI v2)

The last climate index studied in this work is the Multivariate ENSO Index Version 2 (MEI v2). The MEI v2 combines both oceanic and atmospheric variables in a single index to provide an assessment of the El Niño Southern Oscillation (ENSO).

ENSO is a periodic fluctuation (i.e. 2-7 years) in SST and air pressure of the overlying atmosphere across the equatorial Pacific ocean (NOAA CPC, 2020d). The ENSO consists in the alternation of two phases:

- a warm phase called El Niño, in which the trade winds<sup>6</sup> experience a weakening and this causes a warming of the equatorial East Pacific and a cooling of the West Pacific, near Indonesia (Figure 4.24a);
- a cold phase called La Niña, in which the trade winds becomes stronger, the equatorial East Pacific becomes cooler and the West Pacific becomes warmer (Figure 4.24b).

It is well known that ENSO affects global climate variability and teleconnections with Central and Eastern Europe have been reported (Bartholy and Pongracz, 2006 and Shaman and Tziperman, 2011).

The MEI v2 index gives real time indications of ENSO intensity. This climate index is the time series of the leading combined PCA of five different variables:

- sea level pressure;
- sea surface temperature;
- zonal components of the surface winds;
- meridional components of the surface winds;
- outgoing longwave radiation.

These variables are related to the tropical Pacific basin (30°S-30°N and 100°E-70°W). The PCA study is applied to 12 overlapping bi-monthly "seasons" (Dec-Jan, Jan-Feb, Feb-Mar,..., Nov-Dec) in order to take into account the seasonality of ENSO, and reduce effects of higher frequency intraseasonal variability (NOAA PSD, 2019).

---

<sup>6</sup>The trade winds or easterlies are the permanent east-to-west prevailing winds that flow in the Earth's equatorial region (between 30°N - 30°S).

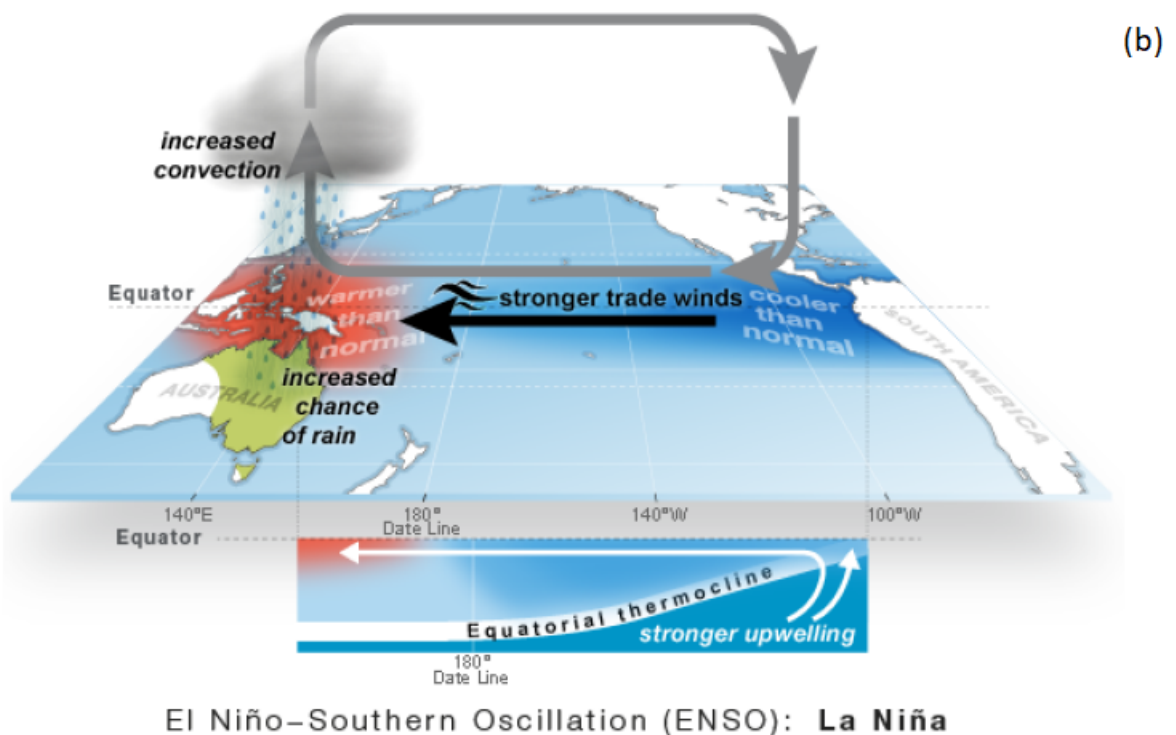
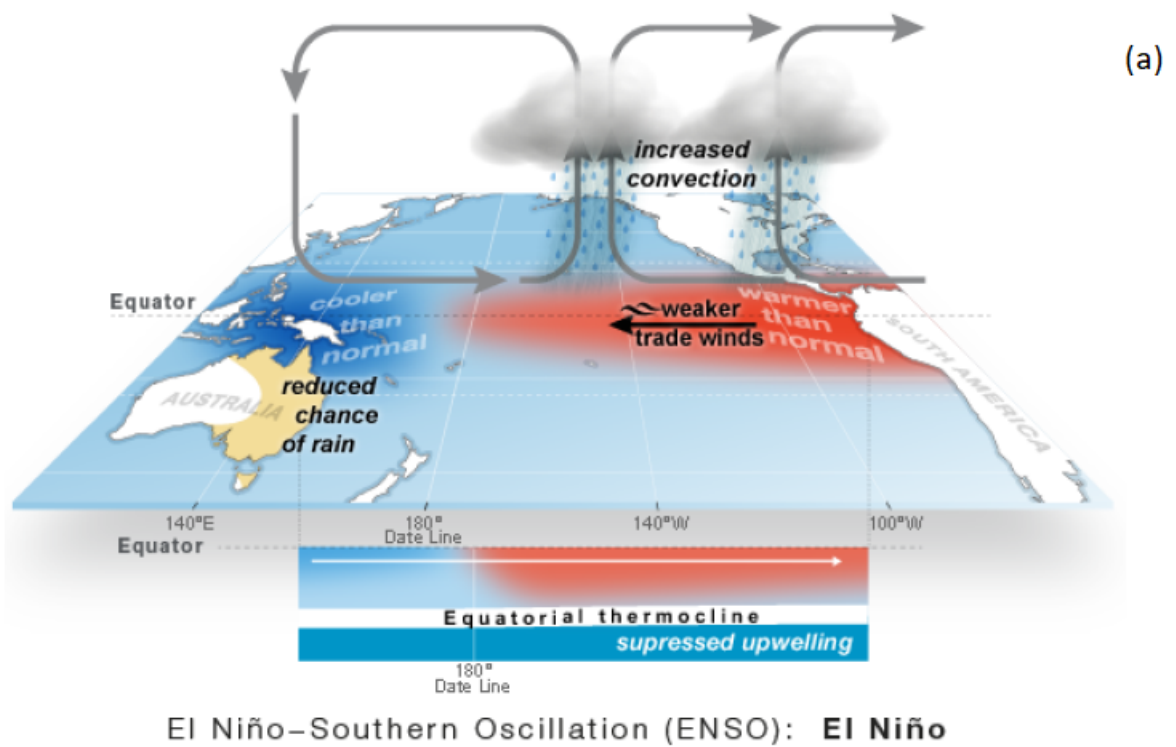


Figure 4.24: Schematic representation of El Niño (a) and La Niña (b) (Doyle, 2018). Red and blue mean higher and lower SST, respectively.

The positive and negative phases of ENSO correspond to positive and negative values of the MEI v2 index (4.25).

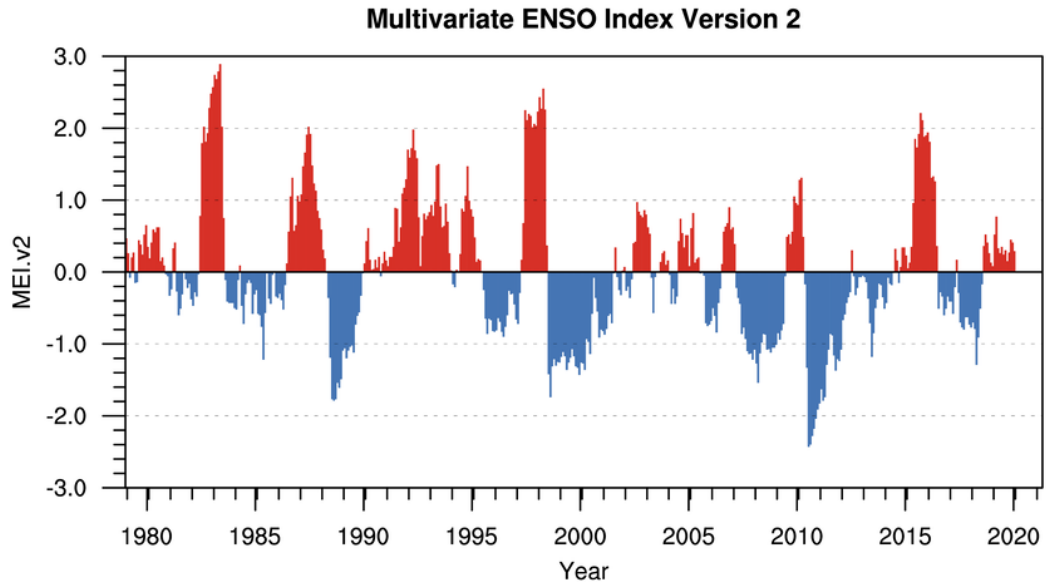


Figure 4.25: The MEI v2 time series; red represents the warm phase (El Niño) and blue the cold phase (La Niña).

The MEI v2 index shows significant correlations with the second (26%), third (-24%) and fourth (-46%) time component of the GPS Up time series (Figures 4.26, 4.27 and 4.28).

The correlation map between the MEI v2 index and the GPS Up time series represented through the first four modes shows significant correlations particularly in Central-Eastern Europe, where the Up time series of many GPS stations show a correlation coefficient with the MEI index greater than 30% with a significance level larger than 99%.

The number of GPS sites which exhibit a significant correlation with the MEI v2 index is approximately half of the total number of stations considered in this work (46 out of 107; Table 4.6), and is second only to the corresponding number of GPS sites in the EA study (Table 4.2, p. 79).

In the case of the comparison with the MEI v2 index, three of the four principal modes of variability of the GPS Up coordinate show a significant correlation. This behaviour can also be related to the results obtained by the SVD analysis of the pairs TWS-GPS Up and SP-GPS Up showing the effects of water and pressure variations over Europe and the Mediterranean. However it has been proved that phenomenon ENSO induces effects at global scale, capable of changing the Earth's

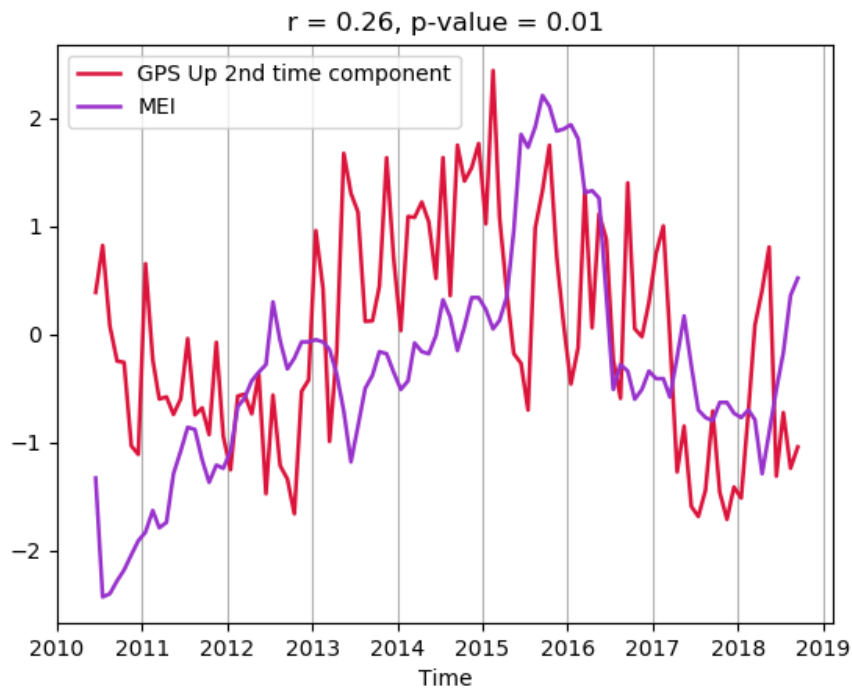


Figure 4.26: Comparison between the GPS Up second time component and the MEI index.

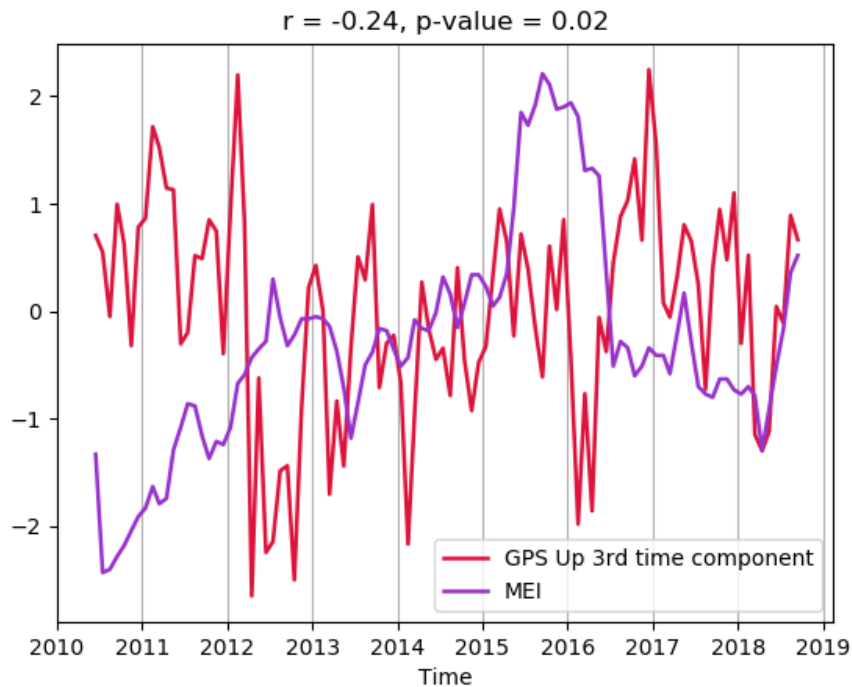


Figure 4.27: Comparison between the GPS Up third time component and the MEI index.

shape, most notably the Earth's polar flattening (Cheng and Tapley, 2004; Cheng, Tapley, and Ries, 2013).

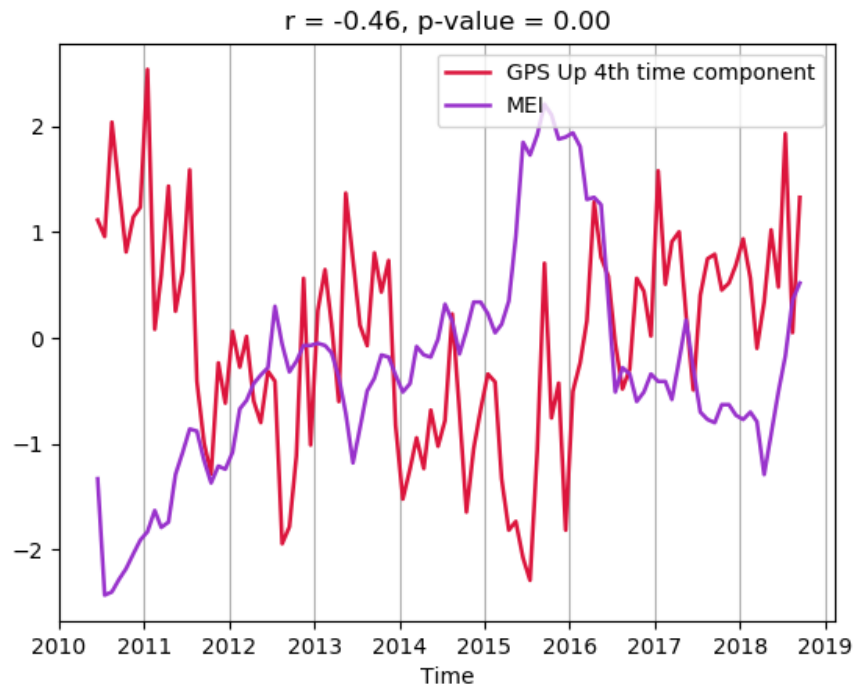


Figure 4.28: Comparison between the GPS Up fourth time component and the MEI index.

	N. GPS Up time series
$ r  \geq 10\%$	79
significance level $\leq 95\%$	33
$ r  \geq 10\%$ & significance level $> 95\%$	46
$ r  \geq 10\%$ & significance level $> 99\%$	31

Table 4.6: Number of GPS sites for each of the following conditions: correlation coefficient ( $r$ ) in absolute value higher or equal to 10%; significance level lower or equal to 95%; correlation coefficient ( $r$ ) in absolute value higher or equal to 10% and significance level larger than 95%; correlation coefficient ( $r$ ) in absolute value higher or equal to 10% and significance level larger than 99%.

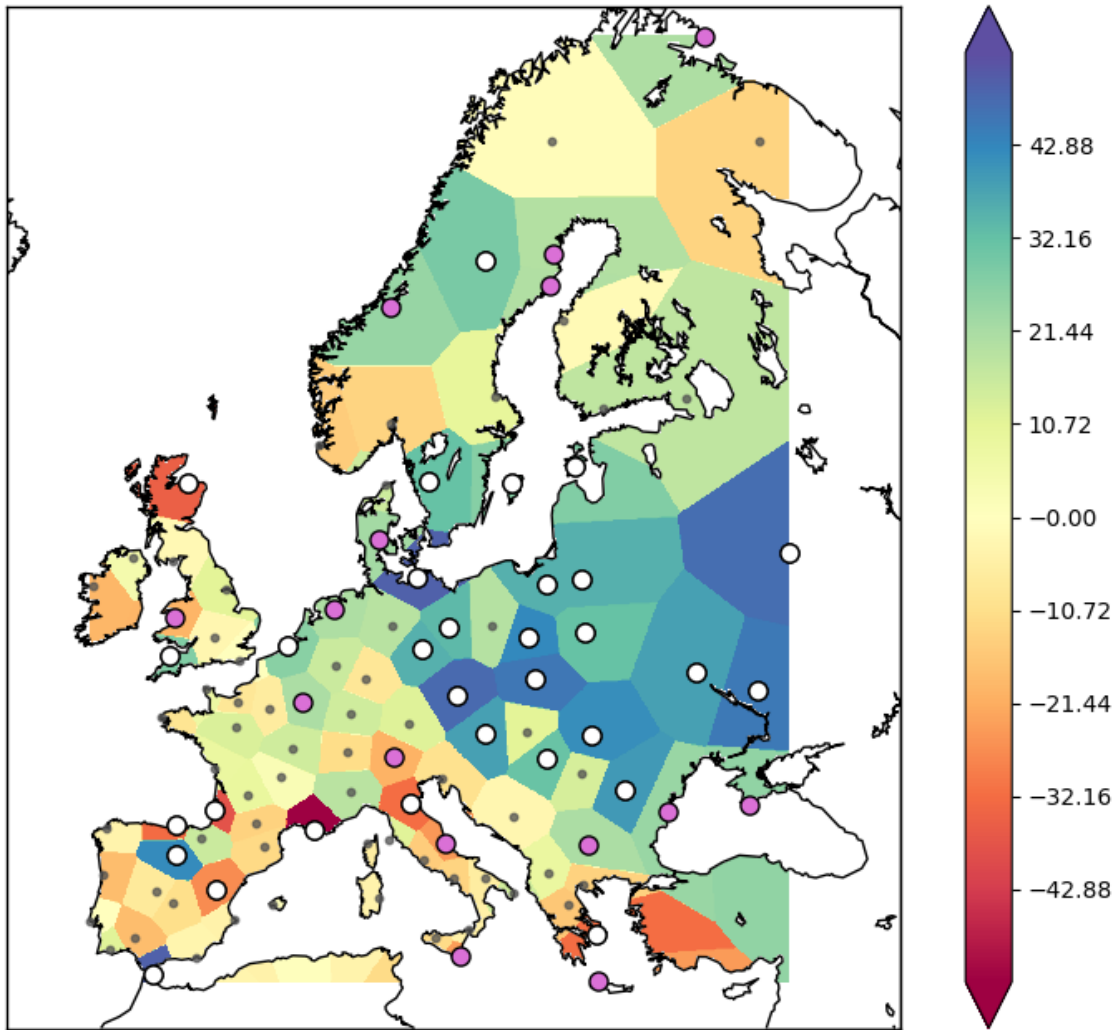


Figure 4.29: Correlation map of the GPS Up time series and the MEI index. The GPS sites the Up time series of which show a correlation with the MEI index larger than 10% with a significance level larger than 95% are identified by lilac points; those sites with correlation above the same threshold and a significance level larger than 99% are identified by white points.



# Conclusions

The Earth's crust undergoes deformations of different nature. In this thesis, vertical displacements were studied in relation to changes in environmental parameters, such as atmospheric surface pressure (SP) and terrestrial water storage (TWS), and to climate indices. In fact, loading effects due to variations of the mass of the atmosphere and of that of TWS cause elastic deformation of the solid Earth. It is worth recalling that, in the case of the atmospheric pressure, this effect can reach 15-20 mm. Among the GPS stations, with time series of coordinates freely available, 107 location were selected in the European and Mediterranean area.

The stations were chosen in such a way to create a network as uniform as possible over the area of interest and on the basis of the length and completeness of the coordinate time series.

The coordinate analyzed in this work is the height of the stations, represented by the local Up coordinate, because it is the one for which the loading/unloading effects caused by the environmental parameters are best explained.

The data series of the investigated parameters cover a period of about 8 years, from June, 9, 2010 to September, 5, 2018. All time series were detrended (linear trend removed) and deseasonalized (annual cycle removed) so that the residual time series of the parameters should be representative of intra-and inter-annual variations.

A principal component analysis (PCA) was adopted to identify the main modes of variability of the three parameters, namely the GPS Up coordinate, the SP and the TWS. Each mode is described by both a spatial pattern and by a time component.

In all the three cases, the first four modes of variability were considered because they explain a large percentage of the total variability. Significant interannual signals were identified in the time components. In the case of the GPS Up and the TWS, the first four modes of variability explain about 50% and 65% of the total variance, respectively. Different short-term local effects might be the source of the remaining variance in the time series. In the case of SP, the first mode alone explains 50% of the total variance, while the first four modes together account for 90% of the total variance. This indicates that the SP residual time series represent continental-scale features well emerging above local characteristics.

All the first time components are characterized by a peak at the end of 2010, which represents a negative variation for the SP and the GPS Up, but a positive one for the TWS. This behaviour is followed by a change of slope in early 2011. In fact the whole late 2010 was characterized by a strong rainfall period all over Europe, followed by a drought that started in the spring 2011 in Southeastern Europe and that extended to the rest of the continent till about 2012. It is possible to identify, in the second time component of the SP, in the first and third GPS Up coordinate and in the first one of the TWS a peak in the early 2012 that might be attributed to the extensive area of high pressure in Northeastern Europe that was responsible, in general, for precipitation deficits in the continent.

In order to check if the results of the principal component analysis applied to the GPS Up time series are sensitive to the selected time interval and to the number of available stations, the analysis was also performed considering a smaller ensemble of GPS Up time series (42). In this case, the period is of about 17 years, from June, 9, 2001 to September, 5, 2018. The analysis confirmed that the first three modes of variability are nearly independent from these two constraints.

In order to identify possible common modes of variability between pairs of variable, the SVD methodology was adopted. The studied pairs were the GPS Up coordinate and the SP and the GPS Up with the TWS. This analysis mostly confirms the expected coupled variability between the two pairs of parameters.

As regards the GPS Up coordinate and the SP, the first three modes explain about 70% of the total covariance. The first mode explains 35.2% and the spatial pattern of the SP is coherent all over the study area, while the spatial pattern of the GPS Up does exhibit complete coherence over the European and Mediterranean area. Clear exceptions are the British Isles and a few zones in the Scandinavia. However, most Central-Northern Europe and the central Mediterranean behave in a coherent way. The two spatial patterns are anti-correlated for about 70 of the total 107 locations. The anticorrelation can be explained with the loading effect caused by atmospheric pressure variations on the Earth's crust. In those areas where anticorrelation is not found, additional factors shall be investigated that may mask the well-known loading effect.

For the pair GPS UP and TWS, the first three modes explain about 50% of the total covariance. The spatial pattern of the first modes are mostly characterized by anticorrelation indicating that this mode could represent the vertical deformation induced by hydrological mass loading. The time series are in general agreement with the behaviour of the annual European precipitation relative to 1981-2010, as provided by ERA-Interim, which shows loss of rain between 2010-2011, 2014-2015 and 2016-2017, while there was a recovery between 2011-2014 (Copernicus Climate Change Service, 2017).

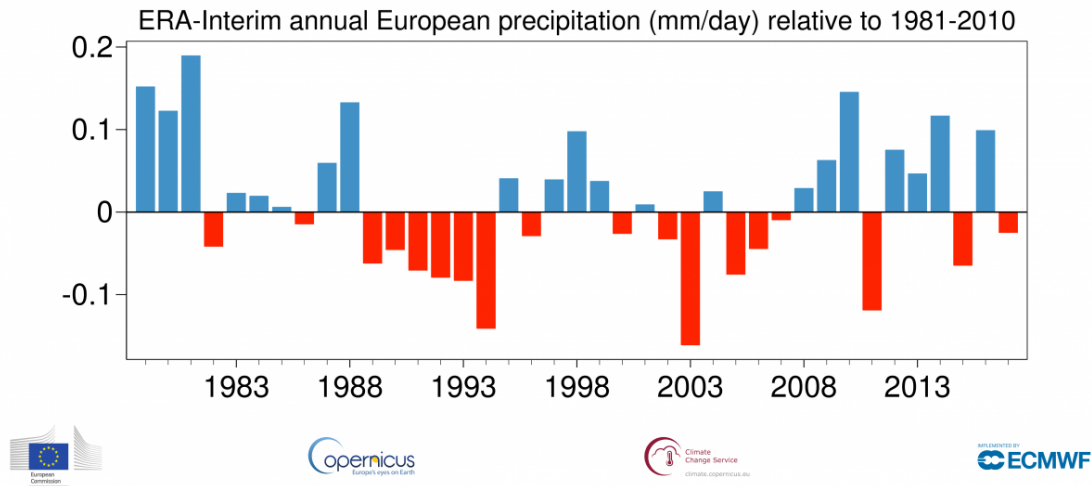


Figure 4.30: Annual European precipitation anomalies from 1979 to 2017, relative to the annual average for the period 1981-2010 (Copernicus Climate Change Service, 2017).

The principal modes of variability of the GPS Up coordinate were also compared with climate indices (NAO, EA, SCAND, AO, TNA, MEI) and correlation maps between the climate indices and the dimensionality-reduced GPS Up time series were analyzed. The correlation patterns found in all the Northern Hemisphere pressure indices (NAO, EA, SCAND) present strong similarities with the spatial patterns of the first four GPS Up modes of variability. The lowest correlation was found between the NAO index and the GPS Up time series, of which only 12 among the total of 107 showed a significant correlation. The SCAND index shows a north-east to south-west gradient, presenting significant correlations with the GPS Up time series of stations in Scandinavia and anticorrelations with those in the Iberian Peninsula, France and the Mediterranean area. The EA index has significant correlations with more than half of the GPS Up time series taken into account (63 over 107). The correlation map between the EA index and the GPS Up time series exhibit the same features of the first spatial pattern of the GPS Up. In fact, the time series of this climate index shows the same characteristics of the first time component of the GPS Up. The AO index is defined as the leading mode of a PCA analysis applied to Northern Hemisphere sea level pressure data. The correlation map with the GPS Up shows significant positive correlations in the area of the British Isles and northern France. The TNA index is an indicator of the surface temperature in the tropical Northeastern Atlantic Ocean. The correlation pattern obtained shows significant and positive correlation values in Western, Central Europe and the Mediterranean area.

The results of the PCA presented in this thesis have shown that interannual vertical movements of the Earth's crust at continental scale are likely responsive to the forcing caused by variations of a number of climate-related parameters (Zerbini, Raicich, et al., 2013). The MEI v2 index reflects the characteristics of the ENSO

phenomenon and is based on five main variables. They are: sea-level pressure, sea surface temperature, zonal and meridional components of surface winds and outgoing longwave radiation. The comparison of the first four time components of the GPS Up with the MEI v2 index shows correlations with significance equal or larger than 99% for the second, third and fourth modes of variability. In particular, the fourth time component (Figure 3.8), although explaining a small percentage of variance, is characterized by a correlation coefficient with MEI v2 equal to -0.46. The slope change occurring at the beginning of 2015 at the end of 5-year ENSO negative state is recognizable in both the MEI (Figure 4.25) and in the fourth time component of the GPS Up coordinate (Figure 3.8). Similar features can also be recognized in the third (Figure 3.6) and second (Figure 3.4) time components. The spatial distribution of this modes of variability seems to indicate two different coherent behaviours over the network. One is that of the stations located in the north and in the south, namely in Ireland, northern Great Britain, Scandinavia, central and southeastern Mediterranean. The other one refers to the stations located in Spain, Central and Eastern Europe.

These results are indicative of the fact that fingerprints of ENSO, which is a complex global scale phenomenon, can be clearly identified in the time series of the height coordinate of the GPS stations. Nevertheless, the physical processes causing the observed modulations of the observed signals are still lacking adequate understanding.

# Bibliography

- Abdi, Hervé and Lynne J. Williams (2010)  
“Principal component analysis”. In: *WIREs Computational Statistics* 2.4, pp. 433–459. DOI: 10.1002/wics.101. eprint: <https://onlinelibrary.wiley.com/doi/pdf/10.1002/wics.101>. URL: <https://onlinelibrary.wiley.com/doi/abs/10.1002/wics.101>.
- Baarda, W. (Nov. 1968)  
“A testing procedure for use in geodetic networks”. In: *Geodesy* 9 2.5, p. 97.
- Barnston, Anthony G. and Robert E. Livezey (1987)  
“Classification, Seasonality and Persistence of Low-Frequency Atmospheric Circulation Patterns”. In: *Monthly Weather Review* 115.6, pp. 1083–1126. DOI: 10.1175/1520-0493(1987)115<1083:CSAPOL>2.0.CO;2. URL: [https://doi.org/10.1175/1520-0493\(1987\)115%3C1083:CSAPOL%3E2.0.CO;2](https://doi.org/10.1175/1520-0493(1987)115%3C1083:CSAPOL%3E2.0.CO;2).
- Bartholy, J. and R. Pongracz (2006)  
“Regional effects of ENSO in Central/Eastern Europe.” In: *Advances in Geosciences* 6, pp. 133–137. DOI: 10.5194/adgeo-6-133-2006.
- Beckers, J. M. and M. Rixen (2003)  
“EOF Calculations and Data Filling from Incomplete Oceanographic Datasets”. In: *Journal of Atmospheric and Oceanic Technology* 20.12, pp. 1839–1856. DOI: 10.1175/1520-0426(2003)020<1839:ECADFF>2.0.CO;2.
- Bertacchi Uvo, C., J. Olsson, O. Morita, K. Jinno, A. Kawamura, K. Nishiyama, N. Koreeda, and T. Nakashima (2001)  
“Statistical atmospheric downscaling for rainfall estimation in Kyushu Island, Japan”. In: *Hydrology and Earth System Sciences Discussions* 5.2, pp. 259–271. URL: <https://hal.archives-ouvertes.fr/hal-00304603>.
- Bigot, S. and O. Planchon (2003)  
“Identification and characterization of sea breeze days in northern France using singular value decomposition”. In: *International Journal of Climatology* 23.11, pp. 1397–1405. DOI: 10.1002/joc.940. eprint: <https://rmets.onlinelibrary.wiley.com/doi/pdf/10.1002/joc.940>. URL: <https://rmets.onlinelibrary.wiley.com/doi/abs/10.1002/joc.940>.
- Bissolli, P., M. Ziese, S. Pietzsch, P. Finger, K. Friedrich, H. Nitsche, and A. Obregon (2012)  
“Drought conditions in Europe in the spring of 2012”. In: *Deutscher Wetterdienst*.
- Bjornsson, H. and S. Venegàs (1997)  
*A Manual for EOF and SVD Analyses of Climatic Data*. McGill University.

- URL: [http://archipelago.uma.pt/pdf\\_library/Bjornsson%5C&Venegas\\_1997\\_McGill.pdf](http://archipelago.uma.pt/pdf_library/Bjornsson%5C&Venegas_1997_McGill.pdf).
- Blewitt, G, W.C. Hammond, and C. Kreemer (2018)  
 “Harnessing the GPS Data Explosion for Interdisciplinary Science”. In: *Eos* 99. DOI: 10.1029/2018E0104623.
- Blewitt, Geoffrey and David Lavallée (2002)  
 “Effect of annual signals on geodetic velocity”. In: *Journal of Geophysical Research: Solid Earth* 107.B7, ETG 9-1-ETG 9–11. DOI: 10.1029/2001JB000570. eprint: <https://agupubs.onlinelibrary.wiley.com/doi/pdf/10.1029/2001JB000570>. URL: <https://agupubs.onlinelibrary.wiley.com/doi/abs/10.1029/2001JB000570>.
- Blewitt, Geoffrey, David Lavallée, Peter Clarke, and Konstantin Nurutdinov (Jan. 2001)  
 “A New Global Mode of Earth Deformation: Seasonal Cycle Detected”. In: *Science (New York, N.Y.)* 294, pp. 2342–5. DOI: 10.1126/science.1065328.
- Boczoń, Andrzej, Anna Kowalska, Małgorzata Dudzińska, and Michał Wróbel (Oct. 2016)  
 “Drought in Polish Forests in 2015”. In: *Polish Journal of Environmental Studies* 25. DOI: 10.15244/pjoes/62797.
- Boscardin, W.J. and X. Zhang (2004)  
 “Modeling the covariance and correlation matrix of repeated measures”. In: *Applied Bayesian Modeling and Causal Inference from an Incomplete-Data Perspective*. Ed. by A. Gelman and X.-L. Meng. New York: John Wiley & Sons. DOI: 10.1002/0470090456.ch20.
- Burt, S and T. Burt (2019)  
*Oxford Weather and Climate since 1767*. Oxford University Press. ISBN: 9780198834632.
- Cheng, Minkang and Byron D. Tapley (2004)  
 “Variations in the Earth’s oblateness during the past 28 years”. In: *Journal of Geophysical Research: Solid Earth* 109.B9. DOI: 10.1029/2004JB003028. eprint: <https://agupubs.onlinelibrary.wiley.com/doi/pdf/10.1029/2004JB003028>. URL: <https://agupubs.onlinelibrary.wiley.com/doi/abs/10.1029/2004JB003028>.
- Cheng, Minkang, Byron D. Tapley, and John C. Ries (2013)  
 “Deceleration in the Earth’s oblateness”. In: *Journal of Geophysical Research: Solid Earth* 118.2, pp. 740–747. DOI: 10.1002/jgrb.50058. eprint: <https://agupubs.onlinelibrary.wiley.com/doi/pdf/10.1002/jgrb.50058>. URL: <https://agupubs.onlinelibrary.wiley.com/doi/abs/10.1002/jgrb.50058>.
- Compagnucci, Rosa H., Diego Araneo, and Pablo O. Canziani (2001)  
 “Principal sequence pattern analysis: a new approach to classifying the evolution

- of atmospheric systems.” In: *International Journal of Climatology* 21.2, pp. 197–217. DOI: 10.1002/joc.601.
- Copernicus Climate Change Service (2017)  
*Climate in 2017 - European wet and dry indicators*. URL: <https://climate.copernicus.eu/climate-2017-european-wet-and-dry-indicators>.
- Dam, T. van, X. Collilieux, J. Wuite, Z. Altamimi, and J. Ray (2012)  
“Nontidal ocean loading: amplitudes and potential effects in GPS height time series”. In: *Journal of Geodynamics* 86, pp. 1043–1057. DOI: 10.1007/s00190-012-0564-5. URL: <https://link.springer.com/article/10.1007%5C%2Fs00190-012-0564-5>.
- Dam, T. van, J. Wahr, P. C. D. Milly, A. B. Shmakin, G. Blewitt, D. Lavallée, and K. M. Larson (2001)  
“Crustal displacements due to continental water loading”. In: *Geophysical Research Letters* 28.4, pp. 651–654. DOI: 10.1029/2000GL012120. eprint: <https://agupubs.onlinelibrary.wiley.com/doi/pdf/10.1029/2000GL012120>. URL: <https://agupubs.onlinelibrary.wiley.com/doi/abs/10.1029/2000GL012120>.
- Dam, T.M. van and J. Wahr (1998)  
“Modeling environment loading effects: a review”. In: *Physics and Chemistry of the Earth* 23.9, pp. 1077–1087. ISSN: 0079-1946. DOI: [https://doi.org/10.1016/S0079-1946\(98\)00147-5](https://doi.org/10.1016/S0079-1946(98)00147-5). URL: <http://www.sciencedirect.com/science/article/pii/S0079194698001475>.
- Darwin, G.H. (1882)  
“XLVI. On variations in the vertical due to elasticity of the earth’s surface”. In: *The London, Edinburgh, and Dublin Philosophical Magazine and Journal of Science* 14.90, pp. 409–427. DOI: 10.1080/14786448208628439. eprint: <https://doi.org/10.1080/14786448208628439>. URL: <https://doi.org/10.1080/14786448208628439>.
- Doyle, K. (2018)  
*What El Niño and La Niña actually mean for Australian and world weather*. URL: <https://www.abc.net.au/news/2017-10-19/what-el-nino-la-nina-mean-australian-weather/9053464>.
- Dray, Stéphane and Julie Josse (May 2014)  
“Principal component analysis with missing values: a comparative survey of methods”. In: *Plant Ecology* 216. DOI: 10.1007/s11258-014-0406-z.
- Dvorský, J., V. Snášel, and V. Voženílek (Nov. 2009)  
“Map Similarity Testing Using Matrix Decomposition”. In: *2009 International Conference on Intelligent Networking and Collaborative Systems*, pp. 290–294. DOI: 10.1109/INCOS.2009.74.

- Eccel, Emanuele, Piero Cau, Kathrin Riemann-Campe, and Franco Biasioli (2012)  
 “Quantitative hail monitoring in an alpine area: 35-year climatology and links with atmospheric variables”. In: *International Journal of Climatology* 32.4, pp. 503–517. DOI: 10.1002/joc.2291. eprint: <https://rmets.onlinelibrary.wiley.com/doi/pdf/10.1002/joc.2291>. URL: <https://rmets.onlinelibrary.wiley.com/doi/abs/10.1002/joc.2291>.
- Farrell, W. E. (1972)  
 “Deformation of the Earth by surface loads”. In: *Reviews of Geophysics* 10.3, pp. 761–797. DOI: 10.1029/RG010i003p00761. eprint: <https://agupubs.onlinelibrary.wiley.com/doi/pdf/10.1029/RG010i003p00761>. URL: <https://agupubs.onlinelibrary.wiley.com/doi/abs/10.1029/RG010i003p00761>.
- Fonf, D. and W. DeSarbo (2007)  
 “A bayesian methodology for simultaneously detecting and estimating regime change points and variable selection in multiple regression models for marketing research”. In: *Quantitative Marketing and Economics* 5, pp. 427–453.
- Fratepietro, F., T. F. Baker, S. D. P. Williams, and M. Van Camp (2006)  
 “Ocean loading deformations caused by storm surges on the northwest European shelf”. In: *Geophysical Research Letters* 33.6. DOI: 10.1029/2005GL025475. eprint: <https://agupubs.onlinelibrary.wiley.com/doi/pdf/10.1029/2005GL025475>. URL: <https://agupubs.onlinelibrary.wiley.com/doi/abs/10.1029/2005GL025475>.
- Gan, Shuwei, Yangkang Chen, Shaohuan Zu, Shan Qu, and Wei Zhong (Mar. 2015)  
 “Structure-oriented singular value decomposition for random noise attenuation of seismic data”. In: *Journal of Geophysics and Engineering* 12.2, pp. 262–272. ISSN: 1742-2132. DOI: 10.1088/1742-2132/12/2/262. eprint: [https://academic.oup.com/jge/article-pdf/12/2/262/26781247/jge\\_12\\_2\\_262.pdf](https://academic.oup.com/jge/article-pdf/12/2/262/26781247/jge_12_2_262.pdf). URL: <https://doi.org/10.1088/1742-2132/12/2/262>.
- Gazeaux, J., E. Flaounas, P. Naveau, and A. Hannart (2011)  
 “Inferring change points and nonlinear trends in multivariate time series: Application to West African monsoon onset timings estimation”. In: *Journal of Geophysical Research* 116. DOI: 10.1029/2010JD014723, p. D05101.
- Gazeaux, J, S. Williams, M. King, M. Bos, R. Dach, M. Deo, AW. Moore, L. Ostini, E. Petrie, M. Roggero, FN. Teferle, G. Olivares, and FH. Webb (2013)  
 “Detecting offsets in GPS time series: first results from the detection of offsets in GPS experiment”. In: *Journal of Geophysical Research* 118. DOI: 10.1002/jgrb.50152, pp. 2397–2407.
- Gegout, Pascal, Jean-Paul Boy, Jacques Hinderer, and G. Ferhat (Dec. 2009)  
 “Modeling and Observation of Loading Contribution to Time-Variable GPS Sites Positions”. In: vol. 135, pp. 651–659. DOI: 10.1007/978-3-642-10634-7\_86.

- Geng, Jianghui, Simon D.P. Williams, Felix N. Teferle, and Alan H. Dodson (2012)  
“Detecting storm surge loading deformations around the southern North Sea using subdaily GPS”. In: *Geophysical Journal International* 191.2, pp. 569–578. DOI: 10.1111/j.1365-246X.2012.05656.x. eprint: <https://onlinelibrary.wiley.com/doi/pdf/10.1111/j.1365-246X.2012.05656.x>. URL: <https://onlinelibrary.wiley.com/doi/abs/10.1111/j.1365-246X.2012.05656.x>.
- Gerchberg, R. (1974)  
“Super-resolution through error energy reduction”. In: *Optica Acta* 21.9, pp. 709–720. DOI: 10.1080/713818946.
- Giroto, Manuela and Matthew Rodell (2019)  
“Chapter Two - Terrestrial water storage”. In: *Extreme Hydroclimatic Events and Multivariate Hazards in a Changing Environment*. Ed. by Viviana Maggioni and Christian Massari. Elsevier, pp. 41–64. ISBN: 978-0-12-814899-0. DOI: <https://doi.org/10.1016/B978-0-12-814899-0.00002-X>. URL: <http://www.sciencedirect.com/science/article/pii/B978012814899000002X>.
- Global Modeling and Assimilation Office (GMAO) (2015)  
*MERRA-2 tavg1\_2d\_lnd\_Nx: 2d, 1-Hourly, -Averaged, Single-Level, Assimilation, Land Surface Diagnostics V5.12.4, Goddard Earth Sciences Data and Information Services Center (GES DISC), Accessed: [Thu Oct 31 14:26:15 2019]*. Greenbelt, MD, USA. DOI: 10.5067/RKPHT8KC1Y1T. URL: <https://www.esrl.noaa.gov/psd/>.
- Hawkins, D. (1980)  
*Identification of outliers*. eng. ISBN: 978-94-015-3994-4. Chapman and Hall, London.
- Hekimoglu, S. and K. R. Koch (2000)  
“How can reliability of the test for outliers be measured?” In: *Allgemeine Vermessungsnachrichten* 7, pp. 247–253.
- Ilin, Alexander and Tapani Raiko (2010)  
“Practical Approaches to Principal Component Analysis in the Presence of Missing Values”. In: *Journal of Machine Learning Research* 11, pp. 1957–2000. DOI: 10.1029/2018E0104623.
- Ionita, M., L. M. Tallaksen, D. G. Kingston, J. H. Stagge, G. Laaha, H. A. J. Van Lanen, P. Scholz, S. M. Chelcea, and K. Haslinger (2017)  
“Drought in Polish Forests in 2015”. In: *Hydrology Earth System Sciences* 21, pp. 1397–1419. DOI: 10.5194/hess-21-1397-2017.
- Kailath, T., A. Sayed, and B. Hassibi (2000)  
*Linear estimation*. Prentice Hall Information and System Sciences Series. ISBN: 0130224642.

- Kay, Steven M. (1993)  
*Fundamentals of Statistical Signal Processing: Estimation Theory*. USA: Prentice-Hall, Inc. ISBN: 0133457117.
- Lehmann, R. (2013)  
“The  $3\sigma$ -rule for outlier detection from the viewpoint of geodetic adjustment”. In: *Journal of Surveying Engineering* 4. DOI: 10.1061/(ASCE)SU.1943-5428.0000112, pp. 157–165.
- Nakatsukasa, Yuji and Nicholas Higham (Jan. 2013)  
“Stable and Efficient Spectral Divide and Conquer Algorithms for the Symmetric Eigenvalue Decomposition and the SVD”. In: *SIAM Journal on Scientific Computing* 35. DOI: 10.1137/120876605.
- NASA JPL Earth Science Communications Team (2019)  
*Climate Change: how do we know?* URL: <https://climate.nasa.gov/evidence/>.
- NOAA CPC (2000)  
*NAO loading pattern*. URL: [https://www.cpc.ncep.noaa.gov/products/precip/CWlink/pna/nao\\_loading.html](https://www.cpc.ncep.noaa.gov/products/precip/CWlink/pna/nao_loading.html).
- NOAA CPC (2020a)  
*AO loading pattern*. URL: [https://www.cpc.ncep.noaa.gov/products/precip/CWlink/daily\\_ao\\_index/new.ao.loading.gif](https://www.cpc.ncep.noaa.gov/products/precip/CWlink/daily_ao_index/new.ao.loading.gif).
- NOAA CPC (2020b)  
*EA loading pattern*. URL: [https://www.cpc.ncep.noaa.gov/data/teledoc/ea\\_correlation\\_map.gif](https://www.cpc.ncep.noaa.gov/data/teledoc/ea_correlation_map.gif).
- NOAA CPC (2020c)  
*EA time series*. URL: <https://www.cpc.ncep.noaa.gov/data/teledoc/ea.timeseries.gif>.
- NOAA CPC (2020d)  
*El Niño/Southern Oscillation (ENSO)*. URL: <https://www.ncdc.noaa.gov/teleconnections/enso/>.
- NOAA CPC (2020e)  
*NAO time series*. URL: <https://www.cpc.ncep.noaa.gov/data/teledoc/nao.timeseries.gif>.
- NOAA CPC (2020f)  
*SCAND loading pattern*. URL: [https://www.cpc.ncep.noaa.gov/data/teledoc/scand\\_correlation\\_map.gif](https://www.cpc.ncep.noaa.gov/data/teledoc/scand_correlation_map.gif).
- NOAA CPC (2020g)  
*SCAND time series*. URL: <https://www.cpc.ncep.noaa.gov/data/teledoc/scand.timeseries.gif>.

- NOAA National Centers for Environmental Information (2014)  
*State of the Climate: Global Climate Report for November 2014*. URL: <https://www.ncdc.noaa.gov/sotc/global/201411> (visited on 12/17/2019).
- NOAA National Centers for Environmental Information (2018a)  
*State of the Climate: Global Climate Report for August 2010*. URL: <https://www.ncdc.noaa.gov/sotc/global/201008> (visited on 12/15/2019).
- NOAA National Centers for Environmental Information (2018b)  
*State of the Climate: Global Climate Report for December 2010*. URL: <https://www.ncdc.noaa.gov/sotc/global/201012> (visited on 12/15/2019).
- NOAA National Centers for Environmental Information (2018c)  
*State of the Climate: Global Climate Report for December 2017*. URL: <https://www.ncdc.noaa.gov/sotc/global/201712> (visited on 12/17/2019).
- NOAA National Centers for Environmental Information (2018d)  
*State of the Climate: Global Climate Report for February 2018*. URL: <https://www.ncdc.noaa.gov/sotc/global/201802> (visited on 12/14/2019).
- NOAA National Centers for Environmental Information (2018e)  
*State of the Climate: Global Climate Report for July 2010*. URL: <https://www.ncdc.noaa.gov/sotc/global/201007> (visited on 12/15/2019).
- NOAA National Centers for Environmental Information (2018f)  
*State of the Climate: Global Climate Report for November 2010*. URL: <https://www.ncdc.noaa.gov/sotc/global/201011> (visited on 12/15/2019).
- NOAA National Centers for Environmental Information (2018g)  
*State of the Climate: Global Climate Report for October 2010*. URL: <https://www.ncdc.noaa.gov/sotc/global/201010> (visited on 12/15/2019).
- NOAA National Centers for Environmental Information (2018h)  
*State of the Climate: Global Climate Report for September 2010*. URL: <https://www.ncdc.noaa.gov/sotc/global/201009> (visited on 12/15/2019).
- NOAA NCDC (2010)  
*State of the climate in 2010*. URL: <https://www1.ncdc.noaa.gov/pub/data/cmb/bams-sotc/2010/bams-sotc-2010-brochure-hi-rez.pdf>.
- NOAA PSD (2019)  
*Multivariate ENSO Index Version 2 (MEI.v2)*. URL: <https://www.esrl.noaa.gov/psd/enso/mei/>.
- NOAA/OAR/ESRL PSD (1979 to present)  
*NCEP Daily Global Analyses*. Boulder, Colorado, USA. URL: <https://www.esrl.noaa.gov/psd/>.
- Oliveira, Paulo and L. Gomes (Mar. 2009)  
“Interpolation of signals with missing data using Principal Component Analysis”. In: *Multidimensional Systems and Signal Processing* 21, pp. 25–43. DOI: 10.1007/s11045-009-0086-3.

- Ordóñez, Celestino, Javier Martínez, José Ramón Rodríguez-Pérez, and Amanda Reyes (2011)  
 “Detection of Outliers in GPS Measurements by Using Functional-Data Analysis”. In: *Journal of Surveying Engineering* 137, pp. 150–155.
- Pan, Yuanjin, Wen-Bin Shen, C.K. Shum, and Ruizhi Chen (2018)  
 “Spatially varying surface seasonal oscillations and 3-D crustal deformation of the Tibetan Plateau derived from GPS and GRACE data”. In: *Earth and Planetary Science Letters* 502, pp. 12–22. ISSN: 0012-821X. DOI: <https://doi.org/10.1016/j.epsl.2018.08.037>. URL: <http://www.sciencedirect.com/science/article/pii/S0012821X1830503X>.
- Papoulis, A. (1975)  
 “A new algorithm in spectral analysis and band-limited extrapolation.” In: *IEEE Transactions on Circuits and Systems* 19, pp. 735–742. DOI: 10.1109/TCS.1975.1084118.
- Pearson, Karl (1901)  
*LIII. On lines and planes of closest fit to systems of points in space.* DOI: 10.1080/14786440109462720. URL: <https://doi.org/10.1080/14786440109462720>.
- Petrov, Leonid and Jean-Paul Boy (2004)  
 “Study of the atmospheric pressure loading signal in very long baseline interferometry observations”. In: *Journal of Geophysical Research: Solid Earth* 109.B3. DOI: 10.1029/2003JB002500. eprint: <https://agupubs.onlinelibrary.wiley.com/doi/pdf/10.1029/2003JB002500>. URL: <https://agupubs.onlinelibrary.wiley.com/doi/abs/10.1029/2003JB002500>.
- Pope, A. J. (1976)  
 “The statistics of residuals and the detection of outliers”. In: *NOAA Technical Rep. NOS65 NGS1*.
- Reynolds, Richard W. and Thomas M. Smith (1994)  
 “Improved Global Sea Surface Temperature Analyses Using Optimum Interpolation”. In: *Journal of Climate* 7.6, pp. 929–948. DOI: 10.1175/1520-0442(1994)007<0929:IGSSTA>2.0.CO;2. eprint: [https://doi.org/10.1175/1520-0442\(1994\)007<0929:IGSSTA>2.0.CO;2](https://doi.org/10.1175/1520-0442(1994)007<0929:IGSSTA>2.0.CO;2). URL: [https://doi.org/10.1175/1520-0442\(1994\)007%3C0929:IGSSTA%3E2.0.CO;2](https://doi.org/10.1175/1520-0442(1994)007%3C0929:IGSSTA%3E2.0.CO;2).
- Richman, M.B. (1983)  
 “Specification of complex modes of circulation with T-mode factor analysis.” In: *preprints, Second International Conference on Statistics and Climate*. National Institute of Meteorology and Geophysics, Lisbon., pp. 511–518.
- Richman, M.B. (1986)  
 “Rotation of principal components.” In: *Journal of Climatology*. 6, pp. 293–35. DOI: 10.1002/joc.3370060305.

Roweis, S. (1998)

“EM algorithms for PCA and SPCA”. In: *Advances in neural information processing systems*. Vol. 10. MIT Press, pp. 626–632.

Sagredo, E.A. and T.V. Lowell (2012)

“Climatology of Andean glaciers: A framework to understand glacier response to climate change”. In: *Global and Planetary Change* 86-87, pp. 101–109. ISSN: 0921-8181. DOI: <https://doi.org/10.1016/j.gloplacha.2012.02.010>. URL: <http://www.sciencedirect.com/science/article/pii/S0921818112000409>.

Savage, James and Jerry Svarc (Aug. 2010)

“Postseismic relaxation following the 1989 MS7.1 Loma Prieta earthquake, central California”. In: *Journal of Geophysical Research* 115. DOI: 10.1029/2009JB006919.

Seeber, G. (2003)

*Satellite Geodesy*. Walter de Gruyter. ISBN: 3-11-017549-5.

Shaman, Jeffrey and Eli Tziperman (2011)

“An Atmospheric Teleconnection Linking ENSO and Southwestern European Precipitation”. In: *Journal of Climate* 24.1, pp. 124–139. DOI: 10.1175/2010JCLI3590.1. eprint: <https://doi.org/10.1175/2010JCLI3590.1>. URL: <https://doi.org/10.1175/2010JCLI3590.1>.

Stewart, G. W. (Dec. 1993)

“On the Early History of the Singular Value Decomposition”. In: *SIAM Rev.* 35.4, pp. 551–566. ISSN: 0036-1445. DOI: 10.1137/1035134. URL: <https://doi.org/10.1137/1035134>.

Subirana, J.S., J.M.J. Zornoza, and M. Hernández-Pajares (2011)

*Ocean loading*. URL: [https://gssc.esa.int/navipedia/index.php/Ocean\\_loading](https://gssc.esa.int/navipedia/index.php/Ocean_loading).

Thomas, Dhanya (Aug. 2018)

“Revelation of early detection of co-seismic ionospheric perturbations in GPS-TEC from realistic modelling approach: Case study”. In: *Scientific Reports* 8. DOI: 10.1038/s41598-018-30476-9.

Thompson, David W. J. and John M. Wallace (2001)

“Regional Climate Impacts of the Northern Hemisphere Annular Mode”. In: *Science* 293.5527, pp. 85–89. ISSN: 0036-8075. DOI: 10.1126/science.1058958. eprint: <https://science.sciencemag.org/content/293/5527/85.full.pdf>. URL: <https://science.sciencemag.org/content/293/5527/85>.

Tregoning, P. and T. van Dam (2005)

“Atmospheric pressure loading corrections applied to GPS data at the observation level”. In: *Geophysical Research Letters* 32.22. DOI: 10.1029/2005GL024104. eprint: <https://agupubs.onlinelibrary.wiley.com/doi/pdf/10.1029/>

- 2005GL024104. URL: <https://agupubs.onlinelibrary.wiley.com/doi/abs/10.1029/2005GL024104>.
- Venegàs, S., Lawrence A. Mysak, and David N. Straub (1996)  
“Evidence for interannual and interdecadal climate variability in the South Atlantic”. In: *Geophysical Research Letters* 23.19, pp. 2673–2676. DOI: 10.1029/96GL02373. eprint: <https://agupubs.onlinelibrary.wiley.com/doi/pdf/10.1029/96GL02373>. URL: <https://agupubs.onlinelibrary.wiley.com/doi/abs/10.1029/96GL02373>.
- Wooden, W.H. (1985)  
“NAVSTAR Global Positioning System: 1985”. In: *Proceedings 1st International Symposium on Precise Positioning with the Global Positioning System*. Ed. by C. Goad. Vol. 1. US Department of Commerce, pp. 403–412. URL: <https://apps.dtic.mil/dtic/tr/fulltext/u2/a140793.pdf>.
- Working Group I to the Fifth Assessment Report of the IPCC (2013)  
“Summary for Policymakers”. In: *Climate Change 2013: The Physical Science Basis*. Ed. by T.F. Stocker, D. Qin, G.-K. Plattner, M. Tignor, S.K. Allen, J. Boschung, A. Nauels, Y. Xia, V. Bex, and P.M. Midgley. New York: Cambridge University Press.
- World Meteorological Organization (WMO) (2013)  
*Assessment of the observed extreme conditions during late boreal winter 2011/2012*. URL: <http://www.wmo.int/pages/prog/wcp/wcdmp/documents/Coldspell2012.pdf> (visited on 12/30/2019).
- Wu, W., D.L. Massart, and S. de Jong (1997)  
“The kernel PCA algorithms for wide data. Part I: Theory and algorithms”. In: *Chemometrics and Intelligent Laboratory Systems* 36.2, pp. 165–172. ISSN: 0169-7439. DOI: [https://doi.org/10.1016/S0169-7439\(97\)00010-5](https://doi.org/10.1016/S0169-7439(97)00010-5). URL: <http://www.sciencedirect.com/science/article/pii/S0169743997000105>.
- Zanetti, Francesco (2007)  
“Indagine delle proprietà statistiche di serie temporali di posizione applicata al caso della stazione permanente GPS della base Mario Zucchelli in Terra Vittoria (Antartide)”. Master’s Thesis. Università degli studi di Bologna.
- Zerbini, S., F. Matonti, F. Raicich, B. Richter, and T. van Dam (2004)  
“Observing and assessing nontidal ocean loading using ocean, continuous GPS and gravity data in the Adriatic area”. In: *Geophysical Research Letters* 31.23. DOI: 10.1029/2004GL021185. eprint: <https://agupubs.onlinelibrary.wiley.com/doi/pdf/10.1029/2004GL021185>. URL: <https://agupubs.onlinelibrary.wiley.com/doi/abs/10.1029/2004GL021185>.
- Zerbini, S., F. Raicich, M. Errico, and G. Cappello (2013)  
“An EOF and SVD analysis of interannual variability of GPS coordinates,

---

environmental parameters and space gravity data.” In: *Journal of Geodynamics* 67, pp. 111–124. DOI: 10.1016/j.jog.2012.04.006.



# Acknowledgements

Ringrazio la Prof. Susanna Zerbini per aver supervisionato il mio lavoro durante tutto il suo sviluppo e il Dott. Fabio Raicich dell'ISMAR CNR di Trieste per i suoi preziosi consigli.

Ringrazio la mia famiglia, mio fratello Daniel e Silvia, Sabrina e Alexander, Monica e soprattutto i miei genitori, Paolino e Mirella, che mi hanno sostenuta durante questi anni e hanno reso tutto questo possibile.

Ringrazio Maria e Giuseppe per il sostegno spirituale e Madda, Miri e tutte le persone che mi sono state vicine durante questo percorso.

Infine, ringrazio Marco, Dario e Martina per avermi supportata e sopportata ogni giorno e senza i quali non sarei arrivata fin qui.



# Appendices



## APPENDIX A

**GPS Stations list**

---

GPS station name	Latitude (°)	Longitude (°)
ACOR	43.3644 N	8.3989 W
ALME	36.8525 N	2.4594 W
ALSA	42.8915 N	2.1644 W
AMUR	40.9072 N	16.6040 W
APPL	51.0569 N	4.1996 W
ARAC	37.8939 N	6.5654 W
ARSP	40.2067 N	5.0827 W
AUT1	40.5668 N	23.0037 E
BAIA	47.6518 N	23.5577 E
BMHG	49.6592 N	1.8296 W
BNAF	37.2324 N	8.1267 W
BOR1	52.2769 N	17.0735 E
BPDL	52.0353 N	23.1274 E
BUCK	57.6761 N	2.9615 W
CACI	47.0569 N	3.9328 E
CANT	43.4720 N	3.7981 W
CASB	53.8507 N	9.2873 W
CASC	38.6934 N	9.4185 W
CEU1	35.8920 N	5.3064 W
CLFD	45.7610 N	3.1111 E
CORL	37.8944 N	13.3039 E
COST	44.1615 N	28.6575 E
CRAO	44.4132 N	33.9910 E
CTAB	49.4098 N	14.6802 E
DENI	38.8348 N	0.1037 E
DEVA	45.8784 N	22.9135 E

ELBA	42.7529 N	10.2111 E
EOST	48.5798 N	7.7625 E
EUSK	50.6741 N	6.7635 E
FFMJ	50.0956 N	8.665 E
GAIA	41.1060 N	8.5891 W
GIUR	40.1244 N	18.4301 E
GLOS	49.1215 N	0.2816 E
GLSV	50.3642 N	30.4967 E
HERS	50.8673 N	0.3363 E
HIRS	57.5911 N	9.9676 E
INGR	41.8281 N	12.5148 E
KIRK	54.8395 N	4.0474 W
KIRU	67.8573 N	20.9685 E
KLOK	39.5647 N	22.0144 E
KLRE	54.9649 N	6.6180 W
KRAW	50.0661 N	19.9205 E
KURE	58.2556 N	22.5101 E
LAMA	53.8924 N	20.6700 E
LANU	39.8827 N	9.5484 E
LBUG	44.9454 N	0.9211 E
LDB2	52.2091 N	14.1209 E
LEIJ	51.3540 N	12.3741 E
LERM	42.0266 N	3.7568 W
LLIV	42.4781 N	1.9732 E
LODZ	51.7787 N	19.4595 E
LOVJ	67.8909 N	34.6159 E
LPPZ	48.4463 N	4.7604 W
LROC	46.1589 N	1.2193 W
LUMI	42.6029 N	8.8274 E
MABZ	46.6860 N	10.5511 E
MACY	52.5889 N	3.8518 W
MALL	39.5526 N	2.6246 E
MAN2	48.0186 N	0.1553 E
MAR6	60.5951 N	17.2585 E
MARS	43.2788 N	5.3538 E
METS	60.2175 N	24.3953 E

MIMZ	44.2006 N	1.2283 W
MOBN	55.1149 N	36.5695 E
MSEL	44.5200 N	11.6465 E
MSRU	38.2638 N	15.5083 E
MUEJ	48.1490 N	11.5682 E
NOA1	38.0471 N	23.8641 E
NOT1	36.8758 N	14.9898 E
OPMT	48.8359 N	2.3349 E
ORID	41.1273 N	20.7941 E
OROS	46.5552 N	20.6714 E
OSLS	59.7366 N	10.3678 E
OXFR	51.8239 N	1.2885 W
PACA	40.8704 N	14.5564 E
PENC	47.7896 N	19.2815 E
POLV	40.6026 N	34.5429 E
PTBB	52.2962 N	10.4598 E
RAT0	63.9856 N	20.8956 E
RSTO	42.6584 N	14.0015 E
SKE0	64.8792 N	21.0483 E
SMID	55.6406 N	9.5593 E
SMSP	49.1152 N	4.5813 E
SOFI	42.5561 N	23.3947 E
SONS	39.6753 N	3.9639 W
SPRN	47.6836 N	16.5831 E
SPT0	57.7149 N	12.8914 E
SRJV	43.8678 N	18.4139 E
STAS	59.0177 N	5.5986 E
SVTL	60.5328 N	29.7809 E
SWAN	53.7365 N	0.5050 W
SWKI	54.0986 N	22.9282 E
TERU	40.3505 N	1.1243 W
TGGC	45.1243 N	25.7406 E
TLIA	43.5614 N	1.4806 E
TORI	45.0634 N	7.6613 E
TRDS	63.3714 N	10.3192 E
TRIE	45.7097 N	13.7635 E

TUC2	35.5332 N	34.0706 E
VAAS	62.9612 N	21.7706 E
VAR5	70.3364 N	31.0312 E
VIL0	64.6978 N	16.5599 E
VIS0	57.6539 N	18.3673 E
WARN	54.1698 N	12.1014 E
WSRT	52.9146 N	3.6045 E
ZIMM	46.8771 N	7.4653 E

Table A.1: GPS station name, latitude and longitude.

